Guillem Marín Aguilera

InAsSb/AlInAsSb nBn Photodiodes - A Basic Device Model

June 2021

Master's thesis

2021

Guillem Marín Aguilera

NTNU
Norwegian University of Science and Technology
Faculty of Information Technology and Electrical Engineering
Department of Electronic Systems

NTNU
Norwegian University of Science and Technology

NTNU
Norwegian University of Science and Technology

NTNU

Norwegian University of
Science and Technology

InAsSb/AlInAsSb nBn Photodiodes - A Basic Device Model

Guillem Marín Aguilera

Master of Science in Electronic Systems Design
Submission date: June 2021
Supervisor: Bjørn-Ove Fimland, DES
Co-supervisor: Trond Brudevoll, FFI
Espen Selvig, FFI

Norwegian University of Science and Technology
Department of Electronic Systems

Abstract

In this work, the band structure of a Unipolar Barrier Infrared Detector has been simulated. The sensor's design proposal is based on a previous study carried out by the author. The device consists of a heterostructure containing InAsSb, a prominent semiconductor material in infrared sensing, and lattice-matched AlInAsSb. The former constitutes the contact and the active absorption layer, while the latter has been used as the barrier layer.

The Poisson-continuity solver presented in this work aims to be a helpful tool in the design of infrared photodetectors. The script solves the Poisson Equation and the continuity equation for holes using the Newton-Raphson method with a Finite Differences scheme. The modelling of the material parameters has been taken from literature and adapted to the context of the device. From there, the solver uses the built-in values of those parameters to approximate an initial solution to the electrostatic potential of the heterojunction (V). Using an iterative process, the initial guess is refined until convergence is met. The electrostatic potential after each iteration is used to calculate the gradient of the hole quasi-Fermi level (E_{f_h}) outside thermal equilibrium. Once the Poisson and the hole continuity equations are solved, V and E_{f_h} help to build the band structure of the heterostructure. With this information, other relevant quantities such as the distribution of carriers at the band edges across the device, the electric field profile and the dark current density (J_{dark}) are calculated.

Relevant figures in the detector's performance have been reviewed and the analysis of the simulations results are in good agreement with that reported in the literature, showing the solver successfully accomplishes its mission. With the design presented in this work, $J_{dark} = 8.2x10^{-5} A/cm^2$ in saturation at 200 K. The dark current density reported here can compete with other reports using a similar architecture and material system approaches.

Preface

This report was submitted in the academic semester in the summer of 2021 for the Department of Electronic Systems at Norges Teknisk-Naturvitenskapelige Universitet in collaboration with Forsvarets Forskningsinstitutt. The present work treats a one-dimensional Poisson-continuity solver adapted to a unipolar barrier photodetector and is presumed to be read by those who already have preliminary knowledge of these subjects.

Acknowledgements

I would like to thank my supervisors Trond Brudevoll, Espen Selvig and co-supervisor Bjørn-Ove Fimland for providing me with great amounts of information related to this work, how to structure the report and their valuable comments and feedback.

I would like to thank my family for their support despite being far away in these troubled times. I would also like to have a few words for my friends, without their help this work would not have been possible: to Núria and Gemma, for holding me tight in the distance; to Pau, for his weekly dose of wisdom and enthusiasm; to Èlia, for always having an answer; to Lisa for the movie nights and shining some light in this report and finally, to Bibek, Hugues and Mahmoud, for walking the way with me.

Table of Contents

List of Figures

List of Tables

Abbreviations

IR = Infrared

NIR = Near Infrared

SWIR = Short wavelength Infrared

MWIR = Medium wavelength Infrared

LWIR = Long wavelength Infrared

FIR = Far Infrared

MCT = *HgCdTe*

FPA = Focal Plane Arrays

SRH = Shockley-Read-Hall

MBE = Molecular Beam Epitaxy

MOCVD = Metal Organic Chemical Vapor Deposition

CB = Conduction Band

VB = Valence Band

CBO = Conduction Band Offset

VBO = Valence Band Offset

SCR = Space Charge Region

FD = Fermi-Dirac

MB = Maxwell-Boltzmann

EHP = Electron Hole Pair

GR = Generation Recombination

APD = Avalanche Photodiode

SACM = Separate Absorption Charge Multiplication

T2SL = *type II* Superlattice

QE = Quantum Efficiency

UBIRD = Unipolar Barrier Infrared Detector

CBIRD = Complementary Barrier Infrared Detector

QWIP = Quantum Well Infrared Photodetector

QDIP = Quantum Dot Infrared Photodetector

HOT = High Operating Temperature

LPE = Liquid Phase Epitaxy

BLIP = Background Limited Infrared Photodetection

HLBC = High Low Blocking Contacts

DCRF = Dark Current Reduction Factor

1. Introduction

1.1 Motivation and Background

The work presented in the upcoming lines is the continuation of a project carried out during the first semester of the second year of the author's MSc degree. The main goal of this work was to write a program able to accurately replicate the characteristics of a unipolar barrier photodetector in terms of its band structure, carrier densities and electrostatic potential. Once these parameters have been calculated, the performance of the device can be evaluated as well as some tendencies that the detector may manifest at certain conditions.

The motivation behind the development of this thesis is to contribute to the design of infrared detectors with new III-V semiconductors with a useful computational tool. The Poisson-continuity solver aims to reliably represent the band structure characteristics which will ultimately determine the performance of the device.

The design of the unipolar barrier infrared photodetector is based on a previous study performed by the author on this sort of devices. By using the Poisson-continuity solver, those initial designs have been optimized and updated while studying the properties of the proposed material system.

This thesis is divided into six basic chapters. First, an introduction to basic concepts of the infrared, the possible applications of the studied devices and the state-of-the-art material system that is aimed to overcome. Next, in Chapter 2 there will be a summary of the basic theoretical concepts needed to understand the working principle of the photodetectors as well as the theoretical basis to the methods employed in the solver. Chapter 3 describes the conception of the solver. Later, in Chapter 4 the accuracy of the program has been tested by calculating different parameters and simulating the behaviour of the detector at various conditions. Finally, in Chapter 5 there is a review of possible modifications, ideas for new directions to optimize the solver and the final remarks from the performed work. Chapter 6 serves as a conclusion for this work.

1.2 Introduction to IR

The Einstein-Planck relation establishes that the energy of photons, discrete packets of electromagnetic energy, is defined by their wavelength (λ), the Planck's constant (h) and light's velocity (c).

$$E = \frac{hc}{\lambda} \tag{1.1}$$

Depending on the wavelength of the photons, and therefore of its energy, one can place the electromagnetic radiation in a specific part of the spectrum. Light in different regions of the electromagnetic spectrum interacts with matter differently. Take for example the human eye: only a tiny region of the incoming radiation to our eyes is sensed by the retina. This region of the electromagnetic spectrum is called the visible range and contains light with wavelengths between 400 and 700 nm. The devices proposed in this work are designed to sense radiation in another part of the spectrum, the infrared (IR), which is composed of wavelengths above the cut-off for red visible light at 700 nm and up to 1 mm.

The first description of the IR was given by William Herschel [1], a British astronomer who discovered it when he was trying to measure the energy distribution of sunlight radiation. Herschel found that the highest temperature on his thermometer was registered beyond the red light. As stated before, the IR accounts for wavelengths larger than the visible up to radio wave band. That is quite a broad part of the spectrum, therefore the classification of the IR radiation is sub-divided into smaller portions according to the light wavelength.

Near-Infrared (NIR) region is a powerful tool for sensors employing the capabilities of NIR spectroscopy, especially for medical applications as it can penetrate deeper into the tissues and requires

Division Name	Abbreviation	Wavelength (μm)	Photon Energy (meV)
Near-Infrared	NIR	0.75 - 1.4	1653 - 886
Short Wavelength Infrared	SWIR	1.4 - 3	886 - 416
Medium Wavelength Infrared	MWIR	3 - 8	416 - 155
Long Wavelength Infrared	LWIR	8 - 15	155 - 83
Far-Infrared	FIR	15 - 1000	83 - 1.2

Table 1.1: Classification of the different regions for IR according to their wavelength and photon energy.

little sample preparation [2]. Short-wavelength Infrared is mainly used in long-range telecommunications since at 1.55 μm the attenuation loss for the optical fiber is minimized [3]. Medium-wavelength Infrared (MWIR) range goes from 3 to 8 μm and it covers a part of the spectrum where the IR radiation is strongly absorbed by the atmosphere. From 8 to 15 μm there is the so-called Long-wave Infrared (LWIR), also named the thermal imaging region, in which sensors can obtain information from thermal emissions of objects. Finally, the far-Infrared (FIR) region contains wavelengths up to 1 mm and is broadly used in astronomy to capture cold-matter radiation [4].

IR radiation is emitted or absorbed by molecules when there is a change in the vibrational or rotational state. IR absorption only occurs for certain wavelengths that correspond to differences in energy levels of the atoms/molecules. These special conditions for absorption are called selection rules. The scope of this project is the design and characterization of photodetectors in the MWIR and LWIR domain.

1.3 Applications

As stated before, one of the fields of science that greatly benefits from IR sensing applications is astronomy. Planets absorb light from stars and heat up. This radiation will be later emitted as heat in the IR spectrum region. In our solar system, the temperatures of the planets are close to the MWIR and LWIR domains (500 to 100 K) [4].

One consideration when discussing possible applications for MWIR or LWIR regimes is the environmental conditions at which the detectors will operate. As it was previously mentioned, at certain wavelengths in the MWIR region, the absorption from molecules in the atmosphere reaches a maximum which makes the operation way more difficult.

Another consideration for choosing between MWIR or LWIR imaging systems is the target temperature. MWIR offers a better thermal contrast - how the signal is normalized to the background - . For high-temperature targets, the MWIR band gives better imaging and that is why it is chosen for the detection of missiles, airplanes and other military applications.

Imaging is the field where IR photodetectors have the most to say with many areas of research that apply directly these technologies. Different approaches are possible depending on the purpose and the frequency range targeted.

The primary example would be infrared photography and how it has evolved from an artistic perspective to other areas such as forensic criminology and medicine, with leading companies in photographic technologies competing in the market. These devices are particularly interesting because of their versatility since a relatively similar architecture can easily be adapted to multiple applications in unrelated fields.

Military research has been one of the driving forces to impulse the advance of new material systems, architectures and strategies for IR sensing. There are many applications related to defence that benefit from the IR photodetectors. Night vision, for example, exploits the absorption characteristics of certain materials in IR range to convert the ambient photons into electrons,

amplify them and convert them back to visible light, increasing the visibility in dark conditions without needing a visible light source [5].

1.4 HgCdTe

The most common material system for sensing the IR is HgCdTe (MCT). This alloy has been unbeatable in terms of performance since it was first introduced in the 1960s. A bit earlier, in 1959, Lawson et al. [6] discovered the immense tuning possibilities that appeared when combining a semiconductor, CdTe, with a semimetal, HgCd. By changing the Hg molar fraction in the alloy, the band gap could be tuned to a specific value of energy, thus, opening the possibility to cover all the IR spectrum with just the variation of the alloy composition [1].

For nearly 60 years, MCT has overcome the major issues presented by other material systems, almost reaching theoretical limits for device detectivity and responsivity [7]. From the mid-seventies, the attention turned from photoconductive detectors to photodiodes as they were easier to multiplex. Having the detectors arranged as pixels in Focal Plane Arrays (FPAs) opened the possibility for smaller and lighter structures. Moreover, photodiode-based detectors have less low-frequency-associated noise, provide a faster response time and are easier to integrate into other device architectures [1].

The current state-of-the-art of MCT-based photodetectors consists of both homo- and heterostructure photodiodes. The absorber is sandwiched by two wide band gap layers that help to reduce dark current when the device is biased.

One of the main advantages that MCT provides in a photodetector is the large minority carrier lifetime. Generation-Recombination processes in bulk materials are determined by an amalgam of different factors. In optoelectronics, one of the starting points to improve the device characteristics is to minimize the non-radiative recombination processes that decrease its performance. In that sense, MCT has proven the best in the suppression of Shockley-Read-Hall recombination processes (SRH), or trap-assisted recombination. The long SRH carrier lifetime has been one of the main features for the wide use of MCT as a photodetector material.

1.5 Beyond HgCdTe photodetectors

MCT photodetectors have been proven reliable and practical throughout the last 60 years. However, there are some technical issues that the material system has not been able to overcome. For example, MCT devices are extremely sensitive to material growth techniques as non-uniform compositions can lead to variations of the wavelength in the LWIR regime. This is especially critical when it comes to the mass production of FPAs.

Growing MCT epitaxially by Molecular Beam Epitaxy (MBE) is quite more challenging than III-V semiconductor counterparts due to the high vapour pressure that is necessary to grow Hg [1]. III-V semiconductors show a lower ionic character and are chemically more stable and robust [8].

One path that has been discussed is Sb-based photodetectors with their multiple approaches and structures. Although InSb has a small band gap and that may deviate its potential applicability in the MWIR, it can be easily incorporated into a ternary alloy with InAs, which possesses a band gap suitable for this spectral range. Using these two materials or a combination of them with other elements, Ga for example, has been the driving force to push the technology development in a new direction. Superlattice heterostructures based on InAs/GaInSb have shown some promise as the resulting material system opens the door to new engineering formulas that could out-compete the current state-of-the-art MCT technologies.

InAsSb ternary alloy can be grown with both MBE and Metal-Organic Chemical Vapor Deposition (MOCVD) and prevents using Ga in the photodetector's material system. This element has been

associated with some undesirable carrier lifetime shortening effects. At the same time, InAsSb provides some flexibility in terms of the spectral region the device will be working as its band gap can be tuned with Sb's molar fraction. Despite its versatility, InAsSb's band gap appeared to be very sensitive to the substrate it is grown on, and strain derived from lattice mismatching can alter its properties [9].

Aside from particular device characteristics improvements that new material systems can bring, the interest to go beyond MCT detectors is to move towards a greener approach and reduce the presence of Hg and Cd due to their toxicity.

2. Theory

The following chapter contains an introduction to the necessary concepts to understand the design process flow and familiarize the reader with the theory laying behind the proposed photodetector. The chapter includes a review of basic Heterostructure concepts, the equations self-consistently solved by the script - Poisson and continuity -, and an introduction to photosensors with special detail into barrier detectors in the context of the proposed device. Finally, the numerical methods used in the solver: the Newton-Raphson Method and the Finite Differences Scheme have also been encompassed in a section within this chapter.

2.1 Heterostructures and Heterojunctions

In the design of photodetectors, it is important to understand that not all materials are suitable for all situations. One needs to evaluate the application and operation conditions of the device to choose the proper material system. Thus, it is quite common to find structures that combine several semiconductors and semi-metals to optimize the device's characteristics. For this reason, it is interesting to review what happens at the interfaces between different materials as they will greatly influence and limit the response of the structure.

The energy band diagrams for devices with position-dependent alloy composition, also called heterostructures, are not only dependent on how the band gap changes across the structure, but also on the alignment of the bands between the different constituents [10]. The offsets in the conduction and valence bands of the different materials determine the alignment type. A discontinuity in one of the bands between the participating materials in the heterostructure can severely affect the performance of the device as it can limit the flow of carriers and lead to the build-up of electric fields.

2.1.1 Types of Alignment

Depending on the relative position of the material's band edges, the alignment will appear to have certain characteristics. The three types of band alignment can be described as:

- **Type I**, the band gap of one of the semiconductors lies totally inside the energy gap of the other material. The inequalities E_{c_2} (pink) $> E_{v_1}$ (blue) and E_{v_2} (pink) $> E_{v_1}$ (blue) are verified.
- **Type II**, the band gap of one of the semiconductor does not fully lie in the energy range of the other semiconductor's band gap. In this situation, E_{c_2} (pink) $> E_{v_1}$ (blue) is verified, but the second inequality is not necessarily true.
- **Type III**, there is no overlap between the band gaps of the two semiconductors and none of the previous inequalities are true.

The alignment types described above are shown in Figure 2.1. The band gap of semiconductor 1 is represented by the blue rectangle, while the band gap of semiconductor 2 is represented by the pink rectangle.

The alignment type has a strong influence on the properties that the device will show later. Primarily, any discontinuity in the valence or conduction band represents an impediment for the carrier's flow from one material to the other. To overcome this sudden energy barrier that appears at the boundaries between materials, the carriers from the smaller band gap semiconductor need to gain some kinetic energy to reach the bulk of the large band gap material. This amount of energy the carriers need to gain is equal to the magnitude of the discontinuity. If electrons in the conduction band are being considered, this offset is referred to as ΔE_c. If, on the other hand, the focus is on the valence band holes movement, the energy difference is ΔE_v.

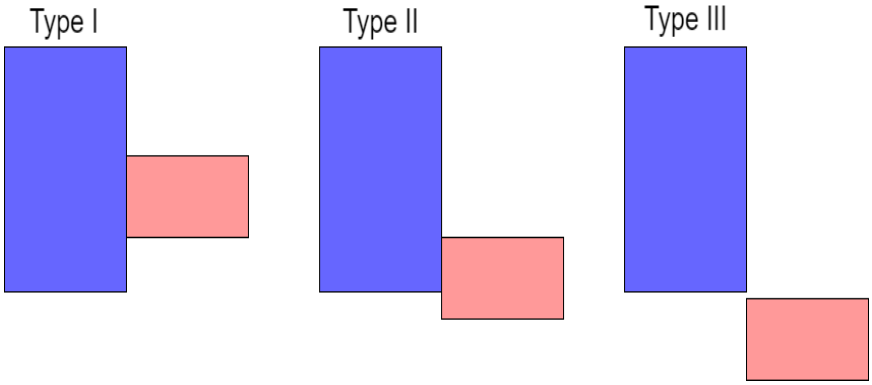

Figure 2.1: Types of alignment according to the relative position of the band positions of the semiconductors involved.

The simplest way to predict which kind of band alignment the material stack of choice will present is to make use of the *Anderson's rule*, also known as the *Electron Affinity Rule*. According to the work from R. L. Anderson [11], when describing a heterojunction between two semiconductors, they will both share the same vacuum level energy. From there, one can use the material properties - mainly the electron affinity and the band gap - to construct the band diagram of the heterostructure and its band alignment.

The energy difference in the conduction band edges will come from the electron affinity difference between the two materials,

$$\Delta E_c = \chi_1 - \chi_2 \tag{2.1}$$

Another fundamental relation that arises from the *Electron Affinity Rule* is that

$$\Delta E_c = \Delta E_g + \Delta E_v \tag{2.2}$$

Where ΔE_g is the difference between the semiconductors band gap.

Although the band alignment comes from the isolated bulk properties of the materials in the junction, the presence of these discontinuities has an effect when determining the band bending characteristics and the diffusion of carriers in the space charge regions. The combination of Poisson equation and the *Anderson's rule* gives the final band structure of the heterostructure.

In this work, the case of study heterostructure presents a couple of heterojunctions, one at each side of the barrier layer. The material of the unipolar barrier is set to be $Al_{0.7}In_{0.3}As_{0.3}Sb_{0.7}$, and surrounding it, there are the contact and the absorption layers composed of $InAs_{0.91}Sb_{0.09}$. The resulting band alignment at 300 K happens to be *type I* as the small band InAsSb has its valence band edge sitting some meV above the valence band edge of AlInAsSb.

For this combination of semiconductors, the relevant parameter to look at is the valence band offset (VBO), ΔE_v, as its value contributes more decisively to the performance of the photodetector.

2.1.2 The Depletion Approximation

The characteristics of the junction, however, are not solely dependent on the position of the band edges, but also the doping in the materials, both in type - n or p - and in quantity. The dopant

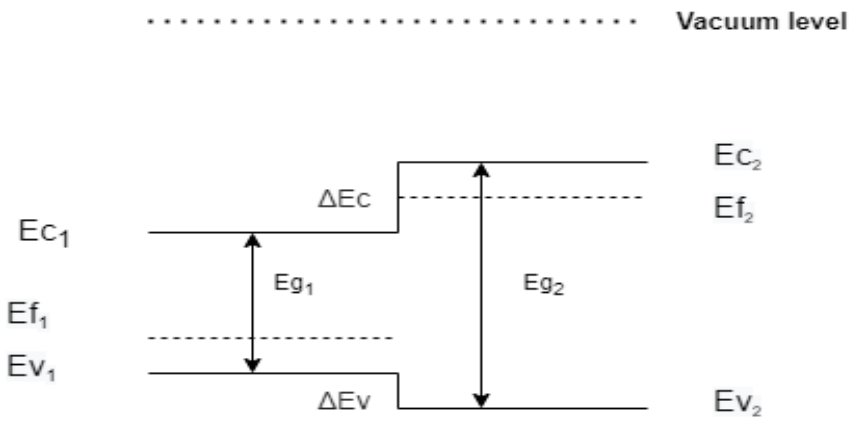

Figure 2.2: $p-N$ heterojunction band structure for two semiconductors with some valence band and conduction band offsets. The alignment is *typeI*.

densities in the semiconductors will determine the energy of the Fermi levels which, in turn, define most of the intrinsic characteristics of the device.

At equilibrium, the Fermi level, E_f, across the heterojunction should sit at a constant energy once the semiconductors have been placed in contact. This should be taken into consideration when solving the Poisson equation and both the band bending and the charge distribution in the heterostructure are calculated

Take for example the band structure of a common *p-N junction* diode like the one in Figure 2.2. The two semiconductors have been doped differently and their band alignment is *type I*. It is clear that in the n-semiconductor the E_f lies above the mid-gap energy and close to the conduction band. Meanwhile, in the $p-type$ material, the Fermi level is closer to the valence band. When the two materials are placed together at equilibrium, the energy of the Fermi level across the junction remains constant and the energy bands bend according to the solution of the Poisson equation.

The built-in potential, V_{bi}, is equal to the shift in the E_f's position from the initial state, when bulk materials are isolated, to once the heterojunction has been set. It can be described by the following equation:

$$qV_{bi} = E_{f_n} - E_{f_p} \tag{2.3}$$

This electrostatic potential arises from the different dopant densities and the semiconductor's characteristics. Making use of the *Anderson's rule*, V_{bi} can be rewritten for the heterojunction as

$$qV_{bi} = \Delta E_c + k_b T ln \frac{N_a\ N_d}{n_{i_n}\ n_{i_p}} - \frac{E_{g_p} + E_{g_n}}{2} - k_b T ln \frac{N_{v_p}\ N_{c_n}}{N_{c_p}\ N_{v_n}} \tag{2.4}$$

Where N_a and N_d are the dopant densities, n_i is the intrinsic carrier concentration for each material and N_v and N_c are the valence and conduction band densities of states for each material respectively.

The magnitude of V_{bi} is indicative of the electrostatic potential that appears at the junction and, therefore, of the band bending. Taking the situation described in Figure 2.2, when the $p-$ and $n-$ materials come in contact, the mobile charge carriers will recombine near the junction creating a space charge region (SCR) depleted from carriers. The ionized dopants will define two spatial regions with a charge build-up and an electric field will arise in the so-called Depletion Region.

The solution of the Poisson equation, which will be treated with greater detail in an upcoming section of this chapter, gives a measure of the charge distribution in the semiconductors and the depletion region. The width of such space region is a function of the dopant level densities in the materials involved in the junction. One can then see the intrinsic relationship between the built-in potential and the depletion region.

2.1.3 Isotype Heterojunctions

Heterojunctions appear when two different semiconductors are placed together, at those interfaces, the depletion region extends on both sides of the junction. However, for complicated device structures, it is convenient to place in contact two different materials with the same dopant type. In this case, we have an isotype heterojunction and it should be treated a bit differently.

Take the case of an $n-N$ heterojunction. Let's set semiconductor 1 with a smaller band gap than semiconductor 2. Also, we assume the band alignment is *type II* like in Figure 2.3. Now, there is not an actual depletion region as for the case described before. However, near the interface, the large band gap material is depleted of majority carriers. The $n-N$ heterojunction in Figure 2.3 is an illustrative example of the band alignment that one will encounter when treating the InAsSb - AlInAsSb heterostructure at low temperatures.

This charge transfer region in the large band gap material will have a defined width determined by the dopant level density of the semiconductor [12]. It is possible to make a qualitative analysis of the interface and see that the built-in potential will be given by the difference in the Fermi levels for the isolated bulk semiconductors as before. Adapting equation 2.4 to the new scenario gives,

$$qV_b = \phi_N - \phi_n = \Delta E_c + k_b T \; ln(\frac{N_D N_c}{N_C N_d}) \tag{2.5}$$

N_D and N_C are the dopant density and the electron density in the conduction band for the large band gap semiconductor. N_d and N_c are the dopant density and the electron density in the conduction band for the small band gap semiconductor. ϕ_N and ϕ_n are the energy difference between the vacuum level and the Fermi level for the two semiconductors, where, ϕ_N is for the large band gap material and ϕ_n is for the small band gap semiconductor. In addition to that, the built-in potential must be the sum of the potential drop at each side of the interface

$$V_b = V_{b_N} + V_{b_n} \tag{2.6}$$

The space charge region in an isotype heterojunction deviates from the usual $p-n$ junction. As mentioned before, the majority carriers of the large band gap semiconductor diffuse away and the material will be depleted from majority carriers inside the SCR. On the other side of the space charge region, however, the majority carriers are going to accumulate creating a 2D electron/hole gas well.

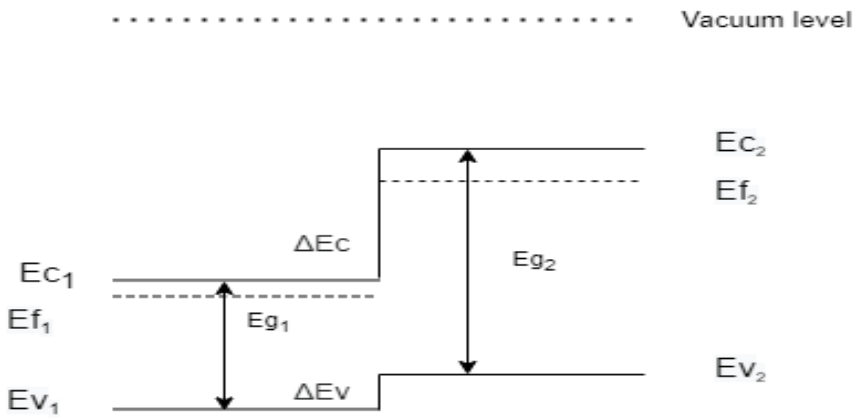

Figure 2.3: $n-N$ heterojunction band structure for two semiconductors with some valence band and conduction band offsets. The alignment is $typeII$.

2.2 Poisson Equation

To simulate properly the device proposed in this work, one needs to solve the Poisson Equation. Its expression is shown below:

$$\frac{\partial}{\partial x}\ [\ \varepsilon(x)\ \frac{\partial V(x)}{\partial x}\ ] = -\rho(x) \tag{2.7}$$

Where $\varepsilon(x)$ is the position-dependent dielectric permittivity, $V(x)$ is the electrostatic potential across the heterostructure and $\rho(x)$ is the position-dependent charge density. $\rho(x)$, as shown below, is described by the electron concentration in the conduction band, *n(x)*, the hole concentration in the valence band, *p(x)* and the dopant concentration in each of the materials composing the diode, $N_{dop}(x)$.

$$\rho(x) = q\ [N_{dop}(x) + p(x) - n(x)] \tag{2.8}$$

$N_{dop}(x)$ in the equation above refers to the effective dopant concentration in the materials. Assuming full ionization of the dopants, this quantity can be expressed as the difference between the donor atoms concentration, $N_d(x)$, and the acceptor atoms concentration, $N_a(x)$.

$$N_{dop}(x) = N_d(x) - N_a(x) \tag{2.9}$$

To describe the concentration of holes in the valence band across the device, *p(x)*, Fermi-Dirac (FD) statistics are used. The FD distribution, $f(E)$ accounts for the probability of an electron occupying an energy states, therefore, for a hole the occupation probability of an energy state at a certain temperature is $1 - f(E)$. In the FD distribution, shown below, the holes fill the energy states in the valence band according to their energy, E, with respect to the position of the Fermi level, E_f. k_b is the Boltzmann's constant and T is the temperature.

$$1 - f(E) = 1\ -\ \frac{1}{1 + exp((E - E_f(x))/k_bT)} \tag{2.10}$$

For each material, to determine the hole concentration, the FD distribution is weighted by $g_v(E)$, the bulk effective density of states in the valence band. In the equation below, $m_h^*(x)$ is the

hole effective mass as a function of the position and h is the Planck's constant. $g_v(E)$ comes to represent the density of states in the valence band, with the square root factor being $\sqrt{E_v(x) - E}$.

$$g_v(E) = \frac{8\pi\sqrt{2}}{h^3}\ m_h^*(x)\sqrt{(E_v(x) - E)} \tag{2.11}$$

With all of this, one can construct the equation for the hole concentration in the valence band. The expression is shown below.

$$p(x) = \int_{-\infty}^{E_v} \frac{8\pi\sqrt{2}}{h^3}\ m_h^*(x)\sqrt{E_v(x) - E}\ \frac{dE}{1 + exp(-(E - E_f(x))/k_bT)} \tag{2.12}$$

On the other hand, $g_c(E)$ is the the density of states in the conduction band with $\sqrt{-(E_c(x) - E)}$. $m_e^*(x)$ now stands for the electron effective mass. This expression can be used to calculate the electron density in the conduction band.

$$g_c(E) = \frac{8\pi\sqrt{2}}{h^3}\ m_e^*(x)\sqrt{-(E_c(x) - E)} \tag{2.13}$$

Similarly to holes, to treat the electrons in the conduction band for the two regions with InAsSb (contact and absorption layers) FD statistics are taken into account as the Fermi level, E_f, lies very close to the conduction band, E_c. Using the corresponding $g_c(E)$ expression shown in Equation 2.13, the electron density in the conduction band can be calculated as depicted below.

$$n(x) = \int_{E_c}^{\infty} \frac{8\pi\sqrt{2}}{h^3}\ m_e^*(x)\sqrt{E - E_c(x)}\ \frac{dE}{1 + exp(E - E_f(x))/k_bT)} \tag{2.14}$$

Within the AlInAsSb layer of the device heterojunction, the Fermi level sits several k_bT away from the conduction band edge due to the material being depleted of mobile carriers. Therefore, the electrons in the conduction band are assumed to follow the Maxwell-Boltzmann (MB) distribution, as seen in the equation below.

$$n(x) = N_c(x)\ exp(-(E_c - E_f)/k_bT) \tag{2.15}$$

In this case, N_c is referred to as the bulk effective density of states in the conduction band. Its equation is shown below, with $m_e^*(x)$ being the electron effective mass.

$$N_c = 2(\frac{2\pi k_bT m_e^*}{h^2})^{3/2} \tag{2.16}$$

The influence of the electrostatic potential and the applied bias on the band curvature will shape the distribution of carriers across the device, defining the regions where accumulation and depletion might happen. Solving the Poisson equation in the heterostructure is the first step to find out the band profile of the photodiode.

2.3 Continuity equations

When a bias is applied across the photodiode, it is not possible to consider that the Fermi level is constant in the device, but it is useful to refer to the quasi-Fermi levels for each kind of carrier,

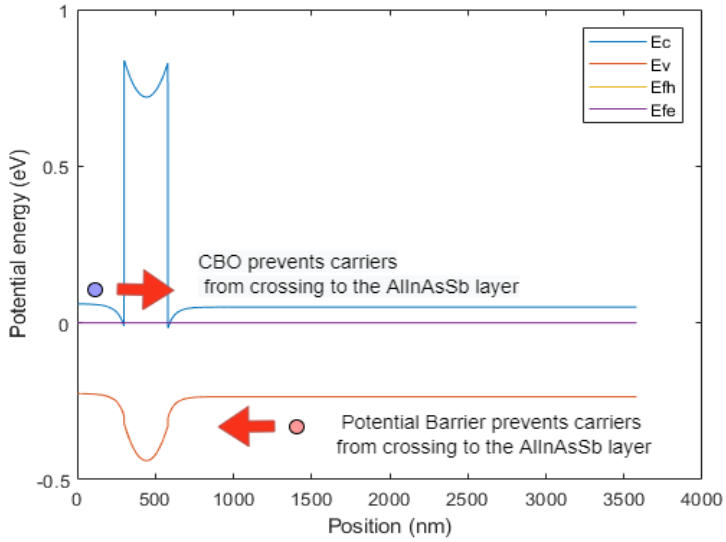

Figure 2.4: Holes in the barrier layer at $V_{app} = 0$ V can not move to the contact layer on the left at due to the high potential barrier in the valence band that appear within the barrier layer. E_{f_h} is superimposed to E_{f_e} as they share the same position.

both electrons, E_{f_e}, and holes, E_{f_h}. The new conditions should manifest in a split of the carriers' quasi-Fermi levels with a magnitude equal to the same applied bias [13].

An applied bias will inject electrons in the sample, and therefore, deviate the carrier population from its value at thermal equilibrium. However, that is not the only method to push the device out of equilibrium. In photodiodes, the carrier generation rate can be stimulated by illuminating the sample with the proper wavelength. The absorption of the incoming radiation by the semiconductor will promote electrons in the valence band to jump into an energy state in the conduction band generating an electron-hole pair in the process.

These two mechanisms will increase the carrier population in the corresponding bands. The newly generated/injected carriers are called excess carriers and they will contribute to the conductivity of the material. The EHP generated from illuminating the sample and the injected electrons from the voltage source will displace the carrier concentrations from their value at thermal equilibrium and, thus, move the quasi-Fermi level of the carriers away from the unbiased E_f value. The presence of the photogenerated EHP will have a more visible effect over the minority carrier population, and the larger shift will be observed in the minority carrier quasi-Fermi level position.

In the case of the nBn detector, an applied bias is necessary to reduce the valence barrier created at the heterojunction and enable to collect the photogenerated holes at the contact. As seen in Figure 2.4, at zero bias the potential barrier in the valence band is too large for holes to overcome it and move to the contact layer.

When a voltage is applied and the potential barrier is reduced, these excess carriers will be able to diffuse in the detector and the movement of charges will lead to the appearance of a current within the device. The double heterojunction at the edges of the barrier layer will lead to a gradient in the electrostatic potential which, in turn, will create an electric field. The carriers moving by the action of the **E** field contribute to the drift current. In nBn photodetectors, the conduction band offset is so large that the electron drift current is disabled. The main contribution to dark current comes from those photocarriers able to make it to the edge of the absorber region and have enough kinetic energy to overcome the valence band barrier. These carriers will later be swept by the field. At equilibrium, with no applied bias nor sample illumination conditions, the number of carriers

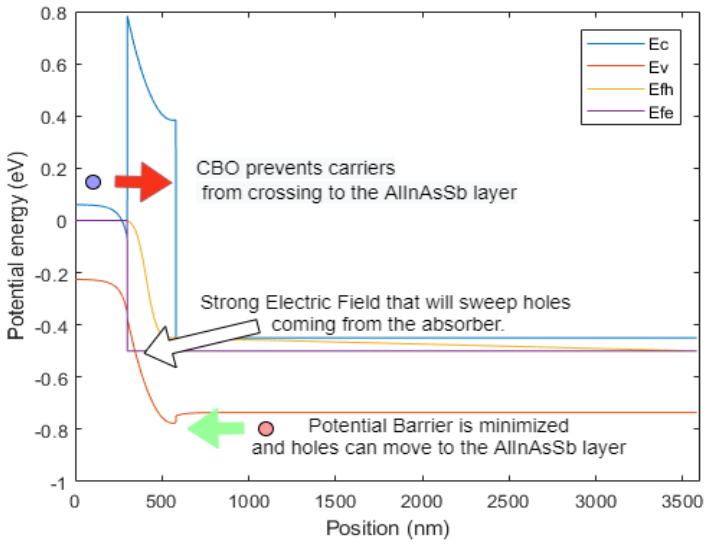

Figure 2.5: At an applied bias $\neq 0$ V, holes will be able to surmount the potential barrier and move to the contact layer. The Electric field inside the barrier layer is high and will sweep the carriers and contribute to the drift current. The electrons in the contact can not make it to the absorber because of the large CBO.

traversing the energy barrier will be the same in opposite directions, resulting in zero net current. However, once the applied bias reduces the barrier in the valence band at the barrier-absorber junction, it will also enhance the transport of photogenerated carriers to the contact layer. Figure 2.5 is representative of the photocarrier collection once the potential barrier has been reduced.

The other contribution to the current outside of the equilibrium will come from the random thermal motion of carriers in the semiconductor. This contribution, called the diffusion current, arises from the uneven distribution of the carriers in the materials. The bending of the energy bands gives a good hint on that aspect. In the nBn photodetector, there are spatial regions where the electrons accumulate. In this context, holes and electrons tend to diffuse favouring a gradient of concentration. Each carrier kind from the photogenerated pair will diffuse in opposite directions, some are going to recombine eventually, but there will be holes that make it to the edge of the absorption region, and, if they have gained enough kinetic energy, overcome the potential barrier. It can be understood how the diffusion of photogenerated holes to the edge of the barrier layer constitutes the limiting mechanism for the current in the detector.

The hole and electron drift and diffusion contributions are shown in the equations below. As mentioned before, the drift current for electrons in the nBn detector is negligible. How the different regions of the device add up to the current will be discussed later on in this thesis.

$$J_n(x) = q\ \mu_n(x)\ n(x)\ \mathbf{E}\ (\mathbf{x}) + q\ D_n(x)\frac{\partial n(x)}{\partial x} \tag{2.17}$$

$$J_p(x) = q\ \mu_p(x)\ p(x)\ \mathbf{E}\ (\mathbf{x}) - q\ D_p(x)\frac{\partial p(x)}{\partial x} \tag{2.18}$$

In the expressions above, μ is the carrier mobility in the material and D is the diffusion coefficient at each layer of the heterostructure, D is also carrier dependent. Currents have been expressed as current densities for holes, J_h, and electrons, J_e.

As stated before, moving out from thermal equilibrium will result in a split of the Fermi level into the quasi-Fermi levels for holes and electrons. Now, these split E_f represent the new distribution of carriers once the excess carriers have been taken into account. The carriers added by the optically generated EHPs will also move favouring a gradient of concentration determined by the position of the quasi-Fermi levels. In other words, the appearance of a current is directly related to a gradient of the quasi-Fermi levels. The new dependence is pictured in the equations below.

$$J_n(x) = \mu_n(x)\ n(x)\ \frac{\partial E_{f_e}(x)}{\partial x} \tag{2.19}$$

$$J_p(x) = \mu_p(x)\ p(x)\ \frac{\partial E_{f_h}(x)}{\partial x} \tag{2.20}$$

Even though excess carriers may take a very important role outside the equilibrium, if the radiation or voltage sources are turned off, the system will relax and return to the equilibrium situation. That is because of the recombination mechanisms present in the semiconductor. Take, for example, an infinitesimal piece of material in the absorber region: depending on the generation-recombination processes happening in that volume, the number of carriers crossing the "entrance" surface might be different to the number of carriers crossing the exit surface. Rephrasing it, the rate of change in the carrier concentration is proportional to the gradient of carrier flux through that region minus the generation-recombination rate (assuming the recombination rate is greater than the generation rate), $GR(x,t)$ [13]. If one takes electron and hole charge, the spatial variation of carrier flux can be understood as a gradient in current density. The situation described here is well modelled for electrons and holes in the continuity equations.

$$\frac{\partial n(x,t)}{\partial t} = \frac{1}{q}\frac{\partial J_e(x,t)}{\partial x} + G_n R_n(x,t) \tag{2.21}$$

$$\frac{\partial p(x,t)}{\partial t} = -\frac{1}{q}\frac{\partial J_h(x,t)}{\partial x} + G_p R_p(x,t) \tag{2.22}$$

2.4 Photodetectors

The ability to sense infrared light and other sorts of electromagnetic radiation is a fundamental part of the technology that surrounds us. A photodetector, or photosensor, accomplishes this mission by capturing light and converting it into a measurable current.

2.4.1 Photoconductors

The easiest implementation of a photosensor is to exploit the photoconductive properties of the material without making use of a $p-n$ junction. The mechanism could be described the following way: an EHP is generated by the absorption of a photon, since the device is biased, the electric field is going to sweep each carrier kind in opposite directions varying the electrical resistance of the device depending on the amount of light irradiated on it.

Photoconductors appear to be very suitable for long-wavelength infrared light and their design flow is simpler than other photosensor devices. No $p-n$ junction is needed, nor epitaxial growth, which reduces the complications and costs from the device's architecture design [14].

One of the advantages that photoconductor sensors have upon photodiodes is their ability to introduce carrier gain. Once the electron-hole pair has been generated, the carriers will drift in opposite directions. However, since they have different velocities, one of them is going to arrive first at its corresponding contact. If a majority carrier goes into the wire, another majority carrier

is injected from the other side. After many of these roundtrips, there would be an accumulation of carriers and therefore a carrier gain. That is possible if the transit time of the majority carrier, i.e. the time that it takes to go around the semiconductor, is greater than the carrier lifetime. However, the photoconductive gain can lead to an increase in the device's dark current, reducing the sensing ability of the photoconductor.

The role of contacts is vital to exploit the characteristics of these devices to their maximum, this is to say, keeping minority carriers "alive" - without recombining - while the majority carriers go on multiple roundtrips in the semiconductor. The blocking contacts prevent minority carriers to enter highly doped contact regions where they will be prone to suffer from recombination. The band alignment should also prevent minority carriers to tunnel to those contact regions while keeping the Ohmic character of the junction.

2.4.2 Photodiodes

The most common type of photodetectors is photodiodes. The absorption of photons generates an electron-hole pair which will be collected and directed towards the contact by the electric field generated in the depletion region of a $p-n$ junction. In a photodiode, the electric current will be proportional to the power of the absorbed light.

Solar cells, for example, exploit the properties of p-n junctions to generate electric power from the absorption of light. When the photodiode is set into a particular configuration, a voltage build-up in the forward direction appears and the electric power can be extracted from illuminating the junction. The photodiode is operated then in the photovoltaic mode. If on the other hand, the diode is reversely biased, the depletion region will increase and that can benefit the response time of the detector. Operating in this regime also implies dealing with the dark current, which can limit the performance of the device.

One can reduce the effective dark current by placing a barrier layer that blocks the flow of majority carriers. By doing that, it is possible to selectively filter the majority carrier contribution in certain space regions. This is the approach chosen in this work and a more detailed explanation of this kind of photodiodes will be presented in the upcoming section.

If the operational conditions of the photodetector in terms of reverse bias are pushed, new phenomena will appear. At high reverse bias, the electric field inside the device will be high enough to trigger carrier multiplication processes. The internal gain can enhance the properties of the photodetector. This avalanche process of carrier multiplication gives the name to the detectors, Avalanche photodiodes (APD).

2.4.3 Photodiode Architecture and Technology

The design of a suitable photosensor should be closely linked to the requirements needed for its application. The desired dark current levels, target spectral range and device's responsivity are going to set the standards for the technology employed in the detector as well as the architecture approach one should follow.

PIN photodiodes

The PIN photodiode is the most basic and known architecture approach when it comes to light sensing. The combination of materials with $n-$type and $p-$type dopants is going to translate into the appearance of a depletion region: a spatial region empty of mobile carriers with a strong electric field. Photogenerated carriers one diffusion length away from the edges of the depletion region are going to be swept by the field into one of the contacts.

From this simple principle, many variations have been introduced throughout the years. Doped semiconductor absorption layers have been substituted by more complex heterostructures, such as

type II superlattices, that can offer better performance in terms of dark current. In order to push the detection limits of the basic PIN photodiodes, modifications in the device's architecture have also been made. One of them is the presence of a unipolar barrier to block the flow of majority carriers and deactivate its contribution to the dark current. This work is based on the idea of such kind of photodetectors and in the upcoming pages, a more detailed explanation of the working principles of these devices will be given.

Avalanche photodiodes

Avalanche photodiodes (APD) are one of the primary device structures for sensing IR radiation. The operational conditions of this architecture make them suitable for low-light-level applications. APD have the particularity to overcome the unitary-gain condition of many photodetectors.

In the absorber layer of the APD, an EHP is generated upon the absorption of a photon. The photogenerated carriers, however, are accelerated by a high electric field. If the carriers gain enough kinetic energy they are able to create another EHP from a collision with a bound electron. Therefore, each absorbed photon in the absorber layer will generate an EHP that will create M secondary EHP increasing the photocurrent substantially.

The amplification of the photocurrent, however, is limited by the stochastic nature of the multiplication process. The first theoretical description of the carrier multiplication was done by McIntyre [15]. In his Local Field Model, McIntyre inspected the properties of the multiplication gain and introduced the excess noise factor, which limits the detectivity of the device.

Assume that an electron-hole pair is generated in the absorber layer of an APD by an incoming photon. This electron will naturally travel within the material undergoing several scattering events, however, in the presence of an electric field, the carrier will be accelerated and gain some kinetic energy. If the energy of this primary electron, E_1, is higher than E_g it will be able to generate another EHP through a collision with another electron. This process is called impact ionization. The secondary electron promoted to the conduction band will also undergo a similar process, generating an avalanche of EHP generated with a single absorbed photon.

To characterize the ionization events, it is useful to introduce the impact ionization coefficients, which describe how often a carrier suffers from an ionizing collision within the material. The expression for the impact ionization rates for electrons (α) and holes (β) are shown below. α and β increase with the electric field as the carriers need to travel a shorter distance before undergoing an ionizing scattering event [16]. On the other hand, α and β tend to decrease as a function of temperature because the energy of the carriers is delivered mainly to the crystal lattice [17].

$$\alpha = \alpha_0 \cdot exp(\frac{-E_0}{E}) \tag{2.23}$$

$$\beta = \beta_0 \cdot exp(\frac{-E_0}{E}) \tag{2.24}$$

$$k = \frac{\beta}{\alpha} \tag{2.25}$$

A representative material parameter for APD is the *k-ratio* as it determines the device bandwidth and noise levels [16]. For materials that use electrons as the main multiplying carrier, as is the case for InAsSb alloys, the aim is to look for $k \sim 0$.

The excess noise factor F described by McIntyre [15] is a function of the *k-ratio* and the multiplication gain (M). Suitable materials for APD are desired to have the lowest possible *k-ratio* values, thus, the multiplication gain can be pushed higher without increasing the excess noise factor and the noise signal. McIntyre's equation of the excess noise factor is shown below.

$$F(M) = kM + (1-k)(2 - \frac{1}{M}) \tag{2.26}$$

As good as McIntyre's avalanche theory [15] is, it does not take into account the dead-space effect introduced by Hayat et al. in 1992 [18]. This non-local model incorporated the carrier history into the calculations [19]. This means that a newly generated carrier from an ionization process must travel a certain distance to acquire enough kinetic energy to contribute to ionization itself, such distance is called the dead-space [18]. The dead-space effect enables the excess noise factor F to go below 2, which is the limit imposed by the McIntyre theory ($F = 2,\ when\ k = 0\ and\ M = \infty$ in the equation above).

The first reported APDs were rather simple structures. The devices resembled PIN diodes in which the photon absorption and the multiplication happened in the same layer [20, 21]. To achieve multiplication gain, a high electric field is required, consequently, strong band-to-band tunnelling can also appear, leading to a rapid increase of the dark current.

In addition to that, materials with good *k-ratio* may not be suitable to sense in a specific IR range, or the other way around, materials with a desired band gap and absorption coefficient may not show good multiplication characteristics. To solve these problems, another approach was taken, and the structure was provided with separated layers for absorption and multiplication, enabling a higher degree of tunability for APDs. This device architecture is the so-called Separate Absorption Charge Multiplication layer avalanche photodetectors or SACM APDs.

The working principle of the SACM photodiode is quite similar to a regular PIN diode in the avalanche operational regime. The difference is that now the photogenerated carriers will be swept through a high electric field layer before the multiplication can happen. Different spatial regions for different functions within the photodiode have direct benefits in the applicability of the device while opening the door to incorporate better-suited materials that can optimize the performance of the detector.

Type II Superlattice Absorbers

As firstly proposed by Sai-Halasz et al. in 1977 [22], *Type II* superlattices (T2SL) take advantage of the band alignment between semiconductors to exploit new properties in solid-state based opto-electronic devices. In this heterostructure, the conduction and valence band of the semiconductors follow the *type II* alignment presented in Section *Heterostructures and Heterojunctions - Types of Alignment* of Chapter 2. In T2SL, the CB of one of the semiconductors is located very close (type II) or even below (type III) the VB edge of the other semiconductor. With this new band structure arrangement is possible to confine the electrons and holes wavefunctions in the different materials.

T2SL properties can greatly differ from their bulk constituents, thus, allowing another degree of tunability to the device structure and give rise to new optical and electrical properties [22]. For example, the band gap of the T2SL is defined by the difference in energy between the first electron level in the conduction band (C1) and the highest heavy-hole level in the valence band (HH1). The energy of the band gap can be tuned by choosing the proper substrate and coherently straining the lattice [23]. Another property that can be enhanced in the T2SL is the carrier lifetime, as the spatial separation of carriers due to the band structure can effectively suppress the Auger recombination processes[24].

Superlattice's period, layers' thicknesses, and Sb molar composition are the main parameters to play with when designing an InAs/InAsSb T2SL absorber [23]. The absorption coefficient, for example, is very dependent on the superlattice period. Shorter periods give better absorption coefficient as the carrier wavefunction is enhanced by thinner semiconductor layers, however, as InAs and InAsSb are not closely lattice-matched, shorter periods give rise to higher strain in the

growth direction reducing the minority carrier lifetime and the Quantum Efficiency (QE) [25].

Another issue that reduces InAs/InAsSb T2SL integration possibilities is the Fermi level surface pinning over the conduction band minimum. That is an added difficulty to its viability for being incorporated in APDs, where the required dopant type is p (as $k \sim 0$ and the impact ionizing carrier will be electrons). Having opposite conductivity types in the bulk and the surface will create dark current pathways at the surface if the device is not properly passivated.

2.5 nBn Photodetector

The previous section was a brief introduction to the different sort of photodiodes one can encounter as well as some of the technological approaches that are being used nowadays. When talking about PIN photodiodes, the possibility to introduce a unipolar barrier into the heterostructure to reduce dark current densities was mentioned. This thesis has focused on the study of such photosensors and developing a reliable simulation script to predict the behaviour of barrier photodetector in different conditions. The following section contains an overview of the working principles, the advantages of general barrier photodiodes and a detailed description of the designed detector, highlighting the role of the constituent layers and the materials of choice.

2.5.1 Working Principle

In its structural aspects, Unipolar Barrier Infrared Detectors (UBIRD) resemble very much the regular PIN diodes. The electric field enclosed in a space charge region, resulting from a heterojunction, will help to sweep the photogenerated minority carriers to their corresponding contact. The difference is that the flow of majority carriers will be prevented due to the presence of large band gap material which serves as a potential barrier.

The potential barrier can act in the valence band, if the majority carriers are holes, or in the conduction band in the case that electrons appear to be the majority carriers. The selection of the dopant type in the detector's layers is not arbitrary at all, rather it is closely linked to the material choice. For this work, the absorber has been chosen to be the ternary alloy $\mathrm{InAs}_{0.91}Sb_{0.09}$.

InAsSb has proven to be a reliable material as an absorber for barrier photodetectors due to its band gap tunability with Sb molar composition and its good absorption characteristics. However, the InAsSb surface Fermi level is pinned above the minimum of the conduction band which can lead to surface current channels if the dopant type of the bulk differs from the n-type surface. Kopytko et al. [26] showed how the surface current for n-type absorber can be effectively reduced, with the bulk dark current being the only component for the dark current.

In comparison to MCT, InAsSb barrier photodetectors are more stable to higher temperature conditions. Additionally, the band gap is not so sensitive to composition inhomogeneities which makes them more reliable for mass production and the fabrication process is more flexible [27].

There are different approaches to incorporate this material into the photodetector structure. One possibility is to design a PIN-like diode with a barrier. With this architecture, a depletion region will appear at some interface giving rise to SRH generation-recombination processes that can minimize the efficiency of the design. The approach that was chosen for this work, however, is a so-called depletion-less barrier photodetector in which all the components have the same dopant type. A small charge transfer region will appear at the heterointerface between the absorber and the barrier layers [28]. In spite of that, the structure can reduce the GR mechanisms associated with the presence of a depletion layer. Including a wide band gap semiconductor in the barrier layer also reduces the effect of misfit dislocations to the dark current in comparison with conventional $p-n$ junctions [29, 30, 31].

Unipolar barriers are not the only engineering solution that has been proposed for reducing dark

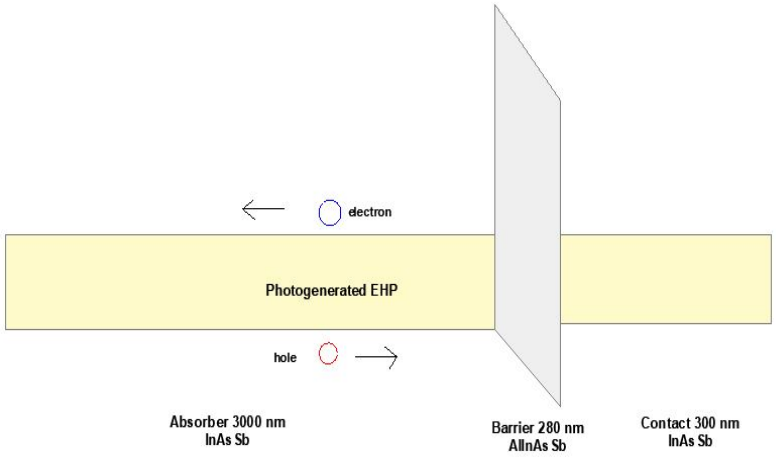

Figure 2.6: Schematic of the carrier collection of the nBn photodetector.

currents. Usually associated with *type II* superlattices, these strategies consist of introducing wide band gap materials between the superlattice semiconductors to modify the envelope wavefunction overlap of holes and electrons. These variations are named W [32], N [33] or M [34] due to the shape the barrier gives to the band structure. Ting et al. [35] proposed in 2009 a heterostructure with both hole and electron barrier (CBIRD), this approach, also targeted to T2SL absorbers, showed great current responsivity at 77 K. However, bulk photodetectors have a better performance in terms of dark current densities and quantum efficiency than T2SL, Quantum Wells Infrared Photodetectors (QWIP) and Quantum Dots Infrared Photodetectors (QDIP) [36], especially at High Operating Temperatures (HOT). Another characteristic that makes UBIRDs especially interesting is the possibilities they offer in terms of multi-colour functionality, that is to say, the same heterostructure is capable of precisely detect different spectral regions just by changing the biasing conditions [29, 37].

Taking those factors into consideration, the best architecture choice to incorporate bulk InAsSb as the absorber material is an nBn photodetector, with the collector, barrier and absorber having all $n-type$ conductivity.

For an nBn photodetector, an EHP will be created upon the absorption of an incoming photon in the InAsSb layer. From there, electrons and holes will move to opposite sites of the structure. In a barrier photodetector, a wide band gap material is incorporated into the structure to block the majority carrier flow to the absorber layer. Holes will move to the barrier layer and will be collected at the n-type contact. A schematic of the device basic working principle is shown in Figure 2.6

An important consideration when choosing a suitable barrier material for the heterostructure is to minimize valence band offset at the absorber-barrier and barrier-contact junction. By doing that, one ensures that no hole-block barrier appears at the heterojunction. This would result in difficulties to the minority carrier collection process [38]. To combine with InAsSb, usually, the preferred materials are binary, ternary or quaternary alloys containing Al and Sb which ensures large band gaps and tunable VBO with composition [28, 39, 40].

2.5.2 Material System

InAsSb-based infrared photodetectors research began back in the 1970s when they were grown by Liquid Phase Epitaxy (LPE) [41]. Later, it was shown that nearly lattice-matched InAsSb on GaSb produced the best detector characteristics [42]. InAsSb band gap's tunability makes it

suitable for detecting in both LWIR and MWIR spectral ranges [9].

Lattice Constant

The lattice constant of the ternary alloy can be obtained by linear interpolation taking into account the parameters of the binary compounds [43], in this case, InAs and InSb. That is to say,

$$a_{InAsSb} = a_{InAs}(1 - x_{Sb}) + a_{InSb}x_{Sb} \tag{2.27}$$

Parameter	$InAs$	$InSb$
a	6.0853 Å	6.4794 Å

Table 2.1: Lattice parameters for InAs and InSb.

GaSb has a lattice constant equal to 6.1 Å, to obtain the lattice-matchig condition the molar fraction has to be $x_{Sb} = 0.09$. The values in Table 2.1 have been taken from [44].

Band gap

In 1973, Wieder and Clawson [45] derived an equation for the band gap of InAsSb as a function of molar composition, x_{Sb} and temperature, T. The band gap for the InAsSb-based contact and absorbtion layers has been parametrized using the expression shown below,

$$Eg(x,T) = 0.411 \; - \; \frac{3.4x10^{-4}T^2}{210+T} \; - \; 0.876x_{Sb} \; + \; 0.70x_{Sb}^2 \; + \; 3.4x10^{-4}x_{Sb}T(1-x_{Sb}) \tag{2.28}$$

Valence Band Offset

The valence band offset between the absorber and the barrier layer is presumed to have a big importance in the carrier transport of the device. To calculate the VBO of InAsSb as a function of the molar composition, one can use a linear interpolation taking the parameters for the binary semiconductors, InAs and InSb, and the bowing parameter C_{InAsSb}.

$$VBO_{InAsSb} = VBO_{InAs}(1 - x_{Sb}) + VBO_{InSb}x_{Sb} - C_{InAsSb}x_{Sb}(1 - x_{Sb}) \tag{2.29}$$

	VBO_{InAs}	VBO_{InSb}	C_{InAsSb}	VBO_{InAsSb}
Parameter (eV)	-0.59	0.00	-0.40	-0.50

Table 2.2: Parameters used in the equation above to calculate VBO_{InAsSb} for $x_{Sb} = 0.09$. The VBO have been calculated taking InSb valence band edge as a reference.

Using the parameters listed in Table 2.2 and $x_{Sb} = 0.09$ in Equation 2.29, it is possible to obtain VBO_{InAsSb}. The values in Table 2.2 have been extracted from [46].

As shown by Martyniuk and Rogalski [28], the CBO at the AlAsSb-InAsSb interface remains basically constant with temperature. A similar assumption has been made at the AlInAsSb - InAsSb heterointerfaces, so the expansion or shrinkage of the InAsSb band gap will only affect the VBO. The band gap of AlInAsSb has been assumed to remain constant with temperature. In this way, VBO_{InAsSb} (T) can be calculated the following way,

$$VBO_{InAsSb}(T) = VBO_{InAsSb}(300K) - (E_{g_{InAsSb}}(T) - E_{g_{InAsSb}}(300K)) \tag{2.30}$$

Calculating the VBO for InAsSb is important, however, the factor with a greater influence on the current of the detector is the relative displacement between VBOs of different materials, in this case, InAsSb and AlInAsSb. In a quaternary alloy, $A_{1-x}B_xC_{1-y}D_y$, the VBO of each material with respect to InSb can be obtained as a function of the constituents molar fractions as it follows [43],

$$VBO_{ABC} = VBO_{AC}x + VBO_{BC}(1-x) - b_{ABC}x(1-x) \tag{2.31}$$
$$VBO_{ABD} = VBO_{AD}x + VBO_{BD}(1-x) - b_{ABD}x(1-x) \tag{2.32}$$
$$VBO_{ACD} = VBO_{AD}y + VBO_{AC}(1-y) - b_{ACD}y(1-y) \tag{2.33}$$
$$VBO_{ABC} = VBO_{BD}y + VBO_{BC}(1-y) - b_{BCD}y(1-y) \tag{2.34}$$
$$\tag{2.35}$$

$$VBO_{ABCD} = \frac{(x(1-x))(yVBO_{ABC} + (1-y)VBO_{ABD})}{x(1-x)+y(1-y)} + \frac{(y(1-y))(xVBO_{ACD} + (1-x)VBO_{BCD})}{x(1-x)+y(1-y)} \tag{2.36}$$

For $Al_{1-x}In_xAs_{1-y}Sb_y$, the parameters to calculate the VBO are shown in Table 2.3 and the results in Table 2.4. All parameters, but the AlInAsSb band gap [47], have been taken from [46].

	$AlAs$	$AlSb$	$InAs$	$InSb$
VBO (eV)	-1.33	-0.41	-0.59	0.00
	b_{AlInAs}	b_{AlInSb}	b_{AlAsSb}	b_{InAsSb}
VBO bowing parameter (eV)	-0.64	-0.1	-1.71	-0.40

Table 2.3: VBO (top) of different materials and their VBO bowing parameter (bottom). They were used for calculating AlInAsSb VBO as a function of the constituents' molar fractions. The VBO have been calculated taking InSb valence band edge as a reference.

Material	Eg (eV) at 300 K	VBO (eV)	x
InAsSb	0.291	-0.50	$x_{Sb} = 0.09$
AlInAsSb	1.16	-0.53	$x_{Al} = 0.7$, $x_{Sb} = 0.7$

Table 2.4: Band gap and VBO for the materials present in the photodetector. The VBO have been calculated taking InSb valence band edge as a reference.

The alignment between the bands of InAsSb and AlInAsSb will be *type I* at 300 K, however, as the VBO of InAsSb is dependent on temperature, the alignment will evolve to *type II* with cooling.

Carrier transport

Mobility in InAsSb has been found using linear interpolation as well. To calculate the carrier mobility at an arbitrary temperature, the strategy followed by Schuster et al. [48] was used. This way,

$$\mu_{e,h}(T) = \mu_{e,h}(300K)\left(\frac{T}{300}\right)^{-\zeta_{e,h}} \tag{2.37}$$

To calculate $\mu_{e,h}(300K)$, the parameters in Table 2.5, extracted from [48], were used. Once $\mu_{e,h}(T)$ is obtained, the value for InAsSb can be calculated by linear interpolation, similarly to the lattice

Material	T (K)	$\mu_e(cm^2/Vs)$	$\mu_h(cm^2/Vs)$	ζ_e	ζ_h
InAs	300	3 x 10^4	500	0.7212	0.5019
InSb	300	8 x 10^4	800	1.8572	1.8572

Table 2.5: Mobility parameters for InAs and InSb. InAsSb carrier mobility was calculated using linear interpolation with the values from the binary compounds.

constant calculation. After calculating the mobility, one can make use of the Einstein's relation $D = \mu\frac{k_bT}{q}$ to obtain the diffusion coefficients for both types of carriers.

As it will be explained later, the diffusion current will be limited by the intrinsic carrier concentration, n_i, of InAsSb. An explicit expression combining the molar fraction, the temperature and the band gap was described by Rogalski and Jóźwikowski in 1989 [49]. Such equation has been used to describe n_i in the absorber and it is shown below,

$$n_i(x,T) = (1.35 + 8.50x_{Sb} + 4.22x10^{-3}T - 1.53x10^{-3}x_{Sb}T - 6.73x^2)x10^{14}T^{3/2}E_g^{3/4}exp[\frac{-E_g}{2k_bT}] \tag{2.38}$$

Absorption Coefficient

The absorption coefficient (α_{InAsSb}) has been modelled as shown by D'Souza et al. [50]. In their article, the absorption coefficient was described according to two situations. First, if $h\nu \leq E_g$

$$\alpha_{InAsSb} = 948.23\ exp[170(h\nu - E_0)] \tag{2.39}$$

$$E_0 = E_g + 0.001 \tag{2.40}$$

Then, in case $h\nu > E_g$

$$\alpha_{InAsSb} = 800 + \frac{K(h\nu - E_g - c)\sqrt{(h\nu - E_g - c)^2 - c^2}}{h\nu} \tag{2.41}$$

$$c = 0.5E_g + 0.1 \tag{2.42}$$

$$K = 10^4 + 2x10^4E_g \tag{2.43}$$

The only active layer in terms of photocarrier generation in the whole device is the absorber. It has been assumed that the contact layer has a negligible contribution in this regard.

2.5.3 Design Proposal

The photodiode simulated in this work is an nBn detector based on a double InAsSb-AlInAsSb heterojunction. The device would be grown on top of a GaSb substrate. At the right Sb molar fraction ($x_{Sb} = 0.09$), InAsSb will be lattice-matched to the substrate and its band gap within the MWIR spectral range. Epitaxial growth is decisive to ensure the performance of the device is optimized, note, however, that strain effects due to misfits have not been taken into account in the simulation.

The dopant density in the InAsSb-based absorption layer has been kept low to avoid Burstein-Moss effects once the device is illuminated. If N_d in the absorber is higher than the conduction band

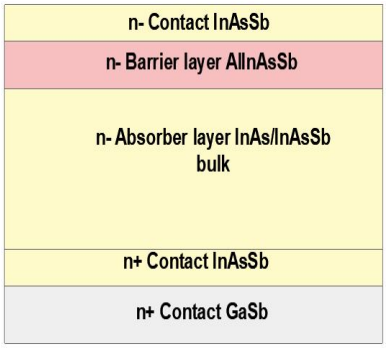

Figure 2.7: Layout of the proposed nBn barrier photodetector with bulk InAsSb as the absorber layer.

density of states, the Fermi level will lie within the conduction band energy range. This situation is called degenerate doping. From Pauli's exclusion principle it is known that an electron sitting in the valence band can only be promoted to a state above the Fermi level. Now, the conduction band edge is below E_f, so, the required energy coming from the illumination source needs to be greater than the bandgap by an amount equal to the Burstein-Moss shift. Klipstein et al. [51] showed the effects of high dopant densities in InAsSb. With the proposed N_D the Fermi level in the absorber should lie below the conduction band edge.

Table 2.6 shows the layer thicknesses and dopant densities for the nBn proposed structure. The barrier layer is AlInAsSb ($x_{Al} = 0.7\ x_{Sb} = 0.7$), this material has been chosen for two main reasons: first, it is lattice-matched to the absorber which enables to fabricate without buffer layers [52, 53]. On the other hand, AlInAsSb has a small VBO with InAsSb ($x_Sb = 0.09$) and introduces a big CBO offset that will prevent electrons to diffuse into the absorber. Figure 2.7 shows the different layers of the proposed nBn design.

The device has a $n+$ contact made of InAsSb that acts both as a collector layer for the photogenerated electrons and as a buffer layer to mitigate epitaxial strain between GaSb and the InAsSb absorption layer.

Layer	Material	Dopant level (cm^{-3})	Thickness (μm)
Substrate	$GaSb$	$1x10^{17}$	1.00
n+ contact	$GaSb$	$1x10^{18}$	0.30
n+ contact	$InAs_{0.91}Sb_{0.09}$	$5x10^{17}$	0.15
n- absorber layer	$InAs_{0.91}Sb_{0.09}$	$8x10^{15}$	3.00
n- barrier layer	$Al_{0.7}In_{0.3}As_{0.3}Sb_{0.7}$	$1x10^{16}$	0.28
n- contact	$InAs_{0.91}Sb_{0.09}$	$5x10^{15}$	0.30

Table 2.6: Structure for the nBn photodiode with bulk InAsSb absorber layer. Materials properties for each layer are indicated.

2.6 Recombination Mechanisms

Inside the photodetectors, carriers are photogenerated when an incoming photon is absorbed by the material. If $h\nu \geq E_g$, the photon is able to transfer its energy to a valence band electron and promote it to the conduction band, generating an electron-hole pair in the process.

A good photodetector must ensure a good carrier lifetime for the photogenerated EHP. The carriers should be able to diffuse towards the depletion region where they will be swept by the field to the

contacts. Different mechanisms can shorten the carrier lifetime and they can be originated from a quite broad range of sources: localized states due to defects or dopants, residual strain in the lattice, etc.

The carrier lifetime in the photodetector can be described through contributions of the different mechanisms:

$$\frac{1}{\tau} = \frac{1}{\tau_1} + \frac{1}{\tau_2} + \frac{1}{\tau_3} + \cdots \tag{2.44}$$

2.6.1 Shockley-Read-Hall Recombination

When charge carriers recombine and release a phonon instead of a photon, a non-radiative recombination process takes place. Shockley-Read-Hall (SRH) is a recombination mechanism that responds to this description. In SRH, the carrier recombines through localize states in the band gap of the material where they exchange energy with the lattice emitting a phonon and heat.

In MCT, large carrier lifetime have been observed for MWIR and LWIR [8]. However, Ga-free superlattices containing InAs/InAsSb have also shown great carrier lifetimes. By suppressing Ga from the structures and the trap states associated with this material, the carrier lifetimes are comparable to ones shown by MCT in MWIR [54, 55].

One approach to reducing SRH associated processes is to introduce a wide band gap barrier material. In this layer, the probability of half band gap trap states is lowered if the Fermi level is several k_bT far from the middle of the band gap [26]. nBn and other depletion-less device structures are suitable to prevent SRH recombination as they avoid the presence of depletion region where this mechanism is prominently effective [36].

This architecture without a depletion region prevents the Shockley-Read-Hall trap states to act as Generation-Recombination centres which are a primary source of dark current [56]. The suppression of this GR mechanism helps the device to work in a diffusion-limited situation and, therefore, they have a more reliable performance at higher temperatures and can exceed the detectivity limits of other heterostructures (standard $p-n$ diode) at low temperatures [56]. Shockley-Read-Hall recombination equation [50] is shown below, however, it has not been included in the final model as it has little influence in the dark current of the heterostructure as shown by Ting et al. [57].

$$U_{SRH} = \frac{np - n_i^2}{(p + n_i)\tau_{n0} + (n + n_i)\tau_{p0}} \tag{2.45}$$

2.6.2 Auger Recombination

In the Auger recombination process, the excess energy from the electron-hole recombination is transferred to another carrier, either an electron or a hole, that will be promoted to a higher energy state [54]. This phenomenon is especially important at higher temperatures as the number of free carriers increases. Auger transitions greatly depend on the carrier density of the material, in that sense, the high degree of tunability of III-V semiconductor superlattices appear to be suitable to engineer the band properties and suppress the Auger contributions to the carrier lifetimes [58].

Low Auger recombination rates are also observed for bulk InAsSb at 77K [24]. In fact, the carrier lifetimes for the bulk material appears to be greater than its superlattice counterparts, both with and without Ga [24].

In narrow band gap semiconductors, like InSb, Auger is predominant within the GR mechanisms [9]. There are different Auger-type processes for recombination depending on the shape of the bands involved. In n-type materials, as is the case for the InAsSb layers in this work, the primary

source of recombination is Auger 1. This process is dominant in InAsSb at high temperatures [9]. Auger 1 recombination mechanism, also called CHCC, involves two electrons and one heavy hole. Once the electron and the heavy hole have been annihilated, the excess of energy from the recombination goes to a third particle, the second electron, that will use it to increase its energy within the conduction band. The process is non-radiative as no photons are emitted from the recombination. The equations below show the Auger 1 recombination rate in cm^{-3}/s and the Auger carrier coefficients in cm^6/s [48].

$$U_{A1} = (C_n n + C_p p)(np - n_i^2) \tag{2.46}$$

$$C_n = \frac{(\frac{m_e^*}{m_0})|F_1F_2|^2}{2n_i^2(3.8x10^{-18})\varepsilon_\infty^2(1+\frac{m_e^*}{m_h^*})^{1/2}(1+2\frac{m_e^*}{m_h^*})}(\frac{E_g}{k_bT})^{-3/2}exp[-\frac{(1+2\frac{m_e^*}{m_h^*})E_g}{(1+\frac{m_e^*}{m_h^*})k_bT}] \tag{2.47}$$

$$C_p = C_n[\frac{1-\frac{3E_g}{k_bT}}{6(1-\frac{5E_g}{4k_bT})}] \tag{2.48}$$

In the Matlab model, Auger 1 has been considered as the limiting mechanism for the carrier lifetime in the InAsSb layers. Following Rogalski and Orman's approach [59], and considering that holes are the only carrier type that will be able to move around the heterostructure, the carrier lifetime τ has been calculated with the equations below [59]. τ_{A1}^i is the intrinsic Auger1 carrier lifetime and τ_{A1}^h takes into account the doping of the layer that is being treated.

$$\tau_{A1}^i = 3.8x10^{-18}\frac{\varepsilon_\infty^2(1+\frac{m_e^*}{m_h^*})^{1/2}(1+2\frac{m_e^*}{m_h^*})}{(\frac{m_e^*}{m_0})|F_1F_2|^2}(\frac{E_g}{k_bT})^{3/2}exp[\frac{(1+2\frac{m_e^*}{m_h^*})E_g}{(1+\frac{m_e^*}{m_h^*})k_bT}] \tag{2.49}$$

$$\tau_{A1}^h = \frac{2\tau_{A1}^i}{1+(\frac{n_0^2}{n_i^2})} \tag{2.50}$$

2.6.3 Surface-mediated Recombination

The discontinuity in the crystal lattice of semiconductors opens the door to trap states associated with dangling bonds. Surface states can lead to leakage paths that will greatly increase the dark current of the device.

That is particularly concerning for structures containing InAsSb alloys as its surface Fermi level is pinned above the conduction band minimum. Surface treatments appear to be necessary for $p-$type InAsSb as these conductive pathways can ruin completely the performance of the device [60, 61]. For $n-$type structure, this contribution is neglected and in addition to that, nBn InAsSb has also shown smaller values of surface current density than MCT detectors [26]. Interfacial defects have also been reported as a limiting factor for reducing the dark current in InAs/InAsSb superlattices [62].

The surface leakage current is expected to come from surface states and its magnitude depends on the position of the surface Fermi level [26]. For InAsSb, the surface Fermi level is pinned above the conduction band minimum, giving it a $n-$type character [26]. To reduce the leakage current coming from the surface states, it is important to keep the same conductivity type in the bulk of the material and at the surface. This is a reason behind the choice of $n-$doped character of

the constituent layers of the device. This way, the unipolar barrier does not only block the bulk current but also the surface contribution [63, 64].

Due to the ability of the nBn heterostructure to neglect certain components of dark current, this architecture can operate with less noise, and work at higher temperature with the same performance, or have a better performance at the same temperature as conventional diodes [36].

2.6.4 Radiative Recombination

Following Bellotti and D'Orsogna model for MCT [65], radiative recombination has been introduced into the nBn solver. This mechanism occurs when an electron in the conduction band and a hole in the valence band recombine, then, a photon is emitted as a consequence of the excess of energy.

Although, the carrier recombination due to this process is not as dominant as Auger 1 it has been included in the model. In the equation below, are shown the band-to-band recombination rate U_R and the band-to-band recombination coefficient B_R from [65].

$$U_R = B_R(np - n_i^2) \tag{2.51}$$

$$B_R = 5.8x10^{-13}\varepsilon_\infty^{1/2}(\frac{m_0}{m_e^* + m_h^*})^{3/2}(1 + \frac{m_0}{m_e^*} + \frac{m_0}{m_h^*})(\frac{300}{T})^{3/2}(E_g^2 + 3k_bTE_g + 3.75k_b^2T^2) \tag{2.52}$$

2.7 Dark Current

Dark current is one of the primary figures to look at when comparing photodetectors. Higher dark current levels are undesirable for sensors as they increase the noise level and hinder the acquisition of a meaningful signal. Dark current arises in photodiodes as a result of the thermal generation of EHP in the depletion region and steadily increases when the device is reversely biased. The above-described recombination mechanisms can be acknowledged as the primary sources for dark current.

SRH is very active in depletion regions as mid-gap trap levels are activated, and is the main responsible for dark current in MWIR devices at low temperatures. Diffusion current is related to the Auger recombination process. The thermal generation of holes in the absorption layer of the device will add up to the dark current. As explained before, surface leakage current is another important contribution to the dark current.

The goal, when designing a photodetector, is to make it work in the so-called background limited infrared photodetection (BLIP) conditions. In this operational regime, the dark current is smaller than the photocurrent generated by the background environment. Accessing this operational regime becomes more and more challenging when the temperature increases as the Auger recombination mechanism starts to dominate.

Barrier photodetectors are one of the best structure options when aiming to reduce dark current contributions. nBn designs are able to minimize the impact of SRH by avoiding the depletion region as the materials that are brought together have the same dopant type [36]. nBn photodetectors also are capable of eliminating the surface leakage current by choosing a suitable fabrication protocol [26, 36, 60]. Unlike in common $p-n$ diodes, where the small band gap semiconductor sidewalls are exposed after etching, the nBn design allows a shallow etch, leaving the wide band gap material exposed where the dark current is suppressed. Thus, if the structure is designed properly, the barrier layer can act as a cap over the absorber with no need for additional passivation [29, 57, 66].

The unipolar barrier prevents the flow of electrons from the $n-$ contact layer. This way, any injected or thermally generated electron will be stopped at the InAsSb-AlInAsSb junction and eventually recombine, leading to 0 net current coming from that layer [57].

As mentioned before, the dark current contribution from SRH recombination is mostly suppressed with the nBn architecture and the dark current is mainly diffusion-limited [56]. Klipstein et al. reported such behaviour in a depletion-less photodetector with a $n-$type AlAsSb. The device showed a diffusion-limited performance up to 180 K at high biases [51]. This was confirmed as the activation energy was approximately the size of InAsSb band gap at 0K and satisfying the relation $J \sim exp(-E_g/k_bT)$. In a diffusion-limited semiconductor, the saturation dark current density follows the equation

$$J_D = q\frac{n_i^2}{N_D}\frac{L_{Diff}}{\tau}\frac{\beta + \tanh(\frac{W_{AL}}{L_{Diff}})}{1 + \beta\tanh(\frac{W_{AL}}{L_{Diff}})} \tag{2.53}$$

Where N_D is the donor density of the absorption layer, L_{Diff} is the diffusion length in that same layer, τ is the minority carrier lifetime, W_{AL} is the absorber layer width and β is the surface recombination velocity. The boundary conditions impose the hole current to be 0 at the absorber-contact interface, thus, the β term can be neglected [51]. Also, the valence band potential barrier that appears as a result of the electrostatics of the junction should be taken into account. Only thermally/photogenerated holes in the absorber with enough kinetic energy to traverse the barrier, $E_{hole} \geq E_{barrier} - 3k_bT$ will contribute to the dark current [56]. As a result, the dark current will be described by the following equation

$$J_D = q\frac{n_i^2}{N_D}\frac{L_{Diff}}{\tau}\tanh(\frac{W_{AL}}{L_{Diff}})exp(\frac{E_{barrier} - 3k_bT}{k_bT}) \tag{2.54}$$

2.8 Contacts

Designing a good device architecture can be in vain if no attention is paid to how the collection of the photocurrent will happen. In this section, a brief explanation on some contacts considerations is given and how they can affect the performance of the photodetector.

Ohmic contacts appear to be a great source of recombination processes, thus, it is desirable to isolate them from active areas [67]. Although the scope of this project is not to dig deep into microfabrication considerations, some aspects need to be taken into account. By photolithographic processing, it is possible to displace the optical active regions from the Ohmic contacts and improve the photodetector's response [67]. The geometry of the mesa shape can have some influence in the dark current, as current crowding has been observed in square geometries [68].

At the Ohmic contacts, by definition, the excess carrier density is 0, which pushes the surface recombination velocity up to infinity, drastically reducing the carrier lifetimes [67]. To prevent that from happening, n-n^+ contacts seem to be a solution as they create an energy barrier for minority carrier diffusion, without disturbing majority carrier flow [67]. These blocking contact types are named Hi-Lo blocking contacts (HLBC), in which the difference of dopant density helps to enhance the carrier lifetime and appear to be the most suitable according to the design goals set for this work.

2.9 Newton-Raphson Method

The script presented in this work makes use of the Newton-Raphson method for finding the roots of the Poisson and continuity equations and gives a solution to the spatial distribution of the potential (V) and the hole quasi-Fermi level (E_{f_h}).

The procedure is named after Sir Isaac Newton [69] and Joseph Raphson [70], who published a method for solving polynomial equations in the late 17th century. The Newton-Raphson method is a root-finding algorithm that iteratively produces better approximations to the roots or zeroes of a real function.

Function f is defined for a real variable x. In order to find a zero for the function x, an initial guess is made, x_0. If the initial guess is close to the root, we will find that x_1 is a better approximation of the root than x_0. x_1 and x_0 are related by the following expression:

$$x_1 = x_0 - \frac{f(x_0)}{f'(x_0)} \tag{2.55}$$

This process can be repeated until some convergence criteria is met. The solutions after each iteration are described as follows,

$$x_n = x_{n-1} - \frac{x_{n-1}}{f'(x_{n-1})} \tag{2.56}$$

The Newton-Raphson method uses the Taylor series expansion to iteratively shape the initial guess into the definitive solution [71]. Following the notation previously used, consider the set of equations:

$$f_i(x) = 0, \; where \; i = 0, 1, 2, ..., N \tag{2.57}$$

Here, x is a vector with N components and x^0 is the proposed initial solution for the above equation. After the k-th iteration of the Newton-Raphson solver, the N-dimensional vector is going to be x^k and the k+1-th solution vector will be

$$x_j^{k+1} = x_j^k + \Delta x_j^k \tag{2.58}$$

Δx_j^k is the j-dimensional correction vector, with $j = 0, 1, 2, ...N$, that drives the consecutive iterations closer to convergence with each new step and is the solution of the linear equation

$$f_i(x^k) + \sum_{j=1}^{N} \frac{\partial f_i}{\partial x_j}|_{x^k} \; \Delta x_j^k = 0 \tag{2.59}$$

Δx_j^k is going to be the working horse of the solver as it can be put into a system of equations in matrix form that can be solved in Matlab. Additionally, Δx_j^k will define the convergence criteria of the loop. In that sense, when the error of approximation at iteration k is lower than a predetermined tolerance, the solution will be considered as converged [71]. The equation below shows how to calculate such an error.

$$error^k = \sqrt{\frac{1}{N} \sum_{j=1}^{N} (\Delta x_j^k)^2} \; \leq tolerance \tag{2.60}$$

2.10 Finite Difference Method

To solve the Poisson and continuity equations numerically, one can discretize them into finite steps across the heterostructure with uniform spacing. The different parameters of the materials

composing the device will be defined in a one-dimensional grid and the above-mentioned equations are solved for each point by algebraic equations that contain the finite differences and the values of neighbouring grid points. By implementing this method, one can define the gradient of a quantity with the following equation

$$\frac{\partial f}{\partial x} \approx \frac{f_j - f_i}{\Delta} \tag{2.61}$$

i and j are the neighbouring points of the grid and delta is the spacing between them. In a similar manner, it is possible to write the second derivative

$$\partial(\frac{\partial f}{\partial x}) \approx \frac{f_i - 2f_j + f_k}{\Delta^2} \tag{2.62}$$

Equations 2.61 and 2.62 will be largely used to describe the Poisson and continuity equations within the Newton-Raphson approach, as will be explained in the upcoming chapters.

3. Poisson - Continuity Solver

The following chapter contains a detailed description of the Poisson-continuity solver that is the core of this work. In the upcoming lines, the constituent blocks of the script will be broken down, highlighting the aim and importance of such parts in the final form of the algorithm. The script was written in Matlab R2017b and run on the author's personal laptop.

The motivation behind writing the script was to represent the band structure of the device in an accurate way to access the characteristics of the design and, from there, check the reliability of the nBn photodetector proposed in an earlier report. Once the behaviour of the device has been depicted, the solver opens the door for optimisation of the design in a quick way as the multiple parameters that influence its performance can be modified easily. The Poisson-continuity solver aims to be a helpful tool for the design of this kind of photodetector.

The solver makes use of the equations described in chapter 2 and follows the Newton-Raphson approach to determine the electrostatic potential and hole quasi-Fermi level position across the device. Once these quantities are computed, the carrier distribution and band structure are calculated. As explained before, the solver uses the finite difference method to numerically solve the Poisson and continuity equations.

Before getting deep inside into the details of the solver, some of the general assumptions that were made to construct the script must be addressed.

- The lattice temperature is assumed to be the environmental temperature at which the device is sitting. No hot carrier effects were considered.
- Full ionization of dopants is assumed. It would be noted later when the Poisson Equation is treated, that the effective dopant concentration is equal to the dopant concentrations at each material layer. As all the layers are doped with donors, $N_{dop} = N_d$.
- The band gap of InAsSb changes with temperature and it translates only in changes on the valence band offset between the materials.
- Applied bias drops within the boundaries of the barrier layer.
- No Generation-Recombination processes are assumed to happen within the barrier layer width.
- Illumination happens uniformly in the absorber. At every point, the optically-generated carrier concentration is the same.

3.1 Material Parameters

In the first block of the script, the meaningful parameters for the simulation are listed along with the physical constants necessary for the calculations. The device's geometrical parameters, the thicknesses of the corresponding layers, are also listed in the first lines of the code as well as the environmental conditions at which the simulation is targeted: applied bias, temperature and conditions of illumination.

Once the conditions for each layer are set, the script includes a *for loop* that creates a series of matrices for each parameter with N_{points} + 2 rows. N_{points} is a variable that includes the sum of the thicknesses for each layer, $N_{points} = t_{CL} + t_{BL} + t_{AL}$. The thickness of each layer is given in nm. The reason to extend the simulation points to N_{points} + 2, one at the contact layer edge and another at the absorber layer edge, answers the need to account for the boundary conditions in the calculation of certain parameters and obtaining numerically the derivatives at the ends of the device. The loop is equipped with conditional *if* statements that ensure that the right material parameters are described in the right simulation points, according to the predefined architecture of the device.

With this loop, one can ensure that all the parameters necessary for the simulation are well described across the whole length of the device. The initial values for the most important variables to start the Poisson solver are defined in this loop. Other quantities, like the electron and hole densities for the isolated materials, are also initially set up here. It is important to mention that in this loop, the materials that form the heterojunction are not considered to be in contact, so it is their bulk properties that are being treated. Far from the junctions, the material properties for InAsSb, both in the contact and absorber layers, need to match their correspondent isolated bulk values, otherwise, the reliability of the simulation diminishes once the whole device is taken into account. Table 3.1 summarizes the parameters used for each of the layers taken into account in the simulation.

Parameter	n- absorber layer	n- barrier layer	n- contact
Material	$InAs_{0.91}Sb_{0.09}$	$Al_{0.7}In_{0.3}As_{0.3}Sb_{0.7}$	$InAs_{0.91}Sb_{0.09}$
Band gap 300 K (eV)	0.286	1.160	0.286
N_d (cm^{-3})	$8x10^{15}$	$0.1 - 2x10^{16}$	$5x10^{15}$
ε_r	15.298	15.500	15.298
m_h^* (kg)	$0.416m_0$	$0.350m_0$	$0.416m_0$
m_e^* (kg)	$0.0197m_0$	$0.0710m_0$	$0.0197m_0$
μ_h 300 K (cm^2/Vs)	527	3000	527
μ_e 300 K (cm^2/Vs)	34500	-	34500
D_h 300 K (cm^2/s)	13.636	77.625	13.636
D_e 300 K (cm^2/s)	892.687	-	892.687

Table 3.1: Material parameters used for each layer in the Poisson-continuity solver.

3.2 Initial Guess

As mentioned before in chapter 2, the Newton-Raphson feeds from an initial guess made on the variables that are involved in solving Poisson and continuity equations. To build up this initial state, a *for loop* runs for the $N_{points} + 2$ length of the simulation. The initial guess also contains information about the generation-recombination processes as a function of the initial carrier distribution.

This first guess considers the heterojunction to be set, so the materials have already been placed in contact with each other. From there, an electrostatic potential profile arises as a result of the bulk built-in voltages that should appear in the device, given the material characteristics of the different layers. Since the dopant densities of the contact and absorption layer are different, the built-in voltages will also be different. To ensure the continuity of the electrostatic potential in the heterostructure, there will be a gradient in the initial voltage across the AlInAsSb layer represented by the linear function below.

$$V_B^i L = V_{bi_1} - m * x \qquad t_{CL} + 1 < x \leq t_{CL} + t_{BL} \tag{3.1}$$

$$m = \frac{V_{bi_1} + V_{bi_2}}{t_{BL}} \tag{3.2}$$

V_{bi_1} is the built-in voltage that appears at the contact layer - barrier layer junction, while V_{bi_2} represents the built-in voltage arising between the barrier layer and the absorber. The gradient of voltage is represented by the slope of Equation 3.1, which takes into account the difference in the magnitude of these two quantities. The negative sign of V_{bi_2} has been considered in the expression above. Figure 3.1 shows the initial guess potential profile at $V_{app} = 0V$ and $V_{app} = -0.3V$.

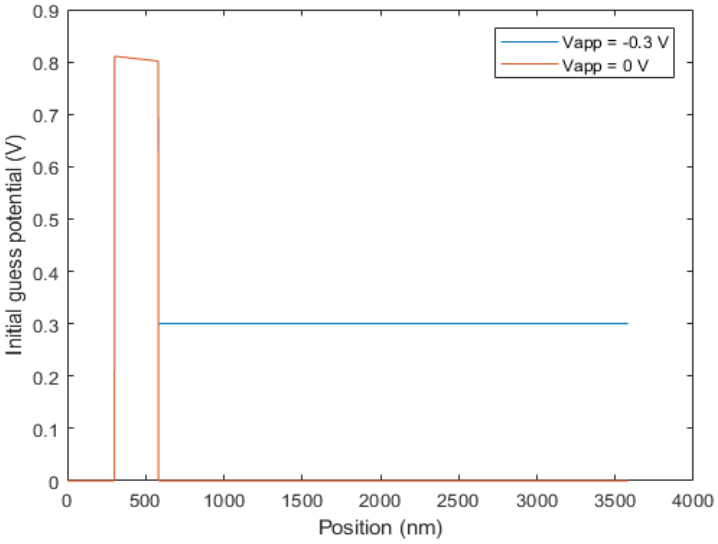

Figure 3.1: Initial guess potential profile across the heterojunction at two different applied bias. The electrostatic potential in the contact and barrier layers is the same at different V_{app} and their curves are superimposed. Therefore, only the function at $V_{app} = 0$ V is shown in those regions.

In the general remarks about the solver, it was pointed out that the entire potential drop from the applied bias was happening within the boundaries of the AlInAsSb electron barrier. This means that the potential difference between the edges of the barrier layer will be V_{app}. Accordingly, the absorber will be sitting at a constant voltage equal to that same value, and the built-in voltage at the barrier-absorber end will follow the expression: $V_{bi_2} = V^0_{bi_2} - V_{app}$, where $V^0_{bi_2}$ is the built-in voltage at equilibrium.

In the above-mentioned first *for loop*, the conduction and valence band profiles have also been calculated according to the dopant levels and intrinsic carrier concentration for the layers. The values are taken to construct an initial band profile. The effect of the applied bias on the band structure is to pull down $q * V_{app}$ (eV) the energy bands of the absorber.

The initial potential profile and band structure are the building blocks to determine the initial carrier concentration distribution. The carrier concentrations in the band edges at all points of the simulated heterostructure are calculated using FD statistics for holes and electrons in the contact and the absorber, and MB statistics for electrons in the barrier layer. As seen in the *Poisson Equation* section in chapter 2, to calculate the FD or MB distribution, the Fermi level plays a very important role. At thermal equilibrium, the Fermi level was set to an energy equal to 0 all across the structure and all the energy values have been calculated with the Fermi level as a reference. To avoid problems when the device is operating out of the equilibrium, the quasi-Fermi levels for holes and electrons have been defined.

The applied bias will split the hole and electron quasi-Fermi levels and since the voltage drop from the applied bias is assumed to be entirely constricted to the barrier layer, the split of Fermi-levels will mainly happen there. Following Rogalski's *et al.* [28] approach, the electrons in the barrier and absorption layer are assumed to be in equilibrium with each other and the only discontinuity in the electron quasi-Fermi level is happening at the contact-barrier junction. Meanwhile, the hole quasi-Fermi level is considered to vary linearly across the AlInAsSb layer as an initial guess, and to be constant through the absorber layer, sitting at an energy equal to qV_{app} eV.

This way, the linear function that describes the quasi-Fermi level in the barrier layer is presented below.

$$E_{f_h} = \frac{qVapp}{BL} * x \qquad t_{CL} + 1 < x \leq t_{CL} + t_{BL} \tag{3.3}$$

If the equilibrium conditions are broken due to the presence of an incoming radiation, the EHP generation and will also produce a shift in the carriers' quasi-Fermi levels. For typical optical power densities, from 1 $\frac{nW}{cm^2}$ to 10 $\frac{mW}{cm^2}$, the majority carrier concentration will not be disturbed by the presence of the optically generated carriers. This is to say, that in the absorber, $\Delta n^{opt} << n^0$ and the electron quasi-Fermi level will remain pinned at its equilibrium value. The situation is different when minority carriers, holes, are considered. In this case, it is not possible to state that the optically-generated hole concentration can be neglected in comparison to the equilibrium hole concentration. The presence of these EHPs will push the absorber hole quasi-Fermi level closer to the valence band. Using, the FD distribution one can calculate the shift in E_{f_h} according to the theoretical optically-generated hole concentration in the valence band. If all the absorbed photons yield in a photogenerated EHP,

$$\Delta p^{opt} = \tau_h \ \alpha_{AL} \ \frac{P_{opt}}{E_{ph}} \tag{3.4}$$

Where, τ_h is the hole carrier lifetime in the absorption layer, α_{AL} is the absorption coefficient of InAsSb, P_{opt} is the optical power density and E_{ph} is the photon energy. Once Δp^{opt} is obtained, the FD distribution can be used to calculate the shift in the hole quasi-Fermi level, $\Delta E^{opt}_{f_{AL}}$, that the new hole concentration, $p = p^0 + \Delta p^{opt}$, will induce.

In this part of the script, the dependence of the carrier concentration with the electrostatic potential is introduced for the first time. In chapter 2, it was mentioned that the FD distribution was being used to describe hole concentration all across the structure and electrons concentration in the InAsSb-based absorber and contact. Meanwhile, MB statistics were being used in the AlInAsSb barrier. The electrostatic potential is going to have an impact on the bending of the bands, therefore, it has been introduced in the energy terms of the carrier distributions. Taking the equations presented in the *Poisson Equation* section of Chapter 2, for a bulk material, the hole density in the valence band will be,

$$p = N_v \frac{2}{\sqrt{\pi}} \int_{-\infty}^{0} \frac{\sqrt{-y}\ dy}{1 + exp(-(y + \nu))} \tag{3.5}$$

The integral term is called the Fermi-Dirac integral of order 1/2, $F_{1/2}(\nu)$ [72]. The energy terms are substituted by $y = (E - E_v)/k_bT$ and $\nu = (E_v - E_{f_h} - qV)/k_bT$, where ν includes the electrostatic potential term. N_v is the effective density of states described in the expression below.

$$N_v = 2(\frac{2\pi k_b T m^*_h}{h^2})^{3/2} \tag{3.6}$$

If one only looks at carriers sitting at the bottom of bands and making the assumption that in the bulk material such carriers have $\nu >> y$, Equation 3.5 can be simplified. For the case of holes, that means carriers within an average thermal energy distance of the valence band edge, $\overline{E_{thermal}} = 3/2k_bT$, will be accounted. The lower y limit is now going to be $-3/2$ since the lowest energy is equal to $E = E_v - \overline{E_{thermal}}$.

$$p \sim \frac{N_v}{1 + exp(-(E_v - E_{f_h} - qV)/k_bT)} \frac{2}{\sqrt{\pi}} \int_{-3/2}^{0} \sqrt{-y}\ dy \tag{3.7}$$

The integral part of the expression above can be approximated to 1. A similar process can be followed for electrons at the bottom of the conduction band.

$p(x_i)$ and $n(x_i)$ describe the hole and electron concentration at the band edges for each point of the heterostructure. The density of states has been approximated to the above-mentioned constant bulk density of states for each material in the heterostructure, N_v for holes and N_c for electrons. Expressions below depict such dependences.

$$p(x_i) \sim N_v(x_i)\ \frac{1}{1 + exp(-(E_v(x_i) - E_{f_h}(x_i) - qV(x_i))/k_bT)} \tag{3.8}$$

$$n(x_i) \sim N_c(x_i)\ \frac{1}{1 + exp((E_c(x_i) - E_{f_e}(x_i) - qV(x_i))/k_bT)} \tag{3.9}$$

$$n(x_i) \sim N_c(x_i)\ exp(-(E_c(x_i) - E_{f_e}(x_i) - qV(x_i))/k_bT) \tag{3.10}$$

The loop described above is the basis that sets the Poisson-continuity solver running. To reduce the computation time of the script, it is important to provide a good initial guess. The closer to reality the first input is, the fewer number of iterations will be necessary for the solver to converge.

3.3 Poisson - Continuity Solver

To numerically solve Poisson's equation, it is necessary to make use of the finite differences scheme previously presented in chapter 2. For that purpose, the device will be represented in Matlab by a one-dimensional grid with spacing Δ_x. Recall Poisson Equation, but now, the charge density ρ will be a function of the electrostatic potential at each point of the grid. The initial guess assumes that we know the potential everywhere in the device. This way, the Poisson Equation will turn into

$$\frac{\partial}{\partial x}\ [\ \varepsilon(x_)\ \frac{\partial V}{\partial x}\ ]|_{V_i}\ = -\ \rho(V_i) \tag{3.11}$$

Following the finite difference scheme previously introduced,it is possible to define the derivatives in the Poisson Equation the following way

$$\frac{1}{\Delta_x}\ (\Delta V_{i+1/2}\ \varepsilon_{i+1/2}\ -\ \Delta V_{i-1/2}\ \varepsilon_{i-1/2}) \tag{3.12}$$

Where,

$$\Delta V_{i+1/2} = \frac{V_{i+1}\ -\ V_i}{\Delta_x} \tag{3.13}$$

$$\varepsilon_{i+1/2} = \frac{\varepsilon_{i+1}\ +\ \varepsilon_i}{2} \tag{3.14}$$

Taking the expressions above, the left-hand side of the Poisson Equation becomes

$$s_i\ V_{i-1} -\ d_i\ V_i\ +\ s_{i+1}\ V_{i+1} = -\rho(V_i) \tag{3.15}$$

And the newly introduced parameters s_i and d_i can be expressed as follows,

$$s_i = \frac{1}{2\Delta_x^2}\ (\varepsilon_{i-1}\ +\ \varepsilon_i) \tag{3.16}$$

$$d_i = \frac{1}{2\Delta_x^2}\ (\varepsilon_{i-1}\ +\ 2\varepsilon_i\ +\ 2\varepsilon_{i+1}) \tag{3.17}$$

Similar approximations are made to obtain the correction factor that will push the Newton-Raphson-based solver. The correction factor comes from the Taylor's expansion series in Equation 2.59. In that sense, one will have that at the k-th iteration

$$-s_i\ \Delta V_{i-1}^k + d_i\ \Delta V_i^k\ -\ s_{i+1}\ \Delta V_{i+1}^k - \frac{\partial \rho}{\partial V}|_{V_i^k}\ \Delta V_i^k = s_i\ V_{i-1}^k - d_i\ V_i^k\ +\ s_{i+1}\ V_{i+1}^k + \rho(V_i^k) \tag{3.18}$$

Equation 3.18 is what Matlab will solve. To make it work, however, it needs to be expressed in matrix form. Everything on the right-hand side of the equal sign is going to be fitted inside the variable R_i^k. The diagonal term of the matrix, *diag*, will correspond to everything multiplying ΔV_i^k, which are d_i and the derivative of ρ with respect to the electrostatic potential V_i^k. ρ contains the dopant density concentration as well as the carrier concentration in each layer, the dependence of n and p with $V(x)$ have been shown in the previous section. Taking all of this into consideration, *diag* will look like the following

$$diag = d_i - \frac{1}{k_b T}\ (p(V_i^k)\ \frac{exp(-(E_{v_i}^k - E_{f_{h\,i}}^k - V_i^k)/k_b T)}{1 + exp(-(E_{v_i}^k - E_{f_{h\,i}}^k - V_i^k)/k_b T)} + n(V_i^k)\ \frac{exp((E_{c_i}^k - E_{f_{e\,i}}^k - V_i^k)/k_b T)}{1 + exp((E_{c_i}^k - E_{f_{e\,i}}^k - V_i^k)/k_b T)}) \tag{3.19}$$

For $0 < x \leq t_{CL}\ and\ x > t_{CL} + t_{BL}$. While for $t_{CL} < x \leq t_{CL} + t_{BL}$, *diag* will be

$$diag = d_i - \frac{1}{k_b T}\ (p(V_i^k)\ \frac{exp(-(E_{v_i}^k - E_{f_{h\,i}}^k - V_i^k)/k_b T)}{1 + exp(-(E_{v_i}^k - E_{f_{h\,i}}^k - V_i^k)/k_b T)}\ +\ n(V_i^k)) \tag{3.20}$$

Matrix **M** contains the left-hand side of equation 3.18 and is a tridiagonal matrix as seen below. To reduce computation time and memory consumption, **M** is described in the sparse format of Matlab. This way, only the terms in the diagonals shown below will be saved in the script, helping to speed up the calculations.

$$\begin{bmatrix} diag_1^k & -s_2 & & & & \\ -s_1 & diag_2^k & -s_3 & & & \\ & & & & & \\ & & & -s_{N-2} & diag_{N-1}^k & -s_N \\ & & & & -s_{N-1} & diag_N^k \end{bmatrix} \tag{3.21}$$

The system of equations that needs to be solved will follow the expression below:

$$\mathbf{M}\ \cdot\ \Delta\ \mathbf{V} = \mathbf{R} \tag{3.22}$$

Matlab possesses an intrinsic function to solve this kind of problems. The eigenvalues will be stored in matrix Δ **V** and using Equation 2.58, it is possible to obtain the updated values for

the electrostatic potential. The process will be repeated until convergence is reached according to Equation 2.60.

Once the first eigenvalue problem has been solved, a similar process is followed to obtain a new function for the hole quasi-Fermi level, E_{f_h}, all across the heterostructure. To comprehend the strategy, it is useful to recall the continuity equations expressions from chapter 2 (2.22) as well as the equations for the hole and electrons current density (2.20). If one assumes steady-state, so it is to say that the carrier concentration does not change with time, the two sets of equations can be bundled together to obtain an expression as the following

$$\frac{\partial}{\partial x}\ [\mu_p(x)\ p(x)\ \frac{\partial E_{f_h}(x)}{\partial x}] - G_p R_p(x,t) = 0 \tag{3.23}$$

The flow of electrons in the heterostructure is highly suppressed with the nBn architecture due to the presence of the electron barrier between the absorption and contact layers. Electrons injected from the source in the contact layer will not be able to travel to the absorber and will end up recombining, so their contribution to dark current is eliminated. Therefore, the variation of the electron quasi-Fermi level has been neglected. Only the changes in the hole quasi-Fermi due to the theoretical flow of holes will be considered. Also, the script assumes steady state conditions so the temporal dependence is neglected.

The approach taken here is similar to what has been described for V. Equation 3.23 is defined at every point in a one-dimensional grid across the structure, and the correction factor is calculated at every iteration step solving the eigenvalue problem in matrix form. The finite difference method has once again been used to numerically calculate the derivatives. The starting point is to dissect Equation 3.23 in its different components for a point i in the grid,

$$\frac{\partial \mu_{p_i}}{\partial x}|_{\mu_{p_i}}\ p_i\ \frac{\partial E_{f_{hi}}}{\partial x}|_{E f_{hi}}\ +\ \frac{\partial p_i}{\partial x}|_{p_i}\ \mu_{p_i}\ \frac{\partial E_{f_{hi}}}{\partial x}|_{E f_{hi}}\ +\ \mu_{p_i}\ p_i\ \frac{\partial^2 E_{f_{hi}}}{\partial x^2}|_{E f_{hi}} - G_{p_i} R_{p_i} = 0 \tag{3.24}$$

μ_{p_i} is the hole mobility in each layer and p_i is the hole concentration as a function of both V and x. $G_{p_i} R_{p_i}$ is the net generation-recombination rate, as explained in chapter 2 the leading recombination mechanisms are Auger 1 and radiative recombination. The explicit dependence on the carrier concentrations for the two mechanisms are also depicted in Equations 2.46 and 2.51.

To proceed, the solver will mimic what has been explained to find the roots of the electrostatic potential. That is to say, finding a suitable expression for Taylor's expansion series of equation 3.23. Recall Equation 2.59,

$$f_i(x^k)\ =\ -\ \sum_{j=1}^{N} \frac{\partial f_i}{\partial x_j}|_{x^k}\ \Delta x_j^k \tag{3.25}$$

Equation 3.24 corresponds to the left side of the equal sign in the expression above. Now, the challenge is to find the Taylor's series expression of the function. If one only takes the first order terms of the Taylor expansion,

$$\sum_{j=1}^{N} \frac{\partial f_i}{\partial x_j}|_{x^k}\ \Delta x_j^k = s_{E_{fh_i}} \Delta E_{fh_{i-1}}^k\ +\ s_{E_{fh_{i+1}}} \Delta E_{fh_{i+1}}^k\ +\ diag_{E_{fh_i}} \Delta E_{fh_i}^k \tag{3.26}$$

Where,

$$s_{E_{fh_i}} = \frac{\mu_{p_i}\ p_i}{\Delta_i^2}\ -\ \frac{1}{\Delta_i}(\frac{\partial \mu_{p_i}}{\partial x}|_{\mu_{p_i}}\ +\ \frac{\partial p_i}{\partial x}|_{p_i}\ \mu_{p_i}) \tag{3.27}$$

$$diag_{E_{fh_i}} = \frac{1}{\Delta_i}\frac{\partial \mu_{p_i}}{\partial x}|_{\mu_{p_i}}\ +\ \frac{\partial p_i}{\partial x}|_{p_i}\ \mu_{p_i}\ -\ \frac{2\mu_{p_i}\ p_i}{\Delta_i^2}\ +\ \frac{\partial G_{p_i} R_{p_i}}{\partial E_{fh}}|^k_{E_{fh_i}} \tag{3.28}$$

$$s_{E_{fh_{i+1}}} = \frac{\mu_{p_i}\ p_i}{\Delta_i^2} \tag{3.29}$$

Taking Equation 3.24 and Equation 3.26 together, one can construct the matrix system and solve the eigenvalue problem for the hole quasi-Fermi level, E_{f_h}. Similar to how it was proceeded to obtain the electrostatic potential, Matlab is going to solve

$$M_{E_{f_h}}\ \cdot\ \Delta E_{f_h} = R_{E_{f_h}} \tag{3.30}$$

Where, $R_{E_{f_h}}$ is a N-dimensional vector corresponding to the expression of Equation 3.24 at every point of the grid, and, $M_{E_{f_h}}$ is a tridiagonal matrix with the coefficients shown in Equation 3.26. A schematic of such a matrix can be seen below,

$$\begin{bmatrix} diag^k_{E_{fh_1}} & -s_{E_{fh_2}} & & & & \\ -s_{E_{fh_1}} & diag^k_{E_{fh_2}} & -s_{E_{fh_3}} & & & \\ & & & & & \\ & & & -s_{E_{fh_{N-2}}} & diag^k_{E_{fh_{N-1}}} & -s_{E_{fh_N}} \\ & & & & -s_{E_{fh_{N-1}}} & diag^k_{E_{fh_N}} \end{bmatrix} \tag{3.31}$$

3.4 Final Parameters and J_{dark} calculation

After the solution has converged, the updated values for V and E_{f_h} are introduced back into the carrier concentration equations and the band structure is computed. Some parameters of interest such as the electric field distribution, the charge density across the heterostructure are also calculated.

The position of the energy bands is calculated taking the distribution of the electrostatic potential after the solver has converged. Then, the values of V are subtracted to the original bulk band profile energy. Therefore, E_c and E_v are calculated as shown by the equation below.

$$E_c(x) = E_c^{bulk}(x) - V(x) \tag{3.32}$$

$$E_v(x) = E_v^{bulk}(x) - V(x) \tag{3.33}$$

Once the band structure of the device is obtained, it is possible to define the energy barrier that holes will encounter in their path from the absober to the contact layer. This energy is calculated taking the minimum of energy in the valence band and subtracting it from the valence band energy at the far edge of the absorber region, $E_{barrier} = -(E_{v_m in} - E_{bulk})$. It is considered that a carrier can traverse unimpeded the valence band barrier when its potential energy is higher than a certain threshold [56], defined as

$$E_{hole} \geq E_{barrier} - 3k_bT \tag{3.34}$$

With this information and using Equation 2.54 introduced in *Dark Current* section of Chapter 2 one can calculate the dark current density given a set of initial conditions for a nBn photodetector with a InAsSb absorption layer.

$$J_{dark} = q\frac{n_i^2}{N_D}\frac{L_{Diff}}{\tau}\tanh(\frac{W_{AL}}{L_{Diff}})exp(\frac{E_{hole}}{k_bT}) \tag{3.35}$$

Figure 3.2 presents an illustrative flow chart of the Poisson-continuity solver in the next page.

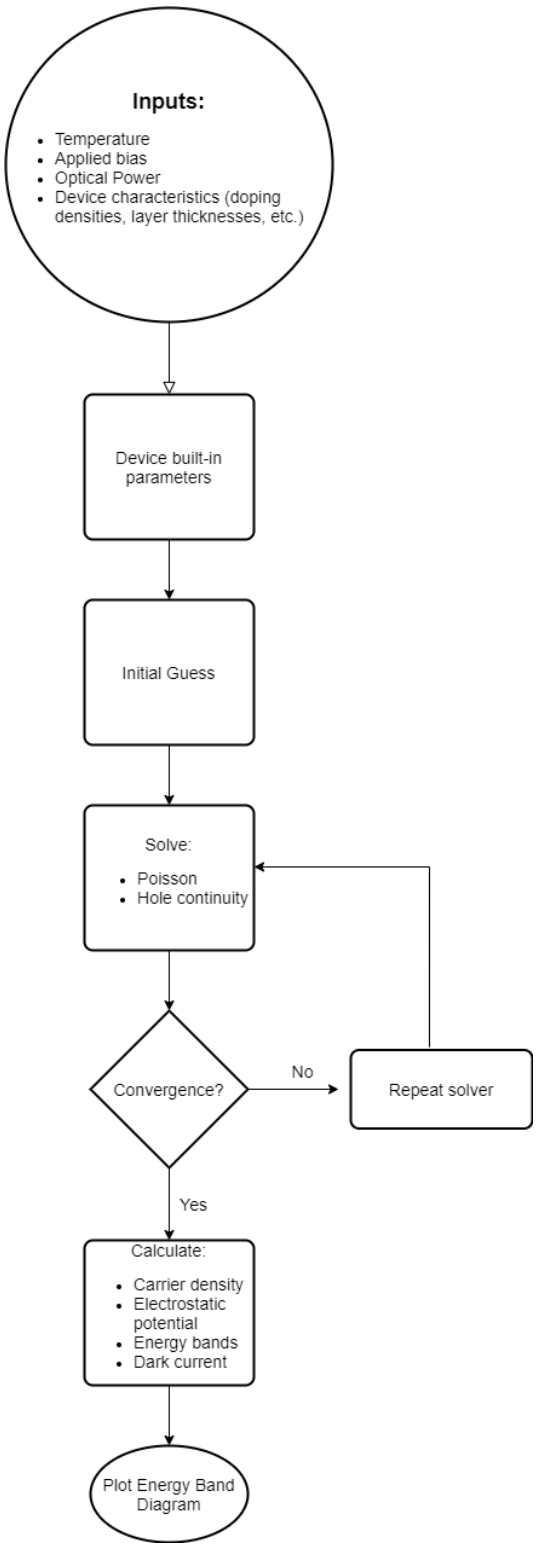

Figure 3.2: Flow chart of the Poisson-continuity solver.

4. Results and Discussion

In this chapter, the results of simulations carried by the Poisson-continuity solver will be shown. This includes the key parameters of the chosen material system for the detector. In in addition to that, representative figures that give an idea of the suitability of the designed device are compared with values extracted from state-of-the-art research.

4.1 Material Parameters

4.1.1 InAsSb Band Gap Energy

When designing a photodetector, the primary parameter one should take into account is the band gap energy of the absorption layer material. The band gap energy is going to define the target spectral region at which the device will work since it is going to limit the electron-hole pair optical generation processes.

Recalling from basic quantum theory and the photoelectric effect, to effectively convert the incoming radiation into electric current, the energy of the photons needs to match or exceed the semiconductor's band gap energy. That is to say, the energy of the irradiated photon is enough to promote an electron in the valence band into a conduction band energy state, generating an EHP in the process.

In the section about the *nBn Photodetector* in Chapter 2, the equation describing the band gap energy evolution of InAsSb as a function of the molar composition and the temperature was introduced. The expression takes the Varshini effect into account, and how the band gap will shrink down with the temperature of operation. Figure 4.1 shows the variation of InAsSb band gap energy as a function of temperature from 0 K to 300 K as described by Equation 2.28 [45].

As depicted in Figure 4.1, the band gap of the absorption layer material decreases with temperature. In this work, the aim is to focus on High Operating Temperatures conditions which include from 150 K to 300 K. In this temperature range, the band gap of InAsSb varies between 0.32 eV and 0.29 eV. That range of energies corresponds to wavelengths from 3.87 μm to 4.27 μm.

The band gap in the absorber will be greatly influenced by the growth conditions of that layer. Strain effects may distort the band structure of InAsSb, shifting the target spectral range of the absorption layer. To prevent this from happening, the absorber was grown on top of lattice-matched GaSb.

4.1.2 InAsSb intrinsic carrier concentration

n_i, also known as the intrinsic carrier concentration, is closely related to the expected performance of the detector. In fact, the dark current will be limited by the number of minority carriers available in the absorption layer, which is linked to the intrinsic carrier concentration of that same layer.

As shown in Equation 2.38, n_i depends on the molar fraction of Antimonide, x_{Sb}, the temperature, T and the band gap of InAsSb E_g. This relation, extracted from [49], explicitly shows a dependence of $n_i \sim exp(-E_g/2)$. Figure 4.2 displays the variation of the intrinsic carrier concentration with temperature at HOT conditions.

Figure 4.2 appears to be useful to have an idea of how the dark current evolves with temperature. At the same biasing and illumination conditions, the expected signal from the detector should be smaller at lower temperatures as there is fewer available holes in the absorption layer within an energy range capable to surmount the potential barrier.

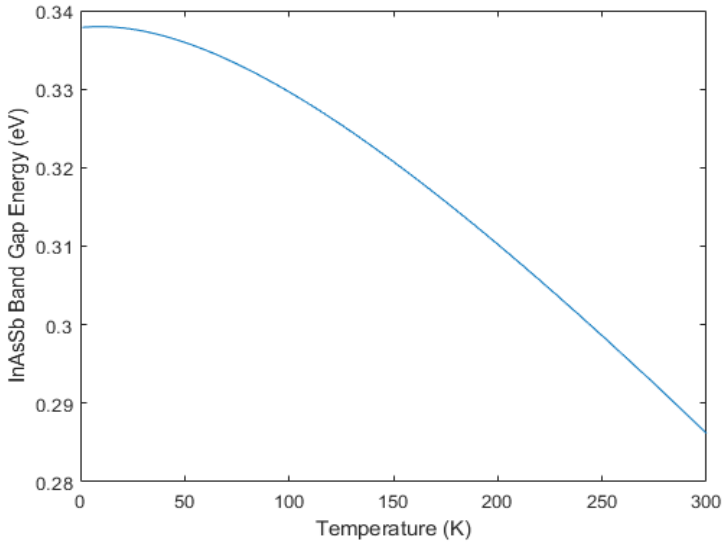

Figure 4.1: Evolution of InAsSb band gap with increasing temperature at molar fraction $x_{Sb} = 0.09$.

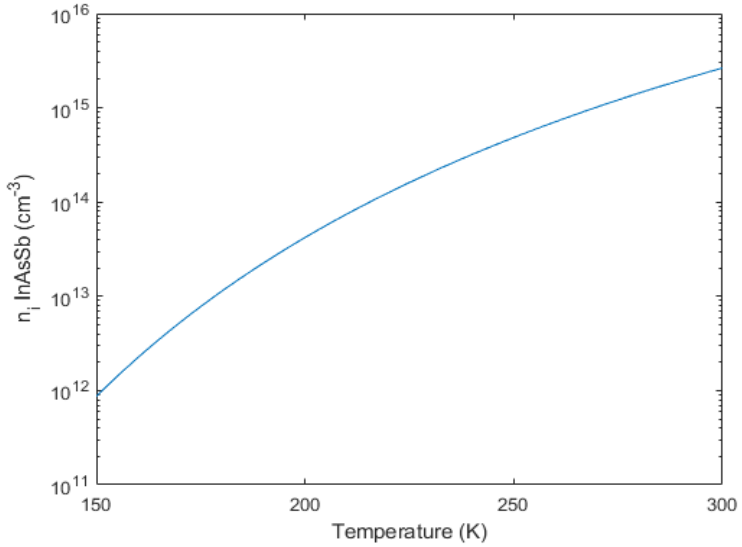

Figure 4.2: Evolution of InAsSb intrinsic carrier concentration with increasing temperature, in the range between 150 K to 300 K, at molar fraction $x_{Sb} = 0.09$.

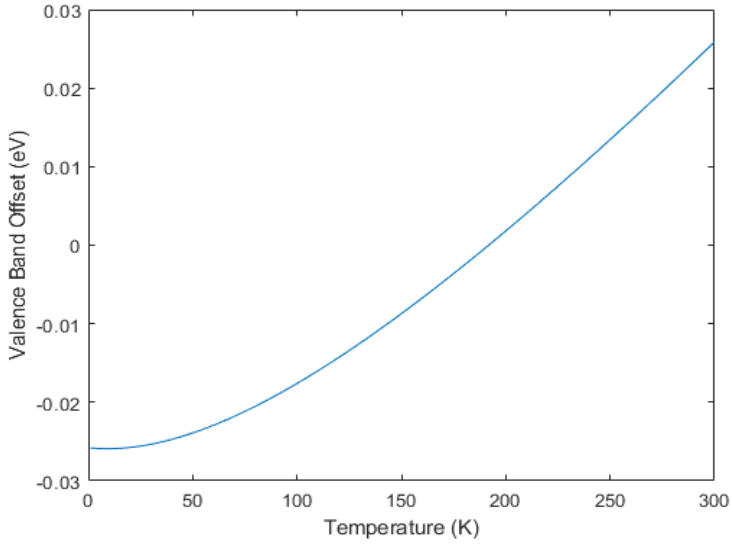

Figure 4.3: Evolution of the VBO at the InAsSb-AlInAsSb junction with increasing temperature at molar fraction $x_{Sb} = 0.09$.

4.1.3 Valence Band Offset

As explained earlier in this work, the alignment between the materials is expected to be *typeI* at room temperature. However, since the band gap of InAsSb is a function of temperature, the valence band offset that appears at the junctions will also change depending on the temperature of operation. It has been assumed that InAsSb's band gap shrinking or expanding with T is only translated into visible changes in VBO.

VBO is a critical parameter when the dark current is being studied as it represents an intrinsic energy barrier for the flow of photogenerated holes from the absorption layer to the contact layer. The choice of materials for the photodetector has taken into account that factor, InAsSb and AlInAsSb have a minimal VBO at room temperature - $VBO \sim 25meV$ -. At low bias, the potential barrier energy is many times larger than the VBO and its weight in the carrier transport can be dismissed. However, when the external voltage is high and the energy of the barrier has been reduced, VBO appears like a built-in blocking mechanism since its energy contribution is similar to the thermal energy, $VBO_{300K} \sim k_b T$.

As seen in Figure 4.3, the VBO at the InAsSb-AlInAsSb junction decreases with decreasing temperature as an effect of the expansion of the InAsSb band gap. At very low temperatures, below 190 K, the alignment between the semiconductor bands is no longer *typeI*, but it evolves to a *typeII* band alignment.

One can also note that there is going to be a temperature range at which VBO will be minimized close to 0 eV. According to the calculations, at 192 K there is no valence band offset at the heterojunction and the carrier transport depends entirely on the electrostatic potential barrier response to the external bias. With this stack of semiconductors, the carrier collection performance of the heterostructure is going to be optimized close to this temperature.

4.1.4 InAsSb Absorption coefficient

The absorption coefficient of InAsSb was modelled following Equation 2.41. There, the strong dependence of the band gap and the material and the absorption coefficient, α, were shown. When the incoming radiation is smaller in energy than the material's band gap, the absorption

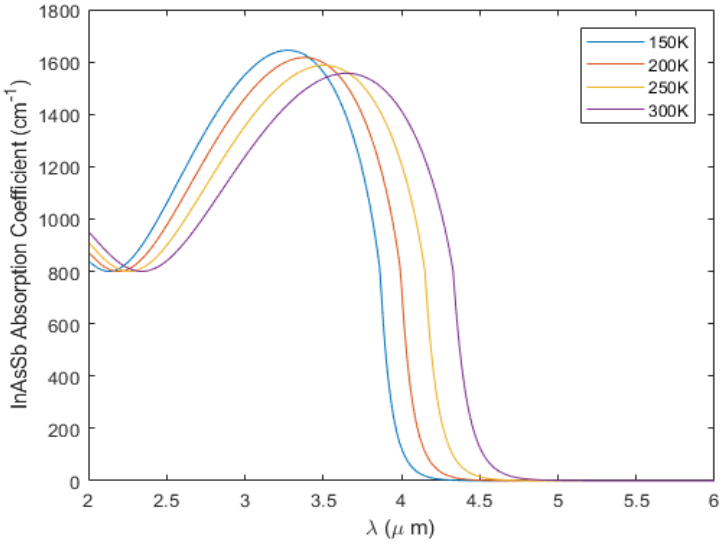

Figure 4.4: Evolution of InAsSb absorption coefficient, α, at different temperatures as a function of the incoming radiation wavelength.

coefficient follows the Urbach tail model. As the band gap of InAsSb varies with temperature, a shift in the energy threshold of absorption is also expected. Figure 4.4 shows the evolution of the absorption coefficient of the absorber as a function of the incoming radiation wavelength at different temperatures.

As displayed in Figure 4.4, the absorption coefficient peaks between 3-4 μm for all the range of simulated temperatures with α values around 1600 cm^{-1}. The maximum value of the absorption coefficient tends to decrease with increasing temperature, this behaviour seems to respond to the K parameter in Equation 2.41 that takes into account the band gap energy as a multiplying factor. Since E_g in InAsSb decreases with T, the value of K should also be smaller at higher temperatures.

4.2 Device Characteristics

The following section covers the analysis and discussion of certain device parameters. As a reference, the reports from Reine et al. [29, 30, 31] were followed and some of the data contained in the cited articles were included for comparison. Other figures to evaluate the performance of the proposed detector can be found in this section as well. Dark current characteristics have been simulated to assess how their behaviour compares with a typical diffusion-limited device and to understand the biasing boundaries for an optimized functioning of the device.

4.2.1 V_{max} and Potential Barrier height at $V_{app} = 0V$

As described by Reine et al. [29], if one solves the Poisson equation in the barrier layer, an intuitive expression for the maximum voltage this layer will absorb can be obtained. This parameter V_{max} is indicative of the operational conditions one can impose to detector. V_{max} can be calculated using the equation below,

$$V_{max} = \frac{qN_d(\frac{W_{AL}}{2})^2}{2\varepsilon_{BL}} \tag{4.1}$$

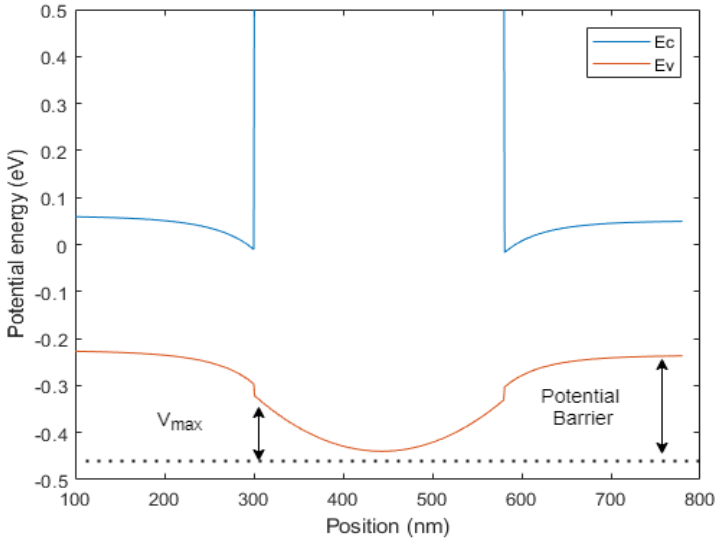

Figure 4.5: Visualization of V_{max} and the Potential Barrier height at the InAsSb-AlInAsSb double heterojunction for $V_{app} = 0$ V and $N_d = 1x10^{16}cm^{-3}$ at room temperature.

This expression shows a linear relationship between the dopant density in the barrier layer and the potential drop in it. V_{max} should not be confused with the potential barrier height, the former is only dependent on the characteristics of the wide band gap layer, the latter includes the VBO and the band bending effects from the electron accumulation near the junctions. Figure 4.5 illustrates these two parameters within the heterostructure model.

The values of both V_{max} and the total potential barrier height at five different barrier layer dopant densities ($6x10^{15}$, $8x10^{16}$, $1x10^{16}$, $1.5x10^{16}$, $2x10^{16}$) have been calculated using the Poisson-continuity solver. The results have been compared to the above expression derived by Reine [29].

Figure 4.6 shows the curves of $V_{max}(N_d)$ at two different temperatures, 200 K and 300 K, given by the Poisson-continuity solver. The applied bias in the simulations is 0 V. Figure 4.6 is representative of the good agreement between Equation 4.1 and the results from the script, the relative error has been found to oscillate between 3-7 %. This indicates that the Poisson equation is properly solved by the algorithm within the barrier layer.

Figure 4.7, on the other hand, shows the potential barrier height dependence with the wide band gap dopant density. In Reine et al. papers [29, 30, 31], the total potential valence band barrier was $1.179V_{max}(eV)$. According to results extracted from the solver, this linear relation between N_{dop} and the valence band barrier height still holds, but the relative contribution of the wide band gap semiconductor is lesser. It can be seen that for the same N_d, the potential barrier height is larger in the simulated device than the potential barrier energy predicted by the equation in [29]. In Reine's article, the absorption and contact layer where made of InAs, whereas, in this work the semiconductor of use is InAsSb, thus, is it plausible to see how the different choice of material can lead to changes in VBO and n_i which will account for the deviation between the curves in Figure 4.7.

It is important to mention how the potential barrier height seems to crossover at around $1.6x10^{16}cm^{-3}$ for the different temperatures. At low barrier layer dopant densities, the height (in eV) of the valence band barrier is larger at higher temperatures, but as the dopant density increases, lower operational temperatures appear to show a bigger potential barrier. This is because of the effect the temperature has on the electrostatic properties of the junction, especially when it comes to determine the built-in voltages.

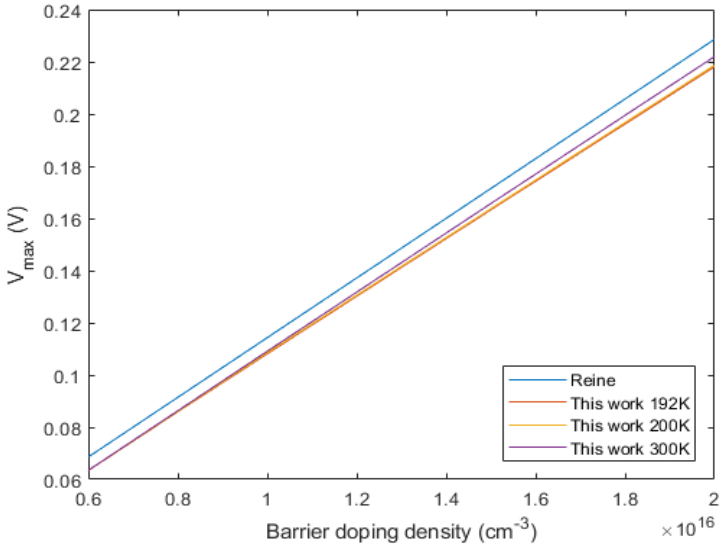

Figure 4.6: V_{max} as a function of the barrier layer dopant density for two different temperatures at $V_{app} = 0$ V. In blue, the expression derived by Reine is used as a comparison.

$$qV_b = \Delta E_c - k_b T \; ln(\frac{N_C N_d}{N_D N_c}) \tag{4.2}$$

Recalling Equation 2.5 -also shown above-, the built-in potential, V_{bi}, depends on the conduction band density of states, the dopant density in the materials involved and the difference between the conduction band edge energies. The electron density of states in the conduction band, N_C and N_c, have a strong relationship with temperature. For the same N_D values, the influence of the $ln(\frac{N_C N_d}{N_D N_c})$ will decrease as the temperature decreases and $V_{b_{1,2}} \sim \Delta E_c$. This means that at high dopant densities in the barrier layer, the electrostatic potential is larger at low operational temperatures. Intuitively, that makes sense since a higher dopant density will in turn become a large number of positively ionized donors per unit volume in the barrier layer. The holes diffusing towards the barrier from the absorber layer will "feel" a larger electrostatic repulsive force, as the charge density is bigger. In addition to that, the thermal energy represented in the $k_b T$ term will also be smaller, and therefore, the energy holes can acquire from the environment to surpass the barrier is also reduced.

Figure 4.7 shows the results of the potential barrier height at three different temperatures: 300 K, 200 K and 192 K. According to Figure 4.3, $VBO_{300K} > VBO_{200K} > VBO_{192K}$. Then, one would think this situation should lead to $E_{Barrier}(300K) > E_{Barrier}(200K) > E_{Barrier}(192K)$, but that is only true for small to moderate barrier layer dopant densities, this effect is shown in Figure 4.7. As mentioned before, the explanation may come from the fact that at higher T, the logarithmic term in Equation 4.2 increases its influence and reduces V_{bi}.

The major takeover from Figures 4.6, 4.7 is that the linear relation between N_d and both V_{max} and the potential barrier height in the valence band holds, indicating the effectiveness of the Poisson-continuity solver.

4.2.2 Band structure characteristics

The main goal of the Poisson-continuity solver is to display comprehensible and reliable information about the band structure of the simulated photodetector. Many of the characteristics that will

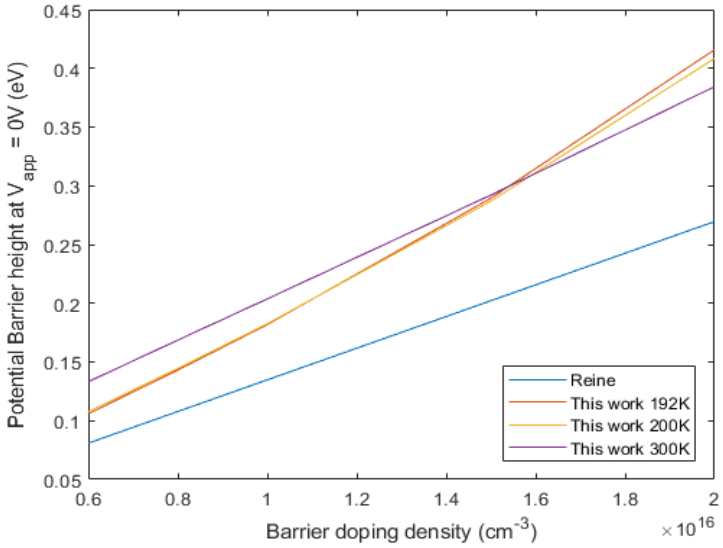

Figure 4.7: Potential barrier height as a function of the barrier layer dopant density for two different temperatures at $V_{app} = 0$ V. In blue, the expression derived by Reine is used as a comparison.

influence the performance of the detector are related to the band structure. There, one can find how the carriers distribute or the variations of the quasi-Fermi levels, among many other key parameters to evaluate the heterostructure.

Temperature, applied bias, dopant densities of the constituent layers, or the optical power density will have an effect on the shape of the band structure. The solver's work is to take into account all those parameters to compute a reliable diagram which sketches the behaviour of the semiconductors in the heterojunction according to the operational conditions. The result can be seen in Figure 4.8, where the band structure of the nBn photodetector is displayed.

Looking at Figure 4.8, one can quickly see that there is an important band bending phenomena at the edges of the barrier layer. That is indicative of the accumulation of electrons near the space charge region which extends over the barrier layer width. AlInAsSb is depleted from mobile charges which have migrated to the adjacent contact and absorption layers.

The reverse applied bias over the heterojunction will have an effect on the accumulation regions and the barrier. Since AlInAsSb is the constituent layer with the larger dopant density, it has been assumed that the potential drop is going to occur there. In addition to that, the absorber layer will be positively biased with respect to the InAsSb contact layer. Thus, when $V_{app} < 0$, the charge density enclosed in the accumulation region at the barrier-absorber junction is going to decrease while the charge density in the accumulation region at the contact-barrier junction will increase. If the applied bias is pushed high enough, all the electrons in the absorber accumulation region will be mobilized away from that junction. Push V_{app} even higher and, in order to compensate for the increase of charge density at the contact-barrier junction, the absorber layer will start to be depleted from electrons.

This behaviour described above can clearly be seen in Figure 4.9 with V_{app} up to -0.6 V. The plot contains the information of the carrier density across the nBn photodetector. Negative carrier density means electrons occupy that region, while a positive carrier density is indicative of ionized donors or holes in that region. As the applied bias is more negative, the carrier density at the barrier-absorber junction edge shrinks down, while the accumulation increases at the other heterojunction. The carrier density in the barrier layer remains constant at $1x10^{16}cm^{-3}$ up to

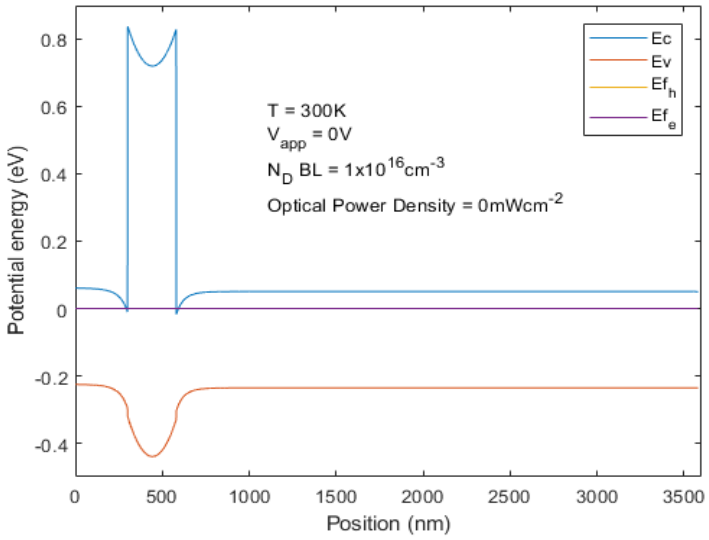

Figure 4.8: Band structure of the simulated nBn photodetector. The plot consists of the energy distribution of E_v, E_c and the quasi-Fermi levels E_{f_h}, E_{f_e}. E_{f_h} is superimposed to E_{f_e} as they share the same position. The operational conditions of the simulations are displayed in the plot.

$V_{app} = -0.6$ V. This indicates that the layer is depleted and the only charge contribution comes from the ionized donors. This behaviour stands up to $V_{app} = -0.6$ V when the flat-band condition is reached, and the charge density at the barrier-absorber edge is 0.

To understand what happens at higher applied biases, it is necessary to explain how the space charge region is formed within the barrier layer width. As a result of the electrostatics of the junction, two SCRs will appear where the AlInAsSb-InAsSb junctions are, one at each side of the barrier layer. The width of these SCR will depend on the doping characteristics of the contact, barrier and absorption layers as shown in the equation below. The parameters in capital letters refer to wide band gap semiconductor, meanwhile, the parameters in small case letters refer to the smaller band gap semiconductor.

$$W_{SCR} = \sqrt{\frac{2\varepsilon_N \varepsilon_n V_{bi} N_d}{qN_D(\varepsilon_N N_d \varepsilon_n N_D)}} \tag{4.3}$$

With the chosen dopant densities for each layer in this work, the SCR of both heterojunctions will overlap and therefore, the entire width of the barrier layer will be depleted of mobile carriers. As seen from the absorption region side, the applied bias is going to reduce the built-in voltage at the barrier-absorber heterojunction, and, consequently, the width of the resulting SCR. For high applied bias, the two space charge regions are not going to overlap anymore, leaving a region within the barrier layer where holes can be allocated. The newly appeared hole concentration in the AlInAsSb layer can be seen in Figure 4.9 at $V_{app} = -0.7$ V. To compensate for the depletion of the absorber and the presence of holes in the barrier layer at higher applied voltages, the charge density due to accumulation in the contact layer increases.

A schematic of the band structure at 300 K and under an applied bias equal to -0.7 V is shown in Figure 4.10. The electron quasi-Fermi levels in the barrier and absorption layer are assumed to be in equilibrium with each other [28]. The hole quasi-Fermi level across the heterostructure has been solved by the algorithm. Interestingly, at this V_{app} the hole quasi-Fermi level is very close to the valence band edge within the barrier layer, this results in the appearance of a surplus of

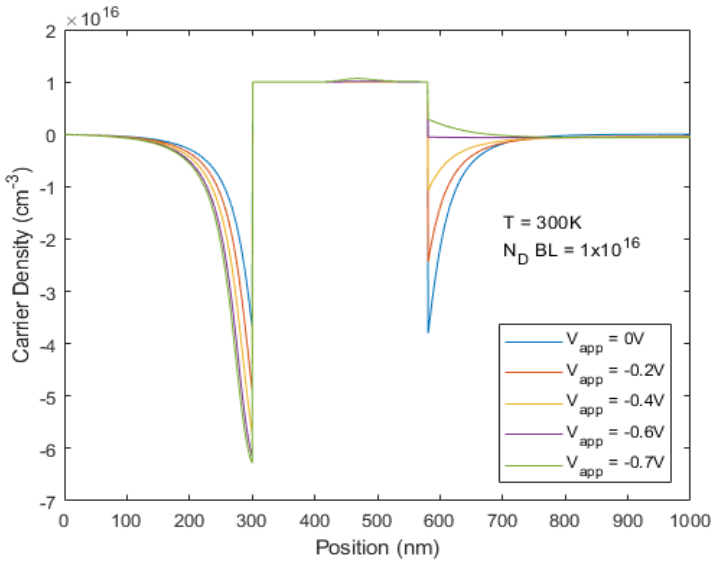

Figure 4.9: Carrier density across the heterostructure as a function of different voltages at 300 K. Charge density can be related to charge density just multiplying by the elemental unit of charge, $q = 1.6x10^{-19}C$. A negative value in the carrier density means electrons are allocated in that region, while a positive value is indicative of the presence of holes and positively ionized donors.

positive charge carriers at V_{app} in the AlInAsSb region as shown in Figure 4.9.

The carrier density plots have also been studied as a function of temperature. Figure 4.11 shows the differences that arise depending on the working temperature. The most noticeable one is the shape of the accumulation region at the contact-barrier junction. At lower temperature, this area of accumulated electrons seems to spread over the contact while also having a lower absolute value. This can be understood from Equations 3.8 and 3.9 presented in Chapter 3.

$$p(x_i) \sim N_v(x_i) \frac{1}{1 + exp(-(E_v(x_i) - E_{f_h}(x_i) - qV(x_i))/k_bT)} \tag{4.4}$$

$$n(x_i) \sim N_c(x_i) \frac{1}{1 + exp((E_c(x_i) - E_{f_e}(x_i) - qV(x_i))/k_bT)} \tag{4.5}$$

At lower T, $N_c(x_i)$ is smaller, therefore the number of conduction band states to fill in with electrons is reduced and the maximum value of the charge density is lower. As it can be seen from Figure 4.11, the reduction of the accumulation region at the barrier-absorber interface is the same regardless of the temperature. Since the number of available states to incorporate new electrons on the other side is lower, in order to keep the charge balance, the accumulation region spreads over the contact layer and the effective "accumulated surface" is larger at lower T.

In Figure 4.12 the distribution of the electrostatic potential across the detector is shown. In that same plot, it is possible to appreciate that the electrostatic potential is more concentrated within the barrier layer width at 300 K than at 200 K. This is linked to Equation 4.5, a more spread $V(x_i)$ function favours a more spread $n(x_i)$ distribution which can explain what is shown in Figure 4.11. In Table 4.1 there are shown the potential drop at each of the layers. It is visible from the values displayed in Table 4.1 that the potential drop in the absorption layer barely changes with T, however, the potential drop in the contact layer is higher at 200 K. As the carrier concentration varies exponentially with V, a relative small shift in the electrostatic potential distribution turn into a visible modification of the carrier density as shown in Figure 4.11.

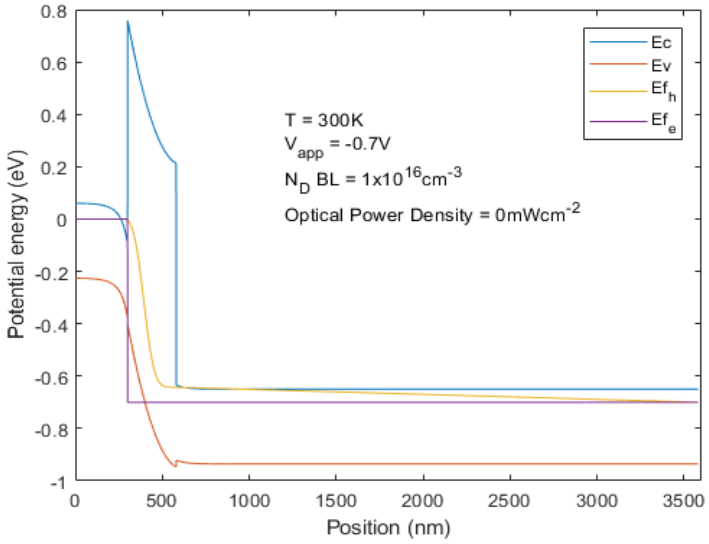

Figure 4.10: Band structure of the simulated nBn photodetector at $V_{app} = -0.7V$. The electron quasi-Fermi level of the barrier layer and the absorber is considered to be in equilibrium.

	200 K	300 K
V_{CL} (V)	0.1354	0.1137
V_{BL} (V)	0.2900	0.3106
V_{AL} (V)	-0.0254	-0.0243

Table 4.1: Electrostatic potential drop in each of the layers at 200 K and 300 K. It can be seen how the electrostatic potential is more concentrated in the barrier layer at higher T.

4.2.3 Electric Field

The electric field is an important factor when it comes to the analysis of the nBn photodetector, as it unveils some characteristics about the electrostatics. Moreover, it is also a key parameter in the carrier collection, as a strong electric field in the barrier layer could lead to a faster response time of the detector. However, it is important to remark that such a strong electric field should be contained within the width of the wide band gap semiconductor.

The magnitude of the electric field is going to be determined by the dopant density of the barrier layer and its width. A high electric field can lead to undesired phenomena such as band-to-band tunnelling. However, in the nBn detector, this is highly mitigated by the introduction of a large CBO.

As shown in Figure 4.13, the magnitude of the electric field in the absorber layer decreases as the applied bias becomes more negative. At $V_{app} = -0.6V$, the flat-band condition is reached and the electric field is nearly 0 $kVcm^{-2}$. If the applied voltage is even more negative and the absorption layer starts to be depleted, the electric field becomes negative. On the other hand, as the applied bias goes to more negative values, the electric field at the contact-barrier junction increases its magnitude. The results for the electric field plot are consistent with the Poisson equation and the band structure plots that were shown previously.

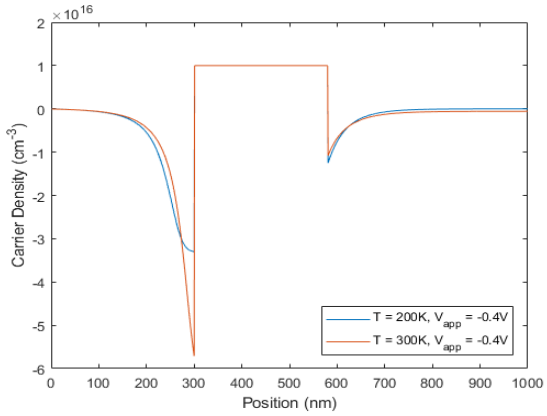

(a) Carrier density plots at $V_{app} = -0.4V$ at two different temperatures.

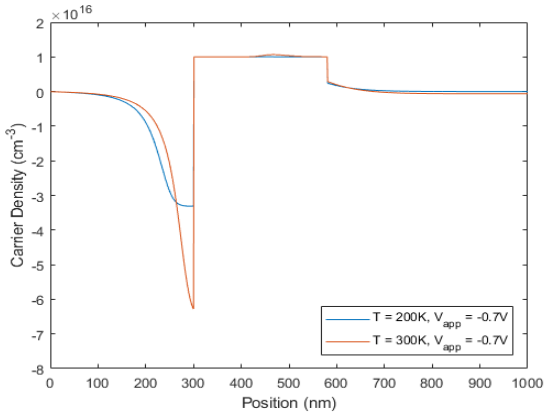

(b) Carrier density plots at $V_{app} = -0.7V$ at two different temperatures.

Figure 4.11: Carrier density plots as a function of temperature for two different applied biases.

4.2.4 Dark Current Density

Dark current density is the key parameter when evaluating the performance of the device. Dark current levels define the possibilities of the detector in terms of detectivity and responsivity. A better sensor is one that can successfully discern between the contribution coming from illumination and the contribution inherent to the device itself.

The current density has been calculated according to Equation 2.54. The potential barrier energy has an important effect as it regulates the flow of holes from the absorber to the contact layer. The temperature of operation will also limit the performance of the detector in this regard, as it will limit the number of available carriers, the diffusion length and carrier lifetime in the absorption layer.

The results from the simulated dark current density are shown in Figure 4.14. At very low temperatures, 150 - 200 K, the levels of J_{Dark} are comparable with the results published by Klem et al. in 2010 [73]. The material employed in the article was InAsSb as the absorber and AlAsSb as the barrier layer semiconductor. With a similar material system, Reine et al. [31] reported dark current levels around $6x10^{-7}A/cm^{-2}$ for an nBn detector at 200 K, which is a couple of orders of magnitude below the simulated results in this work. These results, however, are based on a back-to-back diode model to calculate the dark current density.

The dark current density follows the exponential curve predicted by Equation 2.54. At low bias, the potential barrier is too high to overcome, and the amount of charge carriers that flow from the absorber to the contact is small. The dark current increases exponentially until the effective barrier for holes is suppressed, then, the dark current reaches its saturation value.

Trying to investigate the role of the VBO in the dark current density, a simulation was run to visualize the current curve at 192 K, where the valence band offset is at its minimum. Figure 4.15 shows the evolution of J_{dark} as a function of V_{app} at such temperature. If one compares the two plots, it can be seen that the saturation bias, V_{sat}, increases when the temperature decreases. This fact relates to what has been previously mentioned: the role of VBO is secondary, and the main parameter controlling the device characteristics is the increase of V_{bi} at cooler T. Table 4.2 shows the results in Figure 4.14 and 4.15. The effect of a larger magnitude in VBO does not imply a higher V_{sat}.

V_{sat} is a very good indicator of the operational conditions of the device. Above V_{sat} the carrier collection can be done unimpeded. According to Reine et al. [29, 30, 31], the barrier affects both

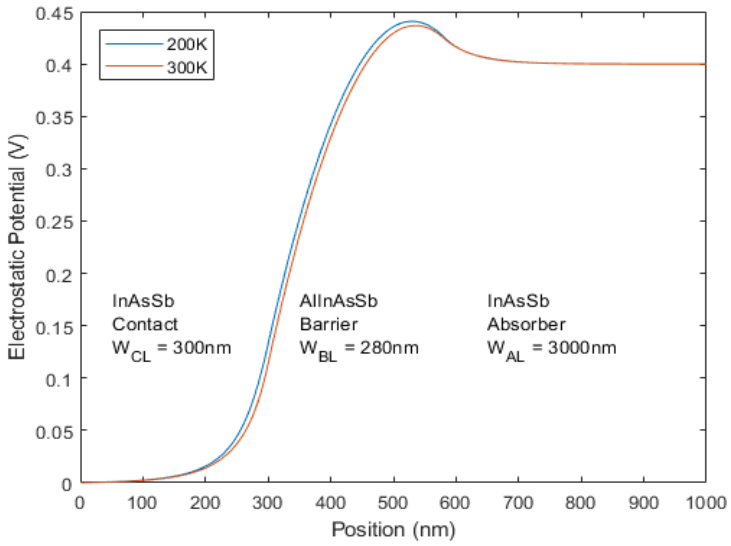

Figure 4.12: Electrostatic potential distribution across the heterojunction at different temperatures with an applied bias equal to -0.4 V. Not all the entire width of the absorber layer is shown in the plot.

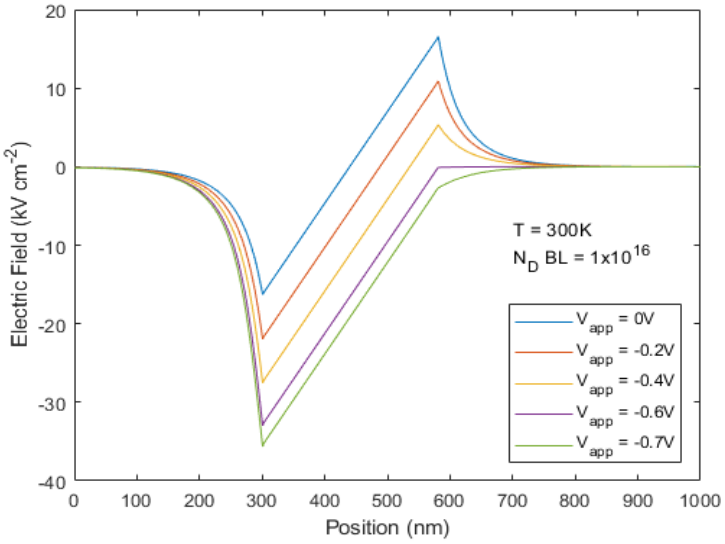

Figure 4.13: Electric field across the heterostructure as a function of the applied bias. Not all the entire width of the absorber layer is shown in the plot.

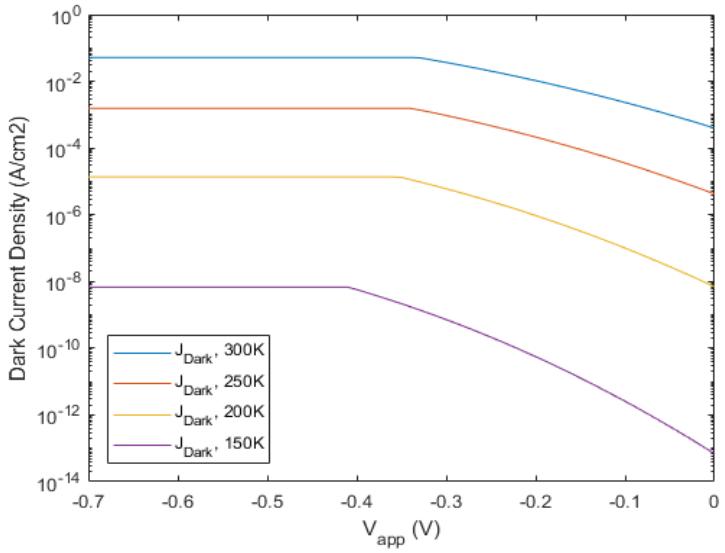

Figure 4.14: Dark current density as a function of the applied bias at four different operational temperatures. The curve follows an exponential relation at low voltages until the saturation voltage is reached. If one goes into larger bias the dark current plateaus at a constant value.

the dark current and the photocurrent likewise. Therefore, if the device is placed in the saturation regime, a higher fraction of the photogenerated holes would be detectable. However, the saturation regime has a window of applied bias before undesirable effects start to dominate. The main matter of concern is to push V_{app} so high that the absorber starts depleting from electrons and the SRH recombination mechanism become dominant. The voltage at which the absorption layer will start being depleted from electrons is V_{dep} and it is represented in Table 4.2. The table also includes the data for a possible device with an area of 10x10 μm^2. All the simulations were carried with the following parameters: barrier layer dopant density equal to $N_d = 1x10^{16}\ cm^{-3}$ and absorber layer width equal to 3 μm.

Temperature	I_{dark}^{sat} (A), 10 μm x 10 μm	J_{dark}^{sat} (A/cm^{-2})	V_{sat} (V)	V_{dep} (V)	VBO (eV)
150 K	$2.8x10^{-14}$	$2.8x10^{-8}$	-0.41	-0.72	-0.0087
192 K	$5.1x10^{-12}$	$5.1x10^{-6}$	-0.37	-0.65	0.0000
200 K	$8.2x10^{-11}$	$8.2x10^{-5}$	-0.36	-0.64	0.0018
250 K	$7.8x10^{-9}$	$7.8x10^{-3}$	-0.34	-0.61	0.0134
300 K	$2.0x10^{-8}$	$2.0x10^{-2}$	-0.34	-0.60	0.0259

Table 4.2: Dark current and dark current density levels at saturation, saturation voltage, depletion voltage and valence band offset for five different temperatures.

4.2.5 Dark Current Reduction Factor

Following Reine's studies of the nBn photodetector [29, 30, 31], the effect of the barrier layer doping was studied to see how it influences the dark current densities. There, Reine et al. proposed a parameter to compare the values of the dark current density at different barrier layer dopant densities. The lowest dopant density, in our case $N_d = 1x10^{-15}cm^{-3}$, is taken as a reference and the current density at this N_d is compared with the dark current density ($V_{app} = -0.05$ V) at other donor densities in the AlInAsSb layer. The ratios of dark currents are plotted against the potential barrier layer height at $V_{app} = 0$ V.

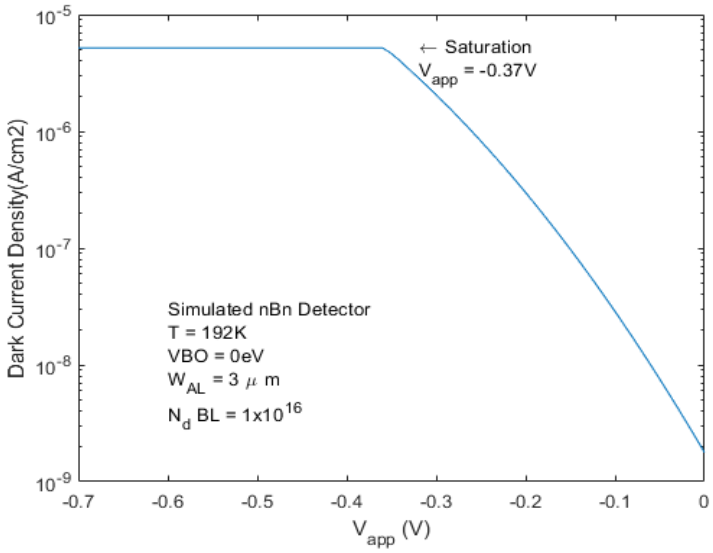

Figure 4.15: Dark current density as a function of the applied bias at 192 K, where VBO is at its minimum value. The curve follows an exponential relation at low voltages until the saturation voltage is reached, in this case, at $V_{app} = -0.37V$

The dark current reduction factor, DCRF, is fitted to a Fermi-Dirac-like equation with the potential barrier height at 0 V as the variable parameter. The equation of DCRF is shown below.

$$DCRF = \frac{1}{1 + A_T exp(EB_T/kbT)} \tag{4.6}$$

Where EB_T is the potential barrier height at $V_{app} = 0$ V for each temperature and A_T is a fitting parameter at different temperatures, $A_{200} = 9.0x10^{-3}$ and $A_{200} = 1.3x10^{-2}$.

BL Dopant Density (cm^{-3})	J_{dark} (300 K) (A/cm^{-2})	EB_{300K} (eV)	DCRF (300 K)
$1.0x10^{15}$	$1.36x10^{-5}$	0.0161	1.000
$2.0x10^{15}$	$1.36x10^{-5}$	0.0348	1.000
$4.0x10^{15}$	$1.36x10^{-5}$	0.0714	1.000
$6.0x10^{15}$	$2.01x10^{-6}$	0.1077	0.148
$8.0x10^{15}$	$2.47x10^{-7}$	0.1444	0.018
$1.0x10^{16}$	$2.78x10^{-8}$	0.1825	0.002
$1.5x10^{16}$	$6.73x10^{-11}$	0.2869	$4.950x10^{-6}$
$2.0x10^{16}$	$5.99x10^{-14}$	0.4084	$4.400x10^{-9}$

Table 4.3: Parameters for DCFR calculations at 200 K.

The parameters shown in Tables 4.3 and 4.4 have been plotted in Figure 4.16. The values of the dark current have been taken at V_{app} for each temperature. From the plot, it is possible to observe a good agreement between the DCRF functions and the simulated points marked as circles. Another aspect that is interesting to note from Figure 4.16, is that the reduction factor function does not start to follow the Maxwell-Boltzmann characteristic curve at $EB = 3k_bT$ but at higher potential barrier energies. In other words, the plot contradicts the intuitive approach that the onset of reduction will appear when the potential barrier height at $V_{app} = 0$ V is higher than $3k_bT$ in accordance to the dark current density description. A similar effect was found by Reine et al. [29, 30, 31] in their studies of the InAs nBn photodetector.

BL Dopant Density (cm^{-3})	J_{dark} (300 K) (A/cm^{-2})	EB_{300K} (eV)	DCRF (300 K)
$1.0x10^{15}$	$5.18x10^{-2}$	0.0426	1.000
$2.0x10^{15}$	$5.18x10^{-2}$	0.0607	1.000
$4.0x10^{15}$	$5.18x10^{-2}$	0.0972	1.000
$6.0x10^{15}$	$1.46x10^{-2}$	0.1332	0.282
$8.0x10^{15}$	$3.80x10^{-3}$	0.1686	0.073
$1.0x10^{16}$	$9.91x10^{-4}$	0.2037	0.019
$1.5x10^{16}$	$3.32x10^{-5}$	0.2921	$6.410x10^{-4}$
$2.0x10^{16}$	$9.45x10^{-7}$	0.3844	$1.820x10^{-5}$

Table 4.4: Parameters for DCFR calculations at 300 K.

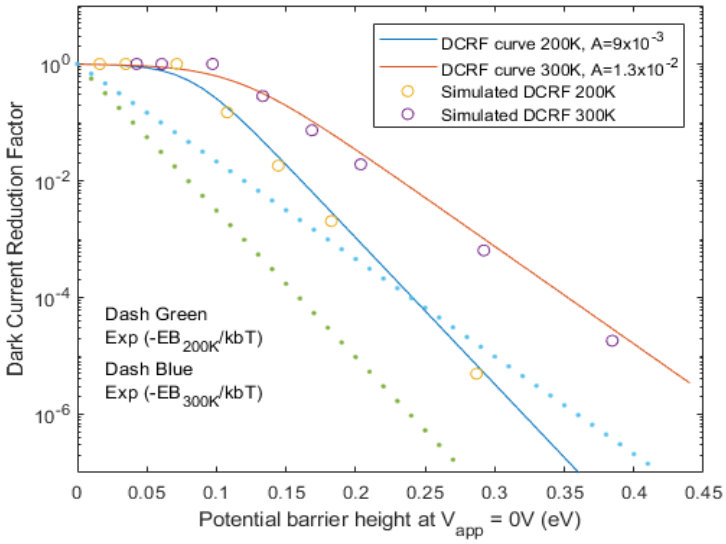

Figure 4.16: Solid lines correspond to the DCFR fitted according to Equation 4.6 at 200 K and 300 K. Yellow and purple circles are the values of the simulated DCFR from Tables 4.3 and 4.4. The dashed lines represent the Maxwell-Boltzmann-like function of the reduction of the dark current. J_{dark} for each N_d has been simulated at $V_{app} = -0.05$ V.

4.2.6 J_{dark} vs T

One common study to determine the characteristics of the photosensor's dark current response. If, as assumed, the dark current is only limited by diffusion processes in the absorption layer, it should follow the diffusion approximation $J_{diff} \sim T^3 exp(-E_a/k_bT)$, where the activation energy takes into account the potential barrier height.

$$E_a = E_{hole} = E_{g_{InAsSb}}(0K) + EB_T(T,V) - 3k_bT \tag{4.7}$$

J_{Dark} has been simulated as a function of the temperature at 3 different applied biases and a barrier layer dopant density $N_d = 1x10^{16}cm^{-3}$. The results have been plotted against $J_{diff} = BT^3 exp(-E_a/k_bT)$, where the fitting parameter $B = 1x10^3$. Figure 4.17 shows how the dark current density as a function of the temperature resembles the diffusion current density approximation for three sets of voltages. The functions have undergone a linear fitting procedure with Matlab to determine the activation energy for each curve. The results displayed in Table 4.5 show a very agreement between the simulated and approximation activation energies at all three different voltages.

V_{app} (V)	$E_a J_{dark}$ (eV)	$E_a J_{diff}$ (eV)
-0.1V	-0.52	-0.51
-0.3V	-0.45	-0.43
-0.5V	-0.41	-0.39

Table 4.5: Activation energies of the Arrhenius plot for the simulated, J_{dark}, and approximated, J_{diff} dark current densities at $V_{app} = -0.1, -0.3, -0.5V$.

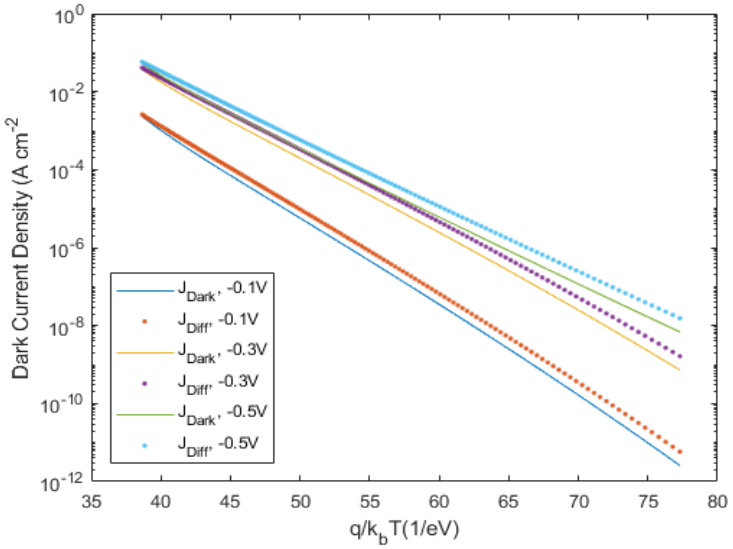

Figure 4.17: Simulated dark current density J_{Dark} at three different voltages in solid lines as a function of temperature. The fitted equation for diffusion current, J_{diff}, as a function of temperature is also shown, this time in dashed lines.

5. Future Work

In this work, a program to solve the Poisson Equation and continuity equations has been presented. The solver has proven to accurately describe the band structure of the heterostructure at certain conditions. It is a powerful tool for design optimization as it can provide meaningful results in relatively short computing times. However, it is not exempt from some adjustments to expand its utilities. Some of the issues may come from the description of the carrier densities at the bottom of the energy bands in the algorithm. In Chapter 3, it was shown the derivation to the expression used in this work. Despite being based on approximations, they displayed good results as presented in Chapter 4. However, at hard conditions: very low temperatures, high applied voltages or high barrier layer dopant densities, the functionality of the solver starts to diminish, casting some doubts on the accuracy of the displayed results when the device is pushed away from that "comfort zone". To overcome this, the driving parameters of the solver should be rewritten and more advanced physics in the detector need to be included.

The growth conditions of the different materials in the heterostructure have not been considered. However, strain effects can greatly disturb the band diagram of the materials involved in the detector. Additionally, quantum transport effects have not been studied in depth, but they can play an important role, especially in the accumulation regions and contacts. The more realistic the model is, the better its accuracy is going to be. One should keep in mind, however, that including more complicated physics into the solver will come at a cost in computation time that will distance the suitability of the program from its original purpose.

To further exploit the results obtained from the solver, one might introduce simulations based on the Monte-Carlo method which will give a new insight on the carrier transport within the device. This hybrid model could use the Poisson-continuity solver as the basis to depict the band structure of the detector while simulating the behaviour of the dark- and photocurrents with semi-classical transport equations.

The main parts of the solver provide some room for further investigations. Due to the way it has been conceived, one should be able to adapt new material systems with minor changes. For example, a possible future study could follow the work published by Reine et al. [29, 30, 31] and compare the performance of the $n-$type barrier layer UBIRD with that of a $p-$type barrier layer UBIRD. Changing the barrier layer material should also be an easy task. More complex structures with a greater number of layers could also be simulated, for example, to study the band structure of a complementary barrier infrared detector and its design possibilities.

The solver has provided for the static analysis of the detector, therefore, is not able to tell anything about its speed. Since holes are the working carrier type, it is expected to be slow, but the actual work can not quantify it. The inclusion of a time-evolving simulation will complement the work presented here and expand on the characteristics of the device. A dynamic analysis is needed to unveil other functionalities or flaws the detector may present. In that sense, the inclusion of Monte-Carlo-based simulations would as well be helpful.

6. Conclusions

This work aimed to present a convincing and reliable script for a heterostructure solver that could help as a design tool for future photodetectors. To realize such a task, an extensive literature review has been made to dive deep into the concepts that rule the semiconductor devices design. With this theoretical background, a proposal for a sensor architecture was made, and that became the basis for this thesis. From there, a computational tool has been built to expand on the study of the device's characteristics as well as the evolution of key parameters under different conditions.

The theory introduced in Chapter 2 should come as a basis for the reader to understand concepts used in later chapters while explaining the reasoning behind the choices made during the development of this work. Along with the theoretical introduction, the thesis includes a detailed description of the building blocks governing the Poisson-continuity solver in Chapter 3. The script's main purpose is to depict the band diagram of the heterostructure after solving Poisson and continuity equations. Chapter 4 presents the results obtained from various simulations of the active layers in the device at different conditions. From the information gathered in Chapter 4, one can see how the detector response to different ambient temperatures is, where the limits of its operational performance are and the evolution certain parameters will follow for a set of different conditions.

As mentioned in Chapter 5, there is still room for improvement in the description of certain parameters of the solver. In addition to that, the inclusion of new phenomena should also increase the reliability of the simulations. Nevertheless, the band structure results presented in Chapter 4 are in accordance with previous studies by Rogalski and Martyniuk [28]. The analysis made on the characteristics of the detector follows the work presented by Reine et al. [29, 30, 31]. The modifications suffered by the band structure at different applied bias resemble the effects noted by Reine in those articles for an InAs-AlAsSb nBn detector. The evolution of the electric field in the three studied regions of the simulated device was also comparable to the results shown there. To complete the analysis, a couple of parameters introduced by the same research group were studied and adapted to the simulations presented here, i.e. V_{max} and the Dark Current Reduction Factor (DCRF). These parameters were used to test the accuracy of the solver, and following the strategies explained in [29, 30, 31], they were analysed at different conditions. The similarities between the simulations in this work and the results presented by Reine et al. indicate the success of the solver to represent the UBIRD.

The key parameter to evaluate the performance of a photodetector is the dark current density levels it will achieve while in saturation. This analysis was also performed and the results of the simulations show that the dark current density for the proposed material system is comparable to the J_{dark} reported in other works for a similar stack of semiconductors [73]. In the model, the dark current was assumed to follow a diffusion-limited curve influenced by the potential barrier at the junction. The Arrhenius plot showed that the theoretical curve for a diffusion-limited behaviour and the evolution of the dark current at different temperatures were fairly similar.

The accuracy of the results shown in Chapter 4 has been checked by comparing the obtained data with publications with similar material system models. Therefore, it is plausible to conclude that the Poisson-continuity solver presented in this thesis can be used as a tool for the design of heterosturcture-based infrared detectors.

Bibliography

[1] A. Rogalski. History of infrared detectors. *Opto-Electronics Review*, 20(3):279–308, 2012. 1, 3

[2] M. Wolf, M. Ferrari, and V. Quaresma. Progress of near-infrared spectroscopy and topography for brain and muscle clinical applications. *Journal of Biomedical Optics*, 12(6), 2007. 2

[3] Y. Tamura et al. Lowest-ever 0.1419-db/km loss optical fiber. *Optical Society of America*, pages 1–3, 2017. 2

[4] NASA IPAC. Near, mid and far-infrared. 2

[5] American Technologies Network Corporation. How night vision works. 3

[6] W.D. Lawson, S. Nielson, E.H. Putley, and A.S. Young. Preparation and properties of HgTe and mixed crystals of HgTeCdTe. *Journal of Physics and Chemistry of Solids*, 9:325–329, 1959. 3

[7] M.A. Kinch, S.R. Borrello, and A. Simmons. 0.1 ev HgCdTe photoconductive detector performance. *Infrared Physics*, 17:127–135, 1977. 3

[8] A. Rogalski. InAs/GaSb type-ii superlattices versus HgCdTe ternary alloys: future prospect. *Electro-Optical and Infrared Systems: Technology and Applications*, 10433, 2017. 3, 23

[9] M. Kopytko P. Madejczyk A. Rogalski, P. Martyniuk and S. Krishna. InAsSb-based infrared photodetectors: Thirty years later on. *Optical Sensors*, 7047, 2020. 4, 19, 23, 24

[10] M. Lundstrom. Notes on heterostructure fundamentals. *School of Electrical and Computer Engineering and the NSF MRSEC for Technology-Enabling Heterostructures Purdue University*, 1995. 5

[11] R. L. Anderson. Germanium-gallium arsenide heterojunctions. *IBM Journal of Research and Development*, 4(3):283–287, 1960. 6

[12] F. Rana. Semiconductor optoelectronics, chapter 2, semiconductor heterostructures. *Cornell University*. 8

[13] B. G. Streetman and S. K. Banerjee. *Solid State Electronic Devices*. Pearson Education Inc., 2006. 11, 13

[14] R. Paschotta. Photoconductive detectors. *Encyclopedia of Laser Physics and Technology*, 2008. 13

[15] R. McIntyre. Multiplication noise in uniform avalanche diodes. *IEEE Transactions on Electron Devices*, ED-13(1):164–168, 1966. 15, 16

[16] B. Saleh and M. Teich. *Fundamentals of Photonics*. Wiley, 1994. 15

[17] C. N. Harrison, J. P. R. David, M. Hopkinson, and G. J. Rees. Temperature dependence of avalanche multiplication in submicron Al0.6Ga0.4As diodes. *Journal of Applied Physics*, 92(12):7684–7686, 2002. 15

[18] M.M. Hayat, B.E.A. Saleh, and M.C. Teich. Effect of dead space on gain and noise of double-carrier-multiplication avalanche photodiodes. *IEEE Transactions on Electron Devices*, 39(3):546–552, 1992. 16

[19] Erum Jamil, J. S. Cheong, J. David, and M. Hayat. On the analytical formulation of excess noise in avalanche photodiodes with dead space. *Optics express*, 24(19):21597–608, 2016. 16

[20] S. G. E. and W. C. M. Avalanche photodiodes. *Semiconductors and Semimetals*, 12:291–393, 1977. 16

[21] H. Ando, H. Kanbe, M. Ito, and T. Kaneda. Tunneling current in InGaAs and optimum design for InGaAs/InP avalanche photodiode. *Japanese Journal of Applied Physics*, 19(6):L277–L280, 1980. 16

[22] G. A. Sai-Halasz, R. Tsu, and L. Esaki. A new semiconductor superlattice. *Applied Physics Letters*, 30:651–653, 1977. 16

[23] T. Manyk, K. Michalczewski, K. Murawski, P. Martyniuk, and J. Rutkowski. InAs/InAsSb strain-balanced superlattices for longwave infrared detectors. *Sensors*, 19(8):1907, 2019. 16

[24] B. V. Olson, E. A. Shaner, J. K. Kim, J. F. Klem, and S. D. Hawkins et al. Time-resolved optical measurements of minority carrier recombination in a mid-wave infrared InAsSb alloy and InAs/InAsSb superlattice. *Applied Physics Letters*, 101(9):092109, 2012. 16, 23

[25] A. Haddadi, G. Chen, R. Chevallier, A. M. Hoang, and M. Razeghi. InAs/InAs1-xSbx type-ii superlattices for high performance long wavelength infrared detection. *Applied Physics Letters*, 112:241103, 2014. 17

[26] M. Kopytko, E. Gomółka, K. Michalczewski, P. Martyniuk, J. Rutkowski, and A. Rogalski. Investigation of surface leakage current in mwir HgCdTe and InAsSb barrier detectors. *Semiconductor Science and Technology*, 33(12):125010, 2018. 17, 23, 24, 25

[27] Ł. Kubiszyn, K. Michalczewski, D. Benyahia, J. Jureńczyk, D. Stepień, A. Kebłowski, J. Boguski, J. Rutkowski, and J. Piotrowski. High operating temperature lwir and vlwir InAs1xSbx optically immersed photodetectors grown on GaAs substrates. *Infrared Physics Technology*, 97:116–122, 2019. 17

[28] P. Martyniuk and A. Rogalski. Theoretical modeling of AlAsSb/InAsSb barrier detectors for higher-operation-temperature conditions. *Optical Engineering*, 53:017106, 2014. 17, 18, 19, 31, 46, 56

[29] Marion Reine, Benjamin Pinkie, Jonathan Schuster, and Enrico Bellotti. Numerical simulation of InAs *nBn* infrared detectors with *n-Type* barrier layers. *Infrared Technology and Applications XXXIX, Society of Photo-Optical Instrumentation Engineers (SPIE) Conference Series*, 8704:87041Y, 2013. 17, 18, 25, 42, 43, 49, 51, 52, 55, 56

[30] Marion Reine, Benjamin Pinkie, Jonathan Schuster, and Enrico Bellotti. New model for the ideal *nBn* infrared detector. *Infrared Technology and Applications XL, Society of Photo-Optical Instrumentation Engineers (SPIE) Conference Series*, 9070:907013, 2014. 17, 42, 43, 49, 51, 52, 55, 56

[31] Marion Reine, Benjamin Pinkie, Jonathan Schuster, and Enrico Bellotti. Numerical simulation and analytical modeling of InAs *nBn* infrared detectors with *n-Type* barrier layers. *Journal of Elec Materials*, 43:2915–2934, 2014. 17, 42, 43, 49, 51, 52, 55, 56

[32] J. H. Warner I. Vurgaftman J. C. Kim J. R. Meyer B. R. Bennett E. H. Aifer, J. G. Tischler and L. J. Whitman. W- structured type-ii superlattice based long and very-long wavelength infrared photodiodes. *Proc. SPIE, Quantum Sensing and Nanophotonic Devices II*, 5732:259–272, 2005. 18

[33] K. Kutluer T. Tansel R. Turan Y. Ergun O. Salihoglu, A. Muti and A. Aydinli. " "n" structure for type-ii superlattice photodetectors. *Applied Physics Letters*, 101:073505, 2012. 18

[34] P. Y. Delaunay B. M. Nguyen, D. Hoffman and M. Razeghi. Dark current suppression in type ii InAsGaSb superlattice long wavelength infrared photodiodes with m-structure barrier. *Applied Physics Letters*, 91:163511, 2007. 18

[35] D. Z.Y. Ting, A. Soibel, C. J. Hill, S. A. Keo, J. M. Mumolo, and J. Nguyen S. D. Gunapala. A high-performance long wavelength superlattice complementary barrier infrared detector. *Applied Physics Letters*, 95:023508, 2009. 18

[36] S. Maimon and G. W. Wicks. nbn detector, an infrared detector with reduced dark current and higher operating temperature. *Applied Physics Letters*, 89(15), 2006. 18, 23, 25

[37] Chengzhi Xie, Vincenzo Pusino, Ata Khalid, Adam P. Craig, Andrew Marshall, and David R. S. Cumming. Monolithically integrated InAsSb-based nbnbn heterostructure on GaAs for infrared detection. *IEEE Journal of Selected Topics in Quantum Electronics*, 24(6):1–6, 2018. 18

[38] D. Z.Y. Ting, A. Soibel, L. Höglund, and S. D. Gunapala. Theoretical aspects of minority carrier extraction in unipolar barrier infrared detectors. *Journal of Electronic Materials*, 44:3036–3043, 2015. 18

[39] A. Soibel, D. Z. Ting, Sir B. Rafol, A. M. Fisher, S. A. Keo, A. Khoshakhlagh, and S. D. Gunapala. Mid-wavelength infrared InAs/InAsSb nbn detectors and fpas with very low dark current density. *Applied Physics Letters*, 114(16):161103, 2019. 18

[40] D. R. Rhiger and E. P. Smith. Carrier transport in the valence band of nbn iii–v superlattice infrared detectors. *Journal of Electronic Materials*, 48:6053–6062, 2019. 18

[41] E. R. Gertner G. M. Williams J. E. Clarke J. G. Pasko D. T. Cheung, A. M. Andrews and J. T. Longo. Backside-illuminated InAs1xSbx-InAs narrow-band photodetectors. *Applied Physics Letters*, 30:587–589, 1977. 18

[42] E. R. Gertner D. T. Cheung, A. M. Andrews and L. O. Bubulac. Backside-illuminated InAsSb/GaSb broadband detectors. *Applied Physics Letters*, 36:734–736, 1980. 18

[43] S.Adachi. *Springer Handbook of Electronic and Photonic Materials. III-V Ternary and Quaternary Compounds.* Springer International Publishing, 2017. 19, 20

[44] T.-Y. Tsai C. H. Wu Y. R. Wu P. Martyniuk, K. Michalczewski. Theoretical simulation of the barrier t2sls InAs/InAsSb/b-AlSb longwave detector operating under thermoelectrical cooling. *2019 International Conference on Numerical Simulation of Optoelectronic Devices (NUSOD)*, 2019. 19

[45] H. Wieder and A. Clawson. Photo-electronic properties of InAs0.07Sb0.93 films. *Thin Solid Films*, 15:217–221, 1973. 19, 39

[46] I. Vurgaftman, J. R. Meyer, and L. R. Ram-Mohan. Band parameters for iii–v compound semiconductors and their alloys. *Journal of Applied Physics*, 89:5815–5875, 2001. 19, 20

[47] Min Ren, Scott J. Maddox, Madison E. Woodson, Yaojia Chen, Seth R. Bank, and Joe C. Campbell. 20

[48] A. D'Souza J. Schuster and E. Bellotti. Analysis of InAsSb nbn spectrally filtering photon-trapping structures. *Opt. Express*, 22(16):18987–19004, 2014. 20, 24

[49] A. Rogalski and K. Jóźwikowski. Intrinsic carrier concentration and effective masses in InAs1xSbx. *Infrared Physics*, 29(1):35–42, 1989. 21, 39

[50] A. D'Souza, E. Robinson, A. Ionescu, D. Okerlund, T. Lyon, H. Sharifi, M. Roebuck, D. Yap, R. Rajavel, N. Dhar, P. Wijewarnasuriya, and C. Grein. Electrooptical characterization of mwir InAsSb detectors. *Journal of Electronic Materials*, 41:2671–2678, 2012. 21, 23

[51] P. Klipstein, O. Klin, S. Grossman, N. Snapi, Barak Yaakobovitz, M. Brumer, I. Lukomsky, D. Aronov, M. Yassen, Boris Yofis, A. Glozman, T. Fishman, E. Berkowicz, O. Magen, I. Shtrichman, and E. Weiss. Xbn barrier detectors for high operating temperatures. 2010. 22, 26

[52] S. J. Maddox, M. Ren, M. E. Woodson, S. R. Bank, J. C. Campbell, and Y. Chen. Low-noise AlInAsSb avalanche photodiode. *Applied Physics Letters*, 108(8), 2016. 22

[53] Yuexi Lyu, Xi Han, Yaoyao Sun, Zhi Jiang, Chunyan Guo, Wei Xiang, Yinan Dong, Jie Cui, Yuan Yao, Dongwei Jiang, Guowei Wang, Yingqiang Xu, and Zhichuan Niu. Digitally grown AlInAsSb for high gain separate absorption, grading, charge, and multiplication avalanche photodiodes. *Journal of Crystal Growth*, 482:70–74, 2018. 22

[54] Y. Aytac, B. V. Olson, J. K. Kim, E. A. Shaner, S. D. Hawkins, J. F. Klem, M. E. Flatte, and T. F. Boggess. Effects of layer thickness and alloy composition on carrier lifetimes in mid-wave infrared InAs/InAsSb superlattices. *Applied Physics Letters*, 105(2), 2014. 23

[55] H. J. Haugan, F. Szmulowicz, K. Mahalingam, G. J. Brown, S. L. Bowers, and J. A. Peoples. Compositional control of the mixed anion alloys in gallium-free InAs/InAsSb superlattice materials for infrared sensing. *Infrared Sensors, Devices, and Applications*, 9609, 2015. 23

[56] P. Klipstein. "xbn" barrier photodetectors for high sensitivity and high operating temperature infrared sensors. 2008. 23, 26, 36

[57] David Z. Ting, Cory J. Hill, Alexander Soibel, Jean Nguyen, Sam A. Keo, Michael C. Lee, Jason M. Mumolo, John K. Liu, and Sarath D. Gunapala. Antimonide-based barrier infrared detectors. 7660:76601R, 2010. 23, 25

[58] M. E. Flatte and C. H. Grein. Theory and modeling of type-ii strained-layer superlattice detectors. *Quantum Sensing and Nanophotonic Devices V*, 7222:72220Q, 2009. 23

[59] A. Rogalski and Z. Orman. Band-to-band recombination in InAs1xSbx. *Infrared Physics*, 25:551–560, 1985. 24

[60] L. K. Casias, C. P. Morath, E. H. Steenbergen, P. T. Webster, J. K. Kim, V. M. Cowan, G. Balakrishnan, and S. Krishna. Carrier concentration and transport in Be-doped InAsSb for infrared sensing applications. *Infrared Physics and Technology*, 96:184–191, 2019. 24, 25

[61] S. P. Svensson, F. J. Crowne, H. S. Hier, W. L. Sarney, W. A. Beck, Y. Lin, D. Donetsky, S. Suchalkin, and G. Belenky. Background and interface electron populations in InAs0.58Sb0.42. *Semiconductor Science and Technology*, 30(3):035018, 2015. 24

[62] D. Z. Ting, A. Soibel, A. Khoshakhlagh, Sir B. Rafol, S. A. Keo, L. Höglund, A. M. Fisher, E. M. Luong, and S. D. Gunapala. Mid-wavelength high operating temperature barrier infrared detector and focal plane array. *Applied Physics Letters*, 28:17611–17619, 2018. 24

[63] G.R. Savich D.E. Sidor and G.W Wicks. Surface leakage mechanisms in iii–v infrared barrier detectors. *Journal of Elec Materi*, 45:4663–4667, 2016. 25

[64] D. Sidor, G. Savich, and G. Wicks. Surface conduction in InAs and GaSb. 2015. 25

[65] E. Bellotti and D. D'Orsogna. Numerical analysis of HgCdTe simultaneous two-color photovoltaic infrared detectors. *IEEE Journal of Quantum Electronics*, 42(4):418–426, 2006. 25

[66] E. Gomółka, M. Kopytko, K. Michalczewski, Ł. Kubiszyn, and et al. A. Kebłowski. Electrical and optical performance of mid-wavelength infrared InAsSb heterostructure detectors. *Electro-Optical and Infrared Systems: Technology and Applications*, 57:027107, 2017. 25

[67] R. Singh and V. Mittal. Mercury cadmium telluride photoconductive long wave infrared linear array detectors. *Defence Science Journal*, 53:281–324, 2003. 26

[68] V. Pusino, C. Xie, A. Khalid, M. J. Steer, M. Sorel, I. G. Thayne, and D. R. S. Cumming. InSb photodiodes for monolithic active focal plane arrays on GaAs substrates. *IEEE Transactions on Electron Devices*, 63(8):3135–3142, 2016. 26

[69] Isaac Newton. De analysi per aequationes numero terminorum infinitas. 1669. 27

[70] Joseph Raphson. Analysis aequationum universalis. 1690. 27

[71] M. Hamad R. A. Jabr and Y. M. Mohanna. Newton-raphson solution of poisson's equation in a pn diode. *International Journal of Electrical Engineering Education*, 44:23–33, 2007. 27

[72] S. W. Corzine L. A. Coldren and M. L. Masanovic. *APPENDIX TWO, Relationships between Fermi Energy and Carrier Density and Leakage.Diode Lasers and Photonic Integrated Circuits*. John Wiley Sons, Inc, 2012. 32

[73] J. Klem, J. Kim, M. Cich, S. Hawkins, T. Fortune, and J. Rienstra. Comparison of nbn and nbp mid-wave barrier infrared photodetectors. *Quantum Sensing and Nanophotonic Devices VII*, 2010. 49, 56

Appendix A

6.1 Poisson-Continuity Solver

In the following pages there is a copy of the Poisson-Continuity solver written for this work. It contains the 3 building blocks explained in Chapter 3 and it has been run for a simulation at T = 300 K, V_{app} = -0.3 V. At the end, one can find a schematic of the band structure and the value of the dark current density.

Contents


```
%This program calculates the potential energy profile of an heterostructure
%barrier for InAsSb/AlInAsSb nBn photodetector

clear all

%************************************************************************
```

Constants and Material parameters

```
%Constants
kb= 1.38E-23;%J/K
T= 300 %K
q = 1.6E-19;%C
kbTeV= kb*T/q;%eV
h= 6.61E-34;%Js
h_eV = h/q; %eVs
hbar= h/(2*pi);%Js
m0= 9.11E-31;%kg
eps0= 8.85E-14;%F/cm
hbar_eV = hbar/q;%eVs
delta = 1E-7;%cm
t = hbar/delta;%eVs/cm
c = 3E8; %m/s

%Device characteristics
CL = 300; %Contact layer width in nm
BL = 280; %Barrier layer width in nm
AL = 3000; %Absorber layer width in nm
Npoints = CL + BL + AL;
Vapp = -0.3 %V

%Illumination conditions
flux_opt = 0; % 1.22E-5; %photons/cm2
lambda = 4.0; %um
freq = (c * 1E6 / lambda); %s-1
Energy_opt = h_eV * freq ; %eV
pulse_length_opt = 3.5E-3; %s
Intensity_opt_Cm2 = flux_opt * Energy_opt/pulse_length_opt; %W/cm2

%Parameters
%InAsSb (IAS)
x = 0.09;
NdCL = 5E15;%cm-3
NdAL = 8E15;%cm-3
meIAS = (0.023 -0.039*x + 0.03*x*x)*m0;%kg
mhhIAS = (0.41 + 0.02*x)*m0;%kg
```

```
mlhIAS = (0.026 - 0.011*x)*m0;%kg
mhIAS = ((mlhIAS)^1.5 + (mhhIAS)^1.5)^(2/3);%kg
red_mass = meIAS/mhIAS;
EgIAS = 0.411 - (3.4E-4*T*T/(210+T)) -0.876*x + 0.70*x*x +3.4E-4 * (T*x*(1-x));%eV
NvIAS = 2E-6*((2*pi*kbTeV*mhIAS*q)/(h*h))^(3/2);%cm-3
NcIAS = 2E-6*((2*pi*kbTeV*meIAS*q)/(h*h))^(3/2);%cm-3
epsIAS = (15.15 +1.65*x)*eps0;%F/cm
epsIAS_inf = (12.3 + 3.4*x)*eps0;%F/cm
niIAS = (1.35 +8.5*x + 4.22E-3*T -1.53E-3*x*T -6.73*x*x)*10^14 * T^1.5 *EgIAS^0.75* exp (-
 EgIAS / (2*kbTeV));%cm-3
nIAS_CL = NdCL/2 + sqrt ((NdCL/2)^2 + niIAS^2);%cm-3
nIAS_AL = NdAL/2 + sqrt ((NdAL/2)^2 + niIAS^2);%cm-3
pIAS_CL = niIAS^2/NdCL;%cm-3
pIAS_AL = niIAS^2/NdAL;%cm-3

mobility_e_InAs_300 = 3E4;
mobility_e_InSb_300 = 8E4;
mobility_e_InAs_T = mobility_e_InAs_300 * (T/300)^(-0.7212);
mobility_e_InSb_T = mobility_e_InSb_300 * (T/300)^(-1.8572);
mobility_e_IAS = mobility_e_InAs_T * (1-x) + mobility_e_InSb_T * x; %cm2/Vs
diff_coef_e_IAS = mobility_e_IAS * kbTeV; %cm2/s

mobility_h_InAs_300 = 500;
mobility_h_InSb_300 = 800;
mobility_h_InAs_T = mobility_h_InAs_300 * (T/300)^(-0.5019);
mobility_h_InSb_T = mobility_h_InSb_300 * (T/300)^(-1.8572);
mobility_h_IAS = mobility_h_InAs_T * (1-x) + mobility_h_InSb_T * x; %cm2/Vs
diff_coef_h_IAS = mobility_h_IAS * kbTeV; %cm2/s

k_illumination = 1E4 + 2E4 * EgIAS;
c_illumination = EgIAS/2 + 0.1;

if (Energy_opt > EgIAS);
    alpha_AL = abs (k_illumination * (Energy_opt - EgIAS - c_illumination) * sqrt ((Energy
_opt - EgIAS - c_illumination)^2 - c_illumination^2)/Energy_opt + 800);%cm-1
else
    alpha_AL = 948.23 * exp (170 * (Energy_opt - (EgIAS + 0.001))); %cm-1
end

Rrad = 5.8E-13 * (epsIAS_inf/eps0)^0.5 * (m0/ (meIAS + mhIAS))^1.5 * (1 + (m0/meIAS) + (m0
/mhIAS)) * (300/T)^1.5 * (EgIAS*EgIAS + 3*kbTeV*EgIAS + 3.75*kbTeV*kbTeV);%cm3/s
Raug1_n = (0.2*0.2*(meIAS/m0)*(EgIAS/kbTeV)^(-1.5) * exp (- ((1 + 2*meIAS/mhIAS)/(1 + meIA
S/mhIAS))*(EgIAS/kbTeV)))/(2*(epsIAS_inf*niIAS/eps0)^2*(1+red_mass)^0.5 * (1+2*red_mass)*3
.8E-18);%cm6/s
Raug1_p = Raug1_n * ((1 - 3*EgIAS/kbTeV)/(6*(1 - (5*EgIAS)/(4*kbTeV))));%cm6/s

lfi_a1_h_IAS = 3.8E-18 * ((epsIAS/eps0)^2 * sqrt (1+red_mass)*(1+2*red_mass) * exp ((EgIAS
/kbTeV)*((1+2*red_mass)/(1+red_mass))))/((meIAS/m0)*0.2*0.2*(kbTeV/EgIAS)^(1.5)); %s
lf_a1_h_IAS = 2 * lfi_a1_h_IAS /(1 + (nIAS_AL/niIAS)^2); %s
diff_length_h_IAS = sqrt (diff_coef_h_IAS * lf_a1_h_IAS); %cm

Gopt = alpha_AL * Intensity_opt_Cm2/(Energy_opt*q); %cm-3s-1
p_opt = lf_a1_h_IAS * Gopt; %cm-3
n_opt = p_opt;

%AlInAsSb (AIAS)
NDBL =1E16;%cm-3
meAIAS = 0.071*m0;%kg
mhAIAS = 0.35*m0;%kg
EgAIAS = 1.16;%eV
NvAIAS = 2E-6*((2*pi*kbTeV*mhAIAS*q)/(h*h))^(3/2);%cm-3
```

```
NcAIAS = 2E-6*((2*pi*kbTeV*meAIAS*q)/(h*h))^(3/2);%cm-3
epsAIAS = 15.5*eps0;%F/m
niAIAS = sqrt (NcAIAS * NvAIAS) * exp (-EgAIAS/(2*kbTeV));%cm-3
nAIAS_BL = NDBL;%cm-3
pAIAS_BL = niAIAS^2/NDBL;%cm-3
mobility_h_AIAS = 3000; %cm2/Vs
diff_coef_h_AIAS = mobility_h_AIAS * kbTeV;%cm2/s

deltaEv300= 0.02586;%eV
deltaEv = deltaEv300 - (EgIAS - (0.411 - (3.4E-4*300*300/(510)) -0.876*x + 0.70*x*x +3.4E-
4 * (300*x*(1-x))));%eV
deltaEg = EgAIAS - EgIAS;%eV
deltaEc = deltaEg - deltaEv;%eV

%Built-in characteristics
Vbi1 = deltaEc - kbTeV*log((nIAS_CL*NcAIAS)/(NDBL*NcIAS)); %Built-in voltage between CL an
d BL
Vbi2 = - deltaEc - kbTeV*log((NDBL*NcIAS)/(nIAS_AL*NcAIAS)); %Built-in voltage between BL
and AL

Ec_init_IAS_CL =  kbTeV*log (NcIAS/nIAS_CL -1);
Ec_init_AIAS_BL = Vbi1 - kbTeV*log (nAIAS_BL/NcAIAS);
Ec_init_IAS_AL = kbTeV*log (NcIAS/nIAS_AL -1);

if Intensity_opt_Cm2 == 0;
Ef_h_AL_opt = 0;
else
Ef_h_AL_opt = (Ec_init_IAS_AL - EgIAS) + kbTeV * log ((NvIAS/(pIAS_CL+p_opt))-1);
end

slope = (Ec_init_AIAS_BL - (Ec_init_IAS_AL + deltaEc))/BL;
slope_V = (Vbi1+Vbi2)/BL;
slope_Vapp = (Vapp)/BL;

%%%%%%%%%%%%%%%%%%%%%%%%%%%%%%%%%%%%%%%%%%%%%%%%%%%%%%%%%%%%%%%%%%%%%%%%%%%%%%%%%%%%%%%
```

```
T =

   300


Vapp =

   -0.3000
```

Built-in Parameters

```
%Parameters' change across the device. Total points for the device's
%simulation are set to be Npoints+2 to account for boundary conditions,
%both on the contact layer and abserober layer ends. The different
%parameters described in the for loop are the bulk characteristics for the
%materials involved in the heterostructure.

for i = 1:Npoints +2
    if (i <= CL + 1);
        meff_e (i,:) = meIAS;
        eps (i,:) = epsIAS;
```

```
        Ndop (i,:) = NdCL;
        Nc_bulk (i,:) = NcIAS;
        Nv_bulk (i,:) = NvIAS;
        ni_bulk (i,:) = niIAS;
        n_bulk (i,:) = nIAS_CL;
        p_bulk (i,:) = pIAS_CL;
        Vbulk_init (i,:) = Ec_init_IAS_CL;
        Ev_init (i,:) = Vbulk_init (i,:) - EgIAS;
        Ei_init (i,:) = Vbulk_init (i,:) - EgIAS/2;
        V_init_CL (i,:) = 0;
        V_init (i,:) = V_init_CL (i,:);
        mobility_h (i,:) = mobility_h_IAS;
        mobility_e (i,:) = mobility_e_IAS;
        diff_coef_h (i,:) = diff_coef_h_IAS;
        diff_coef_e (i,:) = diff_coef_e_IAS;


   elseif (i > CL +1) && (i <= CL+BL+1);
            meff_e (i,:) = meAIAS;
            eps (i,:) = epsAIAS;
            Ndop (i,:) = NDBL;
            Nc_bulk (i,:) = NcAIAS;
            Nv_bulk (i,:) = NvAIAS;
            ni_bulk (i,:) = niAIAS;
            n_bulk (i,:) = nAIAS_BL;
            p_bulk (i,:) = pAIAS_BL;
            Vbulk_init (i,:) = Ec_init_AIAS_BL - slope *(i-(CL+2));
            Ev_init (i,:) = Vbulk_init (i,:) - EgAIAS;
            Ei_init (i,:) = Vbulk_init (i,:) - EgAIAS/2;
            V_init_BL (i,:) = Vbi1 - slope_V * (i-(CL+2));
            V_init (i,:) = V_init_BL (i,:);
            mobility_h (i,:) = mobility_h_AIAS;
            mobility_e (i,:) = mobility_e_IAS;
            diff_coef_h (i,:) = diff_coef_h_AIAS;
            diff_coef_e (i,:) = diff_coef_e_IAS;

        else
            meff_e (i,:) = meIAS;
            eps (i,:) = epsIAS;
            Ndop (i,:) = NdAL;
            Nc_bulk (i,:) = NcIAS;
            Nv_bulk (i,:) = NvIAS;
            ni_bulk (i,:) = niIAS;
            n_bulk (i,:) = nIAS_AL;
            p_bulk (i,:) = pIAS_AL;
            Vbulk_init (i,:) = Ec_init_IAS_AL;
            Ev_init (i,:) = Vbulk_init (i,:) - EgIAS;
            Ei_init (i,:) = Vbulk_init (i,:) - EgIAS/2;
            V_init_AL (i,:) = -Vapp;
            V_init (i,:) = V_init_AL (i,:);
            mobility_h (i,:) = mobility_h_IAS;
            mobility_e (i,:) = mobility_e_IAS;
            diff_coef_h (i,:) = diff_coef_h_IAS;
            diff_coef_e (i,:) = diff_coef_e_IAS;

    end
end
%%%%%%%%%%%%%%%%%%%%%%%%%%%%%%%%%%%%%%%%%%%%%%%%%%%%%%%%%%%%%%%%%%%%%%%%%%%
```

Initial Guess

```
%Newton-Raphson Method for calculating the band profile and the
%electrostatic potential of the heterojuction.
% First we set a matrix V with the potential drop in each region, V in CL
% and AL is 0, V in BL changes from Vbi1 to Vbi1 - (Vbi1+Vbi2) . From this
% starting potential, the potential profile is calculated iteratively with
% the Newton-Raphson method for the Poisson's equation. The "for-loop" is
% set to keep the parameters constant when running the Newton-Raphson part
% as the iterative nature of the procedure can lead to accumulate errors in
% the derivatives that will give an incorrect result. G-R effects are taken
% into account for CL & AL, while in BL it is considered to be negligible
% as the CB & VB lie several kbT far from the Fermi level.

err = 1;

V = V_init;

for i = 1:Npoints+2

        Ec_bulk (i,:) = Vbulk_init (i,:);
        Ev_bulk (i,:) = Ev_init (i, :);
        Ei_bulk (i,:) = Ei_init (i, :);

         if (i <= CL + 1);
             Ef_e (i,:) = 0;
             Ef_h (i,:) = 0;
             n (i, :) = Nc_bulk (i,:) *(1./(1 + exp ((Ec_bulk (i,:) - Ef_e (i,:))/kbTeV)))
;
             p (i, :) = Nv_bulk (i,:) *(1./ (1+ exp (-(Ev_bulk (i,:) - Ef_h (i,:))/kbTeV))
);

            GR (i,:) = Rrad *(n(i,:)*p(i,:) - ni_bulk (i,:)*ni_bulk (i,:)) + (Raug1_n * n(
i,:) + Raug1_p * p(i,:))*(n(i,:)*p(i,:) - ni_bulk (i,:)*ni_bulk (i,:));

         elseif (i > CL +1) && (i <= CL+BL+1);
             Ef_e (i,:) = Vapp;

             %The quasi Fermi level of holes is assumed to vary linearly in the BL region,
 where the voltage drop occurs.
             Ef_h (i,:) = slope_Vapp * (i - (CL+2));

             n (i, :) = Nc_bulk (i,:) * exp (- (Ec_bulk (i,:)- (Ef_e (i,:)))/kbTeV);
             p (i, :) = Nv_bulk (i,:) *(1./ (1+ exp (-(Ev_bulk (i,:) - Ef_h (i,:)-V_init_B
L (i,:))/kbTeV)));

             GR (i,:) =0;

         else
             Ef_e (i,:) = Vapp;

             %EHPs generation is only happening in the AL. The second term
             %accounts for the the modifications in the carrier density
             %induced by the absorption of incoming radiation.
             Ef_h (i,:) = Vapp + Ef_h_AL_opt;

             n (i, :) = Nc_bulk (i,:) *(1./(1 + exp ((Ec_bulk (i,:) - Ef_e(i,:) - V_init_A
L (i,:))/kbTeV))) + n_opt;
             p (i, :) = Nv_bulk (i,:) *(1./(1+ exp (-(Ev_bulk (i,:) - Ef_h (i,:)-V_init_AL
 (i,:))/kbTeV))) + p_opt;

             GR (i,:) = Rrad *(n(i,:)*p(i,:) - ni_bulk (i,:)*ni_bulk (i,:)) + (Raug1_n * n
```

```
(i,:) + Raug1_p * p(i,:))*(n(i,:)*p(i,:) - ni_bulk (i,:)*ni_bulk (i,:)) - Gopt;
         end

end
```

Solver

```
%The loop runs until some convergence criteria is met. The first block
%calculates the derivative of the potential and the dielectric constant in
%the Poisson equation. With the potential energy from V, the charge density
%is computed following Fermi-Dirac statistics for electrons both in the
%Absorber and Contact layers. Carriers are treated with Fermi-Dirac statistics.
%The information is stored in R and Mj. Mj is a
%tridiagonal matrix and using the backslash function in Matlab the linear
%system is solved where the solution DV gives the correction factor for V.
%Applying V(i+1) = V(i) + DV(i) the loop is run iteratively until
% convergence. After the potential is calculated, another for-loop is used
% to calculate the quasi-fermi level for the holes across the
% heterostructure with the Newton-Raphson method. Once the potential is
% converged, the new hole
% quasi-fermi level is calculated and updated to the initial guess.
% Electrons and holes distribution is calculated accordingly.

  while (err >= 2.2204E-13)

for i = 2: Npoints+1
        sn_eps (i-1,:)= (eps (i,:) + eps (i-1,:))/ (2*delta*delta);
        dn_eps (i-1,:) = (2*eps (i,:) + eps (i-1,:) + eps (i+1,:))/ (2*delta*delta);
        sn_plus_eps (i-1,:)= (eps (i,:) + eps (i+1,:))/ (2*delta*delta);

        diff2_V (i-1,:) = sn_eps (i-1,:) * V (i-1,:) - dn_eps (i-1,:)* V(i,:) + sn_plus_ep
s (i-1,:)* V(i+1,:);

        Ec_bulk (i,:) = Vbulk_init (i,:);
        Ev_bulk (i,:) = Ev_init (i, :);
        Ei_bulk (i,:) = Ei_init (i, :);

        E_field (i-1,:) = - (V(i,:) - V(i-1,:))/delta;

        if (i <= CL+1);
            n (i, 1) =  Nc_bulk (i,:) *(1./(1 + exp ((Ec_bulk (i,:) - Ef_e (i,:) - V (i,:)
)/kbTeV)));
            p (i, 1) = Nv_bulk (i,:)* (1./(1 + exp (-(Ev_bulk (i,:) - Ef_h (i,:) - V (i,:)
)/kbTeV)));
            rho (i-1,:) = q * (Ndop (i,:) + p (i,:) - n (i,:));

            %Derivative of rho with respect to V, taking into account the
            %three expressions above.
            dif_rho (i-1,:) = (q/kbTeV) * (-((p (i,:)* (exp (-(Ev_bulk (i,:) - Ef_h (i,:)
- V (i,:))/kbTeV))./(1 + exp (-(Ev_bulk (i,:) - Ef_h (i,:) - V (i,:))/kbTeV))) + (n (i,:)
* (exp ( (Ec_bulk (i,:) - Ef_e (i,:) -V(i,:))/kbTeV))./(1+exp ( (Ec_bulk (i,:) - Ef_e (i,
:) -V(i,:))/kbTeV)));

            grad_n (i-1,:) = (n(i,:) - n(i-1,:))/delta;
            grad_p (i-1,:) = (p(i,:) - p (i-1,:))/delta;

            GR (i,:) = Rrad *(n(i,:)*p(i,:) - ni_bulk (i,:)*ni_bulk (i,:)) + (Raug1_n * n(
i,:) + Raug1_p * p(i,:))*(n(i,:)*p(i,:) - ni_bulk (i,:)*ni_bulk (i,:));

        elseif (i > CL +1) && (i <= CL+BL +1)
```

```
            n (i, :) = Nc_bulk (i,:) * exp (- (Ec_bulk (i,:)- (Ef_e (i,:)- V (i,:)))/kbTe
V);
            p (i, 1) = Nv_bulk (i,:)* (1./(1 + exp (-(Ev_bulk (i,:) - Ef_h (i,:) - V (i,:
))/kbTeV)));
           rho (i-1,:) = q * (Ndop (i,:) + p (i,:) - n (i,:));
           dif_rho (i-1,:) = (q/kbTeV) * (-((p (i,:)* (exp (-(Ev_bulk (i,:) - Ef_h (i,:)
- V (i,:))/kbTeV))./(1 + exp (-(Ev_bulk (i,:) - Ef_h (i,:) - V (i,:))/kbTeV))) + (n (i,:)
));
           grad_n (i-1,:) = (n(i,:) - n(i-1,:))/delta;
           grad_p (i-1,:) = (p(i,:) - p (i-1,:))/delta;

            GR (i,:) = 0;

        else
            n (i, 1) = Nc_bulk (i,:) *(1./(1 + exp ((Ec_bulk (i,:) - Ef_e(i,:) -V(i,:))/kb
TeV))) + n_opt;
            p (i, 1) = Nv_bulk (i,:)* (1./(1 + exp (-(Ev_bulk (i,:) - Ef_h (i,:) - V (i,:)
)/kbTeV))) + p_opt;
            rho (i-1,:) = q * (Ndop (i,:) + p (i,:) - n (i,:));
            dif_rho (i-1,:) = (q/kbTeV) * (-(((Nv_bulk (i,:)* (1./(1 + exp (-(Ev_bulk (i,:
) - Ef_h (i,:) - V (i,:))/kbTeV))))* (exp (-(Ev_bulk (i,:) - Ef_h (i,:) - V (i,:))/kbTeV))
)./(1 + exp (-(Ev_bulk (i,:) - Ef_h (i,:) - V (i,:))/kbTeV))) + ((Nc_bulk (i,:) *(1./(1 +
exp ((Ec_bulk (i,:) - Ef_e(i,:) -V(i,:))/kbTeV))))* (exp ( (Ec_bulk (i,:) - Ef_e (i,:) -V(
i,:))/kbTeV))./(1+exp ( (Ec_bulk (i,:) - Ef_e (i,:) -V(i,:))/kbTeV)));
            grad_n (i-1,:) = (n(i,:) - n(i-1,:))/delta;
            grad_p (i-1,:) = (p(i,:) - p (i-1,:))/delta;

            GR (i,:) = Rrad *(n(i,:)*p(i,:) - ni_bulk (i,:)*ni_bulk (i,:)) + (Raug1_n * n(
i,:) + Raug1_p * p(i,:))*(n(i,:)*p(i,:) - ni_bulk (i,:)*ni_bulk (i,:)) -Gopt;

        end

        %Right-hand term in the matrix equation
        R (i-1,:) = diff2_V (i-1,:) + rho(i-1,:);

end

%diagonal term in Mj
diag = dn_eps + dif_rho;

%Mj is the tridiagonal matrix in the matrix system of equations that is
%going to be solved
Mj = sparse (1:Npoints, 1:Npoints, diag, Npoints, Npoints) + sparse (2: Npoints, 1: Npoint
s - 1, -sn_eps (2:Npoints,:), Npoints, Npoints) + sparse (1: Npoints-1, 2: Npoints, -sn_pl
us_eps (1:Npoints-1,:), Npoints, Npoints) ;

DV = Mj \ R;

V(2:Npoints+1, :) = V(2:Npoints+1, :) + DV;

for j = 2:Npoints+1

    %hole density at the VB edge with the new electrostatic potential
    %distribution.
    p (j, 1) = Nv_bulk (j,:)* (1./(1 + exp (-(Ev_bulk (j,:) - Ef_h (j,:) - V (j,:))/kbTeV)
));

    %Gradient of the hole quasi-Fermi level
    diff_Ef_h (j-1,:) = (Ef_h(j,:) - Ef_h(j-1,:))/delta;

    %Second derivative of the hole quasi-Fermi level with respect to x
```

```
    diff2_Ef_h (j-1,:) = (Ef_h (j+1,:) -2*Ef_h (j,:) + Ef_h (j-1,:))/(delta*delta);

    %Derivative of the hole concentration as a function of the hole
    %quasi-Fermi level
    diff_p (j-1,:) = (q/kbTeV) * (-((Nv_bulk (i,:)* (1./(1 + exp (-(Ev_bulk (i,:) - Ef_h (
i,:) - V (i,:))/kbTeV))))* (exp (-(Ev_bulk (j,:) - Ef_h (j,:) - V (j,:))/kbTeV))./(1 + ex
p (-(Ev_bulk (j,:) - Ef_h (j,:) - V (j,:))/kbTeV)));
    grad_p (j-1,:) = (p(j,:) - p (j-1,:))/delta;
    diff_mob (j-1,:) = (mobility_h (j,:) - mobility_h (j-1,:))/delta;

    %Right-hand term in the hole quasi-Fermi level matrix equation
    R_Ef_h (j-1,:) = diff_Ef_h (j-1,:)*(mobility_h (j,:)*grad_p(j-1,:) + diff_mob (j-1,:)*
p(j,:)) + mobility_h (j,:)*p(j,:)*diff2_Ef_h (j-1,:) + GR (j,:);

    %Diagonal and off diagonal terms in the tridiagonal matrix Mj_Ef_h
    diag_Ef_h (j-1,:) = 2*(mobility_h(j,:)*p(j,:))/(delta*delta) - (mobility_h (j,:)*grad_
p(j-1,:))/delta - (diff_mob (j-1,:)*p(j,:))/delta;
    off_diag_Ef_h (j-1,:) = -(mobility_h(j,:)*p(j,:))/(delta*delta) + (mobility_h (j,:)*gr
ad_p(j-1,:))/delta + (diff_mob (j-1,:)*p(j,:))/delta;
    off_diag_plus_Ef_h (j-1,:) = -mobility_h(j,:)*p(j,:)/(delta*delta);

    %Derivative of the GR term with respect to the hole quasi-Fermi level
    diff_GR_Ef_h (j-1,:) = Rrad*diff_p(j-1,:)*n(j,:) + Raug1_p*diff_p(j-1,:)*(n(j,:)*p(j,:
) - ni_bulk (j,:)*ni_bulk (j,:)) + (Raug1_n * n(j,:) + Raug1_p * p(j,:))*diff_p(j-1,:)*n(j
,:);
end

main_diag_Ef_h = diag_Ef_h + diff_GR_Ef_h;
Mj_Ef_h = sparse (1:Npoints, 1:Npoints, main_diag_Ef_h, Npoints, Npoints) + sparse (2: Npo
ints, 1: Npoints - 1, off_diag_Ef_h (2:Npoints,:), Npoints, Npoints) + sparse (1: Npoints-
1, 2: Npoints, off_diag_plus_Ef_h (1:Npoints-1,:), Npoints, Npoints);
DEf_h = Mj_Ef_h \ R_Ef_h;

for i = 2:Npoints+1
    deriv_Ef_h (i-1,:) = (Ef_h (i,:) - Ef_h (i-1,:))/delta;
    grad_p (i-1,:) = (p(i,:) - p (i-1,:))/delta;
end

err = norm (DV,2)*sqrt (Npoints);

  end

%Computation of new parameters once the iteration cycles have converged
Ef_h (2:Npoints+1,:) = Ef_h (2:Npoints+1,:) + DEf_h;

n =  Nc_bulk .*(1./(1 + exp ((Ec_bulk - Ef_e - V)/kbTeV)));
p =  Nv_bulk .*(1./(1 + exp (-(Ev_bulk -(Ef_h + V))/kbTeV)));

%%%%%%%%%%%%%%%%%%%%%%%%%%%%%%%%%%%%%%%%%%%%%%%%%%%%%%%%%%%%%%%%%%%%%%%%%%%%%%%%
```

Final parameters & Dark Current Density Calculation

```
%Key parameters fitted to the total width of the device
V = V(2:Npoints +1, :);
V_init = V_init (2:Npoints+1,:);
Ec_bulk = Vbulk_init (2:Npoints+1,:);
Ev_bulk = Ev_init (2:Npoints+1, :);
Ei_bulk = Ei_init (2:Npoints+1, :);
p = p (2:Npoints+1,:);
n = n (2:Npoints+1,:);
```

```
rho = q* (Ndop (2:Npoints+1) + p - n);
Ef_h = Ef_h (2:Npoints+1,:);
Ef_e = Ef_e (2:Npoints+1,:);
charge_density = rho/q;

%Calculation of the band structure
Ec = Ec_bulk - V;
Ev = Ev_bulk - V;
Ei = Ei_bulk - V;

%Calculation of the potential barrier and Vmax
barrier_RL = Ev(Npoints,:) - min (Ev);
Vmax = Ev (CL+BL,:) - min (Ev(CL:CL+BL,:));

if (barrier_RL >= 3*kbTeV)
barrier_effect = barrier_RL - 3*kbTeV;
else
barrier_effect = 0;
end
%Calculation of the dark current density
Jdark = q * pIAS_AL * (diff_length_h_IAS/lf_a1_h_IAS) * tanh (AL*delta/diff_length_h_IAS)
* exp (-(barrier_effect)/kbTeV); %A/cm2
```

Plot

```
plot (1:Npoints, Ec, 1:Npoints, Ev, 1:Npoints, Ef_h, 1:Npoints, Ef_e);
xlabel('Position (nm)')
ylabel('Potential energy (eV)')
legend({'Ec', 'Ev', 'Efh', 'Efe'}, 'Location', 'northeast')
```

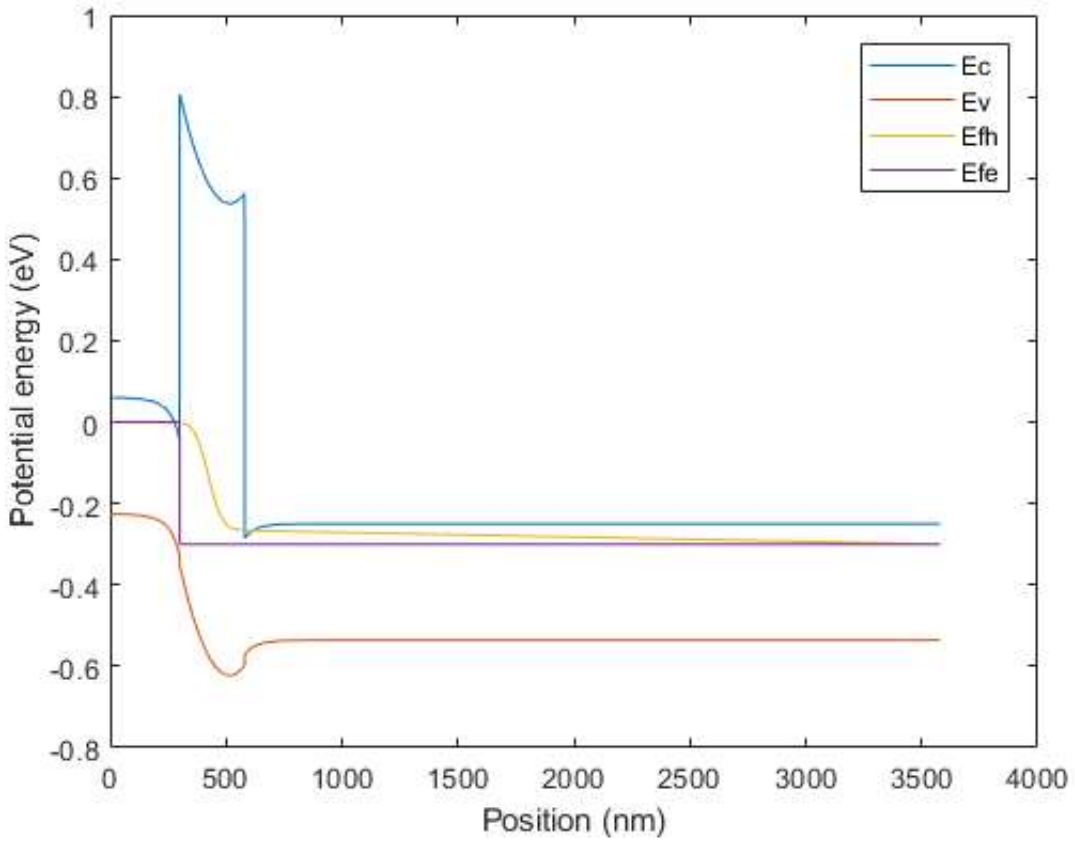

Published with MATLAB® R2017b